THE RESPONSE OF THE CARDIAC BIDOMAIN TO ELECTRICAL STIMULATION

By

Marcella C. Woods

Dissertation

Submitted to the Faculty of the

Graduate School of Vanderbilt University

in partial fulfillment of the requirements

for the degree of

DOCTOR OF PHILOSOPHY

in

Biomedical Engineering

December, 2005

Nashville, Tennessee

Approved:

Professor John P. Wikswo

Professor Robert L. Galloway

Professor Richard A. Gray

Professor Michael I. Miga

Professor Richard G. Shiavi

ACKNOWLEDGEMENTS

This dissertation would not have been possible without the help of numerous people. I would first like to thank my committee members for taking their time to support and help me in my graduate career. Special thanks go to my advisor, John Wikswo, for guiding me through this journey. At times the road was long and difficult, but this has been a rewarding experience and I have learned more than I ever anticipated. I am amazed at his wealth of knowledge, not only in cardiac electrophysiology, but of all matters in general.

I am especially grateful for the help I received from my fellow research lab members. The experimental expertise of Veniamin Sidorov has been invaluable. I have learned much from his calmness and patience in the lab. David Mashburn's work to rebuild and modify the "dog box" was critical to the completion of this dissertation. The improvements of the camera hardware and software by Mark Holcomb are wonderful, and make data collection and analysis much easier tasks.

A former lab member, Mark Bray, deserves special thanks. I have known Mark since our undergraduate days at Tulane University. His knowledge and friendship has meant a lot to me over the years. As he "abandoned" me to go to Harvard, I truly miss our frequent "sounding board" discussions of both the miseries and successes of our research. I dearly treasure the email messages and telephone calls we have had since he moved.

I would be remiss if I did not thank Brad Roth and Rick Gray. They are always so kind, supportive, and quick to respond to any questions asked of them. Their feedback

and help have been much appreciated. I also thank Jon Gilligan for his work and assistance in the cardiac lab while he was a member of our research group. Thomas Howe, the scientific glassblower in the Chemistry Department, fabricated numerous apparatuses for my experiments. I thank him for his work and skills.

The support from our staff members has made life much easier at times. I thank Don Berry, Cheryl Cosby, and, more recently, Allison Price for their patience and assistance during my graduate student career.

I must acknowledge the Whitaker Foundation, the Southeast Affiliate of the American Heart Association, the Academic Venture Capital Fund of Vanderbilt University, and the National Institutes of Health for generous financial support of my research endeavors.

I would also like to thank the numerous office mates I have had over the years. They have been good friends and great diversions when needed during the work day. I would particularly like to thank Shannon Faley. Her positive outlook and hard work ethics have inspired me over the past couple of years. I have enjoyed our conversations regarding parenthood, and I know that one day she will be laughing at me when I have children of my own. Megan Rothney, my fellow step aerobics addict, has been a good friend. Our regular Wednesday attendance of Mary Cady's class has been a bright point in the middle of the work week.

Of course, Patrick Norris deserves the most thanks of all. Without him, I do not think I would have reached this milestone. His support and love in both the good and bad times have been my driving force in my graduate career. I look forward to my future with him.

Lastly, I would like to thank my family members for supporting me along the way. My mother, brother, and nephew have not always understood my work and my choices, but they supported me regardless. My aunt, Judy, has always taken pride in my academic successes. I thank her for believing in me. My father, who passed away from heart disease when I was very young, was the inspiration for my interest in cardiac electrophysiology. I hope our research will one day lead to medical advancements to keep people like him with us longer. This dissertation is dedicated to his memory.

TABLE OF CONTENTS

LIST OF FIGURES

CHAPTER I

INTRODUCTION

In order to effectively treat and prevent cardiac rhythm disturbances, the response of the heart to electrical stimulation must be understood. For example, although cardiac defibrillation therapy is now a widely used and accepted medical procedure, the mechanisms by which a strong electrical shock halts potentially lethal fibrillation are still the subject of debate. While it is obvious that defibrillatory shocks activate and inactivate regions of the heart that are distant from the site of stimulation, standard cable models of cardiac tissue predict that such far-field stimulation would be ineffective more than a few millimeters from the stimulating electrode. Several alternative models have been proposed, including a "bidomain" model that includes the effects of tissue anisotropies and the separate intracellular and extracellular spaces.

The bidomain theory has been shown to characterize successfully many of the effects of electrical stimulation of the heart. Most notably, there is good agreement with experimental results of unipolar stimulation when an unequal anisotropy ratio is used in the bidomain model. Experiment and theory produce a “dog bone”-shaped region centered around the electrode with regions of the opposite sign in the convex portions of the “dog bone”. With reversal of the polarity, the spatial pattern of polarization reverses. These regions of positive and negative polarization, termed “virtual electrode polarization”, have proven responsible for four known modes of excitation in cardiac tissue.

According to the unequal-anisotropy ratio bidomain theory of cardiac tissue, any heterogeneity of the myocardium, such as fiber curvature or branching, should produce regions of hyperpolarization and depolarization in response to an externally applied electric field. This form of virtual electrode polarization provides a mechanism for the far-field stimulation that is observed experimentally. Adjacent areas of opposite polarization are potential sources of wave front generation, which would cause the transmembrane potential to be altered over a large region of the heart.

This research was directed at investigating the roles of virtual electrode polarization and other predictions of the unequal-anisotropy bidomain model in electrical stimulation of the heart.

1.1. Objectives

The objectives of this research were to examine experimentally the response of cardiac tissue under various conditions to electrical stimulation in the context of the bidomain model. Understanding the response of cardiac tissue to an electrical stimulus is crucial for the proper treatment and prevention of cardiac arrhythmias. To this end, we mapped optically the changes in transmembrane potential during and after electrical stimulation using voltage-sensitive fluorescent dyes. This technique allows non-invasive measurement of the transmembrane potential with high spatial and temporal resolution. We examined unipolar point stimulation of cardiac tissue under elevated extracellular potassium conditions, close to the refractory period, and through out the cardiac cycle. We also investigated field stimulation of the diastolic whole heart and the shock-induced changes in transmembrane potential around an artificial heterogeneity. A better

understanding of the cardiac response to electrical stimulation in these situations will facilitate improvement of anti-arrhythmic therapies.

1.2. Specific Aims

To complete the objectives of this research, the following specific aims were necessary:

Aim 1. Determine the effects of elevated extracellular potassium concentration on the response of diastolic cardiac tissue to unipolar stimulation. Cardiac disturbances, such as ischemia and hyperkalemia, are accompanied by elevation of the extracellular potassium concentration that, in turn, affects the resting transmembrane potential as well as tissue excitability. We examined the effects on the stimulation mechanism utilizing several visualization methods, including time-space plots.

Aim 2. Examine unipolar stimulation in the wake of a steadily propagating wave. The "pinwheel" stimulation protocol, in which a point stimulus is applied at the tail of steadily propagating conditioning wave, has been used in extensive theoretical studies of cardiac vulnerability to single premature stimuli, but only a few experimental mapping studies have examined this protocol. When we applied the unipolar test stimulus near the refractory period, interesting activation dynamics were observed that suggest substantial revision of the classical explanation of cardiac vulnerability is necessary.

Aim 3. Investigate the role of virtual electrode polarization from unipolar stimulation in excitability through the cardiac cycle. Although numerous researchers have examined excitability in different phases of the cardiac cycle, there has been no systematic experimental research to elucidate the correlation among the virtual

electrode polarization pattern, stimulation mechanism, and excitability under unipolar cathodal and anodal stimulation. In our experiments, we explained these relationships and constructed strength-interval curves that agree well with bidomain model simulations.

Aim 4. Examine and quantify the activation dynamics of the isolated rabbit heart in response to diastolic field stimulation. Although much research has been directed at studying the effects of field stimulation on systolic tissue, the effects of field stimulation on diastolic tissue are equally important. Our work is the first systematic experimental examination of the response of the isolated whole, intact heart to field shocks applied during diastole. Activation dynamics are measured as a function of shock strength, duration, and polarity.

Aim 5. Determine the role of heterogeneities in the response to field stimulation. Bidomain simulations of an insulated heterogeneity predict alternating regions of positive and negative polarization in response to field stimulation. We inserted a pulled glass micropipette through the myocardium and examined the shock-induced changes in transmembrane potential when the fiber direction was both parallel and perpendicular to the electric field. Shocks were applied to both systolic and diastolic tissue.

CHAPTER II

BACKGROUND AND SIGNIFICANCE

2.1. Introduction: Ventricular Fibrillation and Defibrillation

An estimated 300,000 to 400,000 fatalities each year in the United States are attributed to sudden cardiac death [1]. The most common cause of sudden cardiac death in the United States is ventricular fibrillation, a condition in which the electrical and mechanical activity of the ventricles becomes uncoordinated [2]. The ventricles exhibit chaotic, quivering behavior and cannot effectively pump blood though the cardiovascular system. Without intervention, death usually occurs within minutes. Cardiac defibrillation, a process that halts the arrhythmia, is most often accomplished by subjecting the heart to a strong electrical shock. Although defibrillation therapy has become a well-established practice, the mechanisms by which the electric field alters the myocardial transmembrane potential remain unclear. The future design of safer and more efficient defibrillators, pacemakers, and other anti-arrhythmic devices, as well as improvements in pharmacological treatments, depend upon the understanding of how the heart responds to electrical stimulation.

2.2. Function of the Heart

The heart is a muscular pump whose purpose is to circulate continuously blood throughout the body, delivering nutrients and removing wastes in the process. Most cells of the heart allow conduction of electrical impulses, but there is a specialized conduction system with autorhythmic properties that is essential to proper heart function. Initiation of

the cardiac cycle occurs from an electrical signal (action potential) generated by a specific region of these specialized conduction cells. The action potential then spreads throughout the heart in a coordinated fashion via the specialized conduction system to produce the contraction that pumps blood throughout the body. The heart consists of four chambers: the right atrium (RA), left atrium (LA), right ventricle (RV), and left ventricle (LV). The electromechanical activity of the cardiac cycle occurs in the following way.

The RA fills with deoxygenated blood from the body via the venae cavae while the LA fills with oxygenated blood from the lungs. The sinoatrial node, located in the RA, fires the wave of depolarization that spreads across the RA and LA, causing them to empty into the RV and LV, respectively. The atrioventricular (AV) node is the only electrical connection between the atria and ventricles. Once the electrical signal conducts through the AV node, the activation spreads down the septum between the two ventricles via the bundle of His. The right and left bundle branches depolarize the RV and LV, respectively. Purkinje fibers, cells that arise from the bundle branches, transmit the electrical signal to all parts of the ventricles, producing synchronized contraction of the ventricular muscle. RV contraction pushes the deoxygenated blood to the lungs via the pulmonary artery; LV contraction pumps oxygenated blood to the body through the aorta. When the chambers are filling, the heart is in diastole (rest). When the chambers are contracting and emptying, the heart is in systole. Without the orderly progression of electrical events, the heart is not able to pump blood effectively.

2.3. Structure of the Heart Walls

The heart walls are comprised of three layers: the epicardium, myocardium, and endocardium. The outer surface of the heart is called the epicardium. The epicardium is

usually very smooth and consists mostly of connective tissue, but also contains fat, blood vessels, and nerves. The myocardium lies between the epicardium and endocardium. In the ventricles the myocardium is the thickest layer. The ventricular myocardium consists of sheets of muscle fibers and is highly vascularized. The muscle fibers gradually rotate counterclockwise through the heart wall, with an approximate 120° total angle of rotation from the epicardium to the inner heart surface [3-5]. The rotation minimizes tension between the sheets and maximizes the contractile ability of the ventricles. The inner surfaces of the atria and ventricles are covered with mostly connective tissue, the endocardium. The endocardium also contains some nerves and the Purkinje conduction system, and is an irregular surface. The ridged myocardial surfaces covered by the endocardium are called trabeculae carnae.

2.4. The Cardiac Action Potential

The propagating action potential is mediated by ion channels in the cardiac cellular membrane. Cardiac membranes are excitable: stimulation above a threshold causes large changes in the voltage across the membrane (transmembrane potential, V_m). Connections between cells allow excitation to spread from cell-to-cell. Under normal conditions, the resting V_m is usually around -85 mV in a cardiac ventricular cell. When stimulation of suprathreshold amplitude occurs, an action potential is generated. The most important ion channels in cardiac tissue are those than conduct Na^+, K^+, and Ca^{2+}. These ions are most responsible for the five phases of the cardiac action potential, as shown in Figure 2.1. These ion channels are voltage-gated, meaning that they open and close depending upon V_m, with a time constant that reflects the speed of the opening and closing process.

The upstroke (phase 0) occurs when stimulation induces a change in V_m that opens fast voltage-gated Na^+ channels. Since extracellular [Na^+] is greater than intracellular [Na^+], Na^+ enters the cells and quickly depolarizes the membrane to approximately +25 mV. The Na^+ channels inactivate at the peak of the action potential. The brief rapid early repolarization after the peak (Phase 1) is caused by a transient outward K^+ current. The plateau (Phase 2) is a very distinct feature of cardiac action potentials and is responsible for their prolonged duration (200-300 ms). The plateau phase occurs from a balance of inward Ca^{2+} current and outward K^+ current. Contraction of the heart occurs during this phase due to the presence of intracellular Ca^{2+}. Repolarization (Phase 3) follows the plateau phase. Ca^{2+} channels close as slow K^+ channels open. The resulting K^+ efflux causes V_m to decrease. Finally, ion concentrations return to their resting levels via pumps and exchangers, and V_m returns to its resting value (Phase 4, diastole).

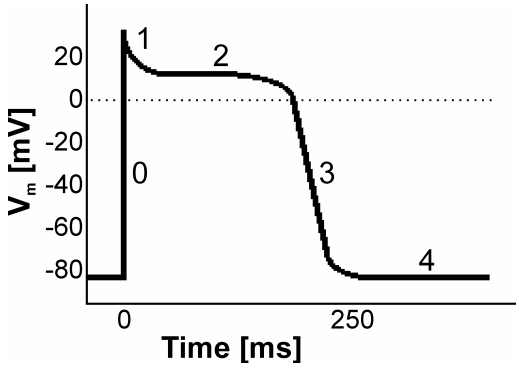

Figure 2.1. Typical ventricular action potential. Phases of the action potential are labeled. 0 – upstroke; 1 – early repolarization, 2 – plateau, 3 – repolarization, 4 – diastole.

2.5. The Bidomain Model

The bidomain model is a mathematical model that has been shown to successfully characterize many electrical properties of cardiac tissue and many of the effects of electrical stimulation of the heart [6]. The bidomain model is a multi-dimensional cable model [7] with distinct intracellular and extracellular spaces represented by networks of resistors. These two spaces are separated by a nonlinear cell membrane that is represented by parallel resistor and capacitor combinations. A schematic depicting the two-

dimensional bidomain model is shown in Figure 2.2 [8]. The electrical potentials of the intracellular and extracellular spaces are governed by the pair of coupled partial differential equations that comprise the bidomain model:

$$\nabla \cdot \tilde{\sigma}_i \nabla V_i = \beta(C_m \partial V_m / \partial t + J_{ion}) - I_i \qquad (1)$$

$$\nabla \cdot \tilde{\sigma}_e \nabla V_e = -\beta(C_m \partial V_m / \partial t + J_{ion}) - I_e, \qquad (2)$$

where $\tilde{\sigma}_i$ and $\tilde{\sigma}_e$ are the electrical conductivities of the two spaces (S/m), C_m is membrane capacitance per unit area (F/m^2), β is the ratio of cell membrane area to tissue volume (m^{-1}), J_{ion} is the membrane ionic current per unit area (A/m^2), and I_i and I_e are the intracellularly-applied and extracellularly-applied external current sources per unit volume (A/m^3). V_i, V_e, and V_m are the intracellular, extracellular, and transmembrane potentials, respectively.

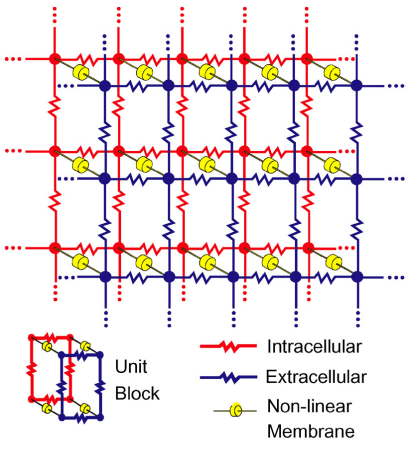

Figure 2.2. Schematic depicting the two-dimensional bidomain model (from [8]).

Use of the bidomain model has gained favor due to its representation of the cardiac microstructure as coupled, continuous domains rather than a single effective monodomain conductor or discrete structures. Thus, the anisotropic nature of cardiac tissue caused by the tissue architecture may be incorporated into the model. The electrical conductivities of the intracellular and extracellular spaces are directionally dependent, with differing anisotropies in the two spaces. This unequal anisotropy ratio leads to the well-known anisotropic conduction velocity, as well as a variety of surprising and interesting effects [9].

2.6. Unipolar Stimulation

Over the past fifteen years, John Wikswo's cardiac electrophysiology group at Vanderbilt University has been dedicated to conducting *in vitro* experiments to provide qualitative and quantitative tests of many of the predictions of the bidomain model. The ability to incorporate unequal anisotropy in the intracellular and extracellular domains in the bidomain model has led to good agreement between numerical simulations and experimental results of unipolar electrical stimulation [10]. The bidomain theory of cardiac tissue revealed that the unequal anisotropies of the intracellular and extracellular spaces play a key role in the virtual electrode appearance [11-14]. These numerical simulations predict that during anodal stimulation of the myocardium, a "dog bone"-shaped region of hyperpolarization arises centrally around the electrode, oriented transverse to the fiber direction. This "dog bone" is flanked by two regions of depolarization (virtual cathodes) lying in the convex portions of the "dog bone", oriented along the fiber direction. Conversely, during cathodal stimulation of the myocardium, a "dog bone" shaped region of depolarization arises centrally around the electrode and is flanked on each side by regions of hyperpolarization (virtual anodes). Wikswo *et al.* [15], Knisley [16], and Neunlist and Tung [17] confirmed these numerical predictions when they observed the virtual electrode effects experimentally using optical mapping. Figure 2.3 shows the marked discrepancy between cathodal point stimulation in the equal-anisotropy ratio bidomain model (A) and the experimental data (B), which are qualitatively consistent with results of the unequal-anisotropy ratio bidomain model (C).

Both numerical [14] and experimental [15] results reveal that virtual electrodes cause the four known mechanisms of excitation: cathode make, cathode break, anode

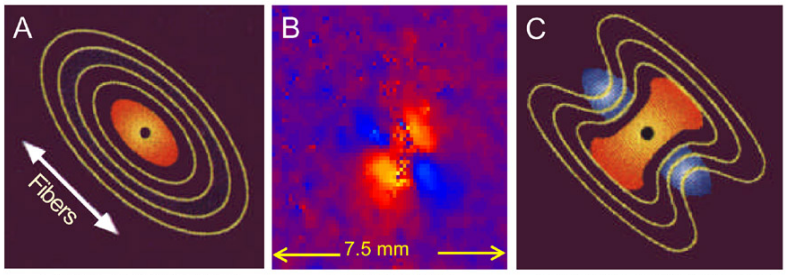

Figure 2.3. The response to unipolar cathodal stimulation. (A) Equal-anisotropy bidomain model. (B) Experimental data. (C) Unequal-anisotropy bidomain model. (From reference [15].)

make, and anode break. "Cathode" and "anode" simply refer to the polarity of the electrical stimulation. In make stimulation, the excitation originates in the depolarized regions at the onset of the stimulus. In break stimulation, however, the excitation originates in the hyperpolarized areas at the termination of the stimulus. Make excitation only occurs when resting tissue is stimulated. Break excitation can occur in both resting and refractory tissue by applying a long stimulus, or by applying a short stimulus during the repolarization stage of the action potential.

Although there has been great qualitative agreement between bidomain theory and experimental data for unipolar stimulation, there are some obvious quantitative discrepancies. One disagreement is in anodal and cathodal thresholds. Theory predicts thresholds that are smaller than those observed experimentally. Additionally, theory predicts anodal thresholds that are ten times greater than cathodal thresholds, while experimental data show a ratio more on the order of 4:1. One reason may be the very large transmembrane potentials predicted numerically near electrodes that are rarely observed experimentally [18].

The causes for the discrepancies between the numerical predictions and the experimental results may be due to experimental artifacts. Tests of voltage-sensitive dyes

commonly used to map transmembrane potential distribution show that they are linear for potentials between -100 mV and 100 mV [19,20], but may produce a constant response for potentials above 200 mV [20]. An additional experimental reason why large transmembrane potentials are not optically recorded is that optical mapping does not actually measure true surface polarization but, rather, a weighted average of transmembrane potential over a region of limited depth [21]. The depth of this region, however, is debated with predictions ranging from 300-500 μm [16,22] all the way up to 1-2 mm [23-25]. Additionally, the physical unipolar electrode prevents recording of the signal directly underneath it, where theory predicts the transmembrane potential will be largest [26]. However, recent experiments using a translucent electrode made from indium tin oxide removed this limitation [27]. Results under the electrode were in agreement with bidomain theory: changes in transmembrane potential were anisotropic, with larger values along the fiber axis. However, at the edge of the electrode, theory and experiment disagreed: bidomain simulations still predicted much larger transmembrane potentials than found experimentally.

Invalid modeling assumptions are also a likely cause of discrepancy between theory and experimental data. In numerical simulations, transmembrane potentials reach values (±400 mV) where electroporation should occur. However, many bidomain modeling studies have ignored electroporation. In studies where electroporation was incorporated into the model [28-32], quantitative differences were observed. One study [32] found that the inclusion of electroporation kept transmembrane potentials from becoming very large near an electrode. Another source of error in numerical studies is the membrane model. Membrane models, such as Beeler-Reuter [33] and Luo-Rudy [34,35],

are usually based on voltage clamp measurements in the range of normal action potentials. Therefore they do not accurately reflect changes occurring from strong shocks where transmembrane potential may be much larger. Use of membrane models in simulations involving strong shocks requires modification of the models which may or may not be valid because the nonlinear response of the cardiac cell membrane to large polarizations is not well known [36].

2.7. Field Stimulation

More recently, the focus of Wikswo's group has expanded to also encompass the unequal-anisotropy bidomain model predictions of field stimulation of the heart. The mechanisms by which defibrillation-strength electric shocks affect cardiac tissue have been the subject of extensive study in the cardiac biophysics community. Standard cable models predict changes in transmembrane potential that decrease exponentially with distance from the stimulating electrode and, hence, do not explain the large changes caused by external electric fields that have been observed distally from the electrode [37,38]. This phenomenon has been termed far-field stimulation, and many explanations have been hypothesized for its existence.

One hypothesis, the saw-tooth model, is an alternative to the bidomain model. In this model, Plonsey and Barr [39] suggest that the intercellular resistances at the gap junctions cause depolarization and hyperpolarization on opposite ends of each myocyte. Although the saw-tooth mechanism seems plausible and has been greatly studied, attempts to verify experimentally the saw-tooth effect thus far have failed [40,41]. A more recent study [42] suggests a new interpretation in which the saw-tooth effect may not necessarily appear as a polarity reversal across a gap junction. However, these results

are limited to a very simplistic two-cell model, and the saw-tooth effect still has not been observed in intact tissue.

A second hypothesis suggested by Trayanova, Roth, and Malden [43] proposes that fiber curvature and unequal anisotropy ratios cause depolarization and hyperpolarization throughout the heart. Their bidomain calculations also predict that the transmembrane potential at the epicardial surface may be vastly different than the transmembrane potential below the surface. Subsequent bidomain numerical simulations by Entcheva *et al.* [44] have supported the role of fiber curvature and fiber rotation in virtual electrode formation. Using an anatomically precise bidomain model of rabbit ventricles, Efimov *et al.* [45] predicted complex virtual electrode polarization patterns that would result in very different transmembrane potential distributions between the endocardium and epicardium, as shown in Figure 2.4.

Another hypothesis, proposed by Fishler [46], is that syncytial heterogeneities inherent throughout the bulk myocardium, such as cell-to-cell variations in myocyte shape and packing efficiency, play a role in the mechanism for far-field stimulation. Each of these syncytial heterogeneities produced a small "island" of depolarization and an adjacent "island" of hyperpolarization when an electric shock was applied. While this phenomenon has been observed on the level of single cells, experimental evidence at

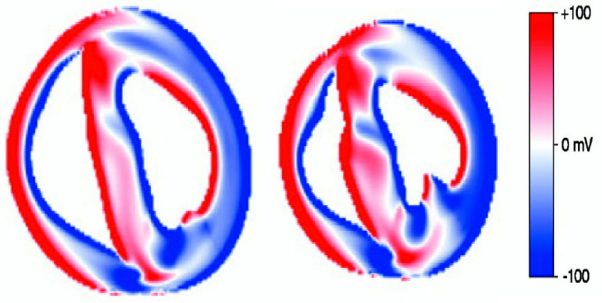

Figure 2.4. Predicted whole-heart response to field shock for two cross-sectional planes during a 5.8 V/cm electric field applied across the heart from right to left (virtual cathodes and virtual anodes are red and blue, respectively). Note the endocardial polarity is opposite to that on the epicardium (from [45]).

larger scales has proven inconclusive.

Macroscopic heterogeneities have also been suggested as a cause for the mechanisms of far-field stimulation. Using three computer models (a space-clamped membrane, a three-dimensional cylindrical cell, and a one-dimensional fiber), Krassowska and Kumar [47] suggest that the heart functions like a collection of short fibers that, in the presence of an electric field, should cause areas of hyperpolarization and depolarization to occur in a patchy fashion associated with each region. White *et al.* [48] found that myocardial discontinuities, caused by surgical incisions in the ventricular wall, can give rise to activation fronts following a stimulus, suggesting areas of polarization near the discontinuity.

More recent bidomain numerical simulations have hypothesized that electrodes often used to record the response of cardiac tissue to stimulation are potential causes of far-field stimulation or electrical artifacts in the recordings. Langrill Beaudoin and Roth [49,50] hypothesize that the insulated plunge electrodes used to record experimentally extracellular potentials [51] may affect the transmembrane potential when subjected to an electric field. Numerical simulations predict that the transmembrane potential induced around the electrode during a field shock exhibits alternating areas of depolarization and hyperpolarization. Patel and Roth [52] examined possible artifacts caused by another type of recording electrode. Epicardial surface electrodes are often used to record the electrical response of cardiac tissue during defibrillation experiments [51,53]. It has been assumed that these electrodes had no effect on the cardiac response. Numerical simulations by Patel and Roth, however, predict adjacent regions of depolarization and hyperpolarization

around the epicardial electrodes in an electric field because the epicardial electrodes have shorted out the extracellular space.

Each of the above hypotheses in some way incorporates bidomain myocardial heterogeneities as mechanisms for producing adjacent regions of hyperpolarization (virtual anodes) and depolarization (virtual cathodes) during an external electrical shock. The adjacent areas of opposite polarization are potential sources of wave front generation that could cause the far-field stimulation observed during electrical shocks. One goal of this research was to examine the roles of such inhomogeneities, emphasizing the macroscopic level, in the response of cardiac tissue to field shocks. Determining and understanding the mechanisms for far-field stimulation will enable the future design of safer and more efficient defibrillation devices.

2.8. Extracellular Potassium Concentration

An elevation in extracellular potassium concentration accompanies many cardiac abnormalities such as ischemia [54] and hyperkalemia [55]. This change in extracellular potassium concentration is known to increase the resting transmembrane potential and additionally affects the excitability of cardiac tissue. In humans normal $[K^+]_o$ is 5.4 mM, and the resting membrane potential is –84 mV. Increasing $[K^+]_o$ to 10 mM elevates the resting membrane potential to approximately –67 mV [55]. However, at transmembrane potentials above –70 mV the sodium inactivation gates are closed, rendering the tissue unexcitable [33]. Therefore the transmembrane potential distribution during electrical stimulation is dependent upon the extracellular potassium concentration. Although high extracellular potassium occurs clinically, there is relatively little work examining the effects of the extracellular potassium concentration on the cardiac shock response.

2.9. Electroporation

High-strength electrical shocks cause the formation of small pores in the lipid bilayer matrix, in a process termed "electroporation". The electropores, as these pores are commonly called, are hydrophilic and increase membrane conductance and permeability, facilitating intercellular molecular transport [56]. Experimental evidence indicates that electropores form when the transmembrane potential exceeds $\pm$400 mV [57]. For most electrical stimulation, electropores are not permanent and can reseal within seconds to minutes after the stimulation ceases [58]. For very strong stimulation, or stimulation of excessive duration, the electropores remain long after the termination of stimulation, leading to irreversible membrane damage and eventual cell death.

There have been numerous numerical studies examining the potential role of electroporation in defibrillation and arrhythmogenesis [28-30,59-63], and more limited experimental studies in cultured cells [20,57,64-66] and tissue [24,67-69]. Characteristics of electroporated regions have included transient elevation in resting transmembrane potential, reduction in action potential amplitude, and decreased rate of rise in action potential upstroke. Neunlist and Tung [70] found that magnitudes of these signatures of electroporation increased sigmoidally with increasing shock strength. Hence electroporation is more likely to occur in regions of maximal shock-induced transmembrane potential polarization.

However, the location and spatial extent of electroporation in intact cardiac tissue is largely unknown [24]. A prior study revealed that electroporation is an asymmetric event, with more electropores of smaller size on the membrane side facing the anode, and fewer electropores of larger size facing the cathode [71]. Direct evidence of

electroporation in cell culture studies [72,73] and intact tissue [74,75] comes from using fluorescent probes. However, the experiments using intact tissue examined electroporation only under a very large stimulating electrode[74], and in permanent tissue damage from repetitive unipolar stimulation [75]. The spatial extent of reversible electroporation during unipolar stimulation remains unknown. Because the transmembrane potential distribution of unipolar stimulation is well-defined, unipolar stimulation would be a good experimental protocol for examination of the spatial pattern of electroporation in intact cardiac tissue.

2.10. Cardiac Optical Mapping

Traditional measurements of cardiac electrical activity have been acquired via microelectrode techniques or via extracellular electrodes placed within the myocardium or on the epicardial, endocardial, or torso surfaces. However, optical fluorescence imaging has arisen as an alternative means to map optically the electrical activity of the heart. The first successful application of optical fluorescence imaging of the heart occurred in 1976 [76]; since that time, optical fluorescence imaging has gained favor as an excellent technique to measure the electrical activity of the heart with high spatial and temporal resolution.

Optical fluorescence imaging involves using a fluoroprobe that is very sensitive to small changes in membrane potential. When the dye molecules are introduced to the cardiac cells, they lodge in the cellular membranes. When the transmembrane potential of those cells changes, the dye molecules undergo changes in their electronic structure, and consequently changes in their fluorescence spectra. This shift in the fluorescence spectra results in a fluoresced signal whose intensity is proportional to the transmembrane

potential. The transmembrane potential is usually computed as $-\Delta F/F$, where F is the fluorescence intensity recorded from resting tissue and ΔF is the difference in fluorescence between F and when the tissue is excited. The minus sign is used to invert the signal such that optically recorded action potentials have the same orientation as those recorded electrically. Excitation of the dye molecules can be achieved over very small areas using a laser beam [77,78] or, more commonly, over much larger regions of the heart via optical fibers or diffusers [79,80].

Optical fluorescence imaging of the electrical activity of the heart has proven very important in experimentally verifying theoretical predictions of unipolar stimulation of the anisotropic bidomain model [15-17]. Cardiac optical imaging has also been utilized to study the spatiotemporal aspects of fibrillation [81] and the mechanisms by which defibrillation-strength shocks halt fibrillation [82]. Its utility in these types of studies lies in the fact that cardiac optical mapping has many advantages over the more traditional glass microelectrode and extracellular electrode measurements.

One advantage is that optical mapping is a non-invasive technique. Microelectrode techniques require the impalement of the cell membrane. This results in undesirable cell damage, and could prove difficult because of the small size of cardiac myocytes and the contractile motion of the cells. The use of a fluoroprobe that is incorporated into the cell membrane alleviates these problems.

An additional benefit of optical mapping is the high spatial resolution that can be achieved. Glass microelectrode techniques obviously are limited to the spatial resolution of one cell at a time. Extracellular electrodes can be used to record from multiple sites simultaneously; however, the spatial resolution of such methods is limited by the size and

density of the electrodes. As electrode arrays become larger, their size and the ability to make good contact with the heart surface can be limiting factors. Optical mapping provides a means of simultaneous recordings from a multitude of sites, with high spatial resolution that depends upon the method of acquisition (*i.e*. CCD camera or photodiode array).

A key advantage of optical fluorescence imaging is that it is not subject to stimulus artifacts during electrical pulses. Both microelectrode and extracellular recordings are complicated by the presence of stimulus artifacts produced by the extracellular electric field. These artifacts mask the tissue response during stimulation, a time which may be very important to understanding the response of cardiac tissue to electrical stimulation. Because transmembrane potential, and not extracellular field, is measured during optical fluorescence imaging, the signal artifact caused by the stimulus is very small [82,83].

There are also some complications in optical fluorescence imaging. As discussed earlier, optical imaging does not actually measure the true epicardial polarization, but a weighted average of transmembrane potential of a debated depth of tissue. Another problem is motion artifacts caused by the contraction of the beating heart. Therefore the motion of the heart must either be stopped via mechanical or chemical means. Mechanical cessation of motion involves pressing the region of the heart to be imaged against glass or some other transparent surface [22,84]. While mechanical cessation eliminates any chemical agent that may affect the electrophysiological properties of the heart, pressing the heart against a surface increases the risk of ischemia in that region and the interface between the heart and the glass may have an effect on virtual electrode

polarization [85]. Excitation-contraction decouplers are usually used to stop motion in cardiac optical mapping experiments. Two commonly used chemical agents are diacetyl monoxime (BDM, DAM, 2,3-butanedione monoxime) and methoxyverapamil (D600, gallopamil). BDM inhibits cross-bridge interactions by blocking ATP-sensitive potassium channels. D600 acts by blocking calcium flux through the slow (L-type) calcium channels. Both slightly alter action potential properties by altering some membrane conductances [86-88]; BDM may also cause edema [89].

2.11. Summary and Dissertation Outline

This chapter provided a background of cardiac dynamics and electrical stimulation of cardiac tissue. The first section introduced fibrillation and explained that the mechanisms of defibrillation are not yet understood. The cardiac cycle, heart structure, and the ionic components of the cardiac action potential were then described. The bidomain model of cardiac tissue was introduced, and was followed by the validation of bidomain theory using unipolar stimulation. Field stimulation of cardiac tissue then was described, and the proposed role that heterogeneities play in the tissue shock response was discussed. Virtual electrode polarization in response to electrical stimulation and its role in excitation also were presented. The relevance of extracellular potassium and electroporation were included. Lastly, the optical fluorescence mapping process, its benefits over more traditional measurement techniques, and its confounding factors were explained.

The purpose of this research is to examine the effects of electrical stimulation of cardiac tissue under different circumstances in the context of the bidomain model. The dissertation is organized in the following manner.

Chapter 3 details the results of diastolic unipolar anodal stimulation during elevated extracellular potassium conditions. Specifically, the spatiotemporal activation in elevated extracellular potassium is compared with normal conditions, and the mechanism of excitation is examined.

Chapter 4 examines unipolar stimulation in the wake of a steadily propagating wave. The timing of the unipolar stimulation has great implications on the resulting activation dynamics.

Chapter 5 presents a systematic examination of excitability through the cardiac cycle. We present experimental strength-interval curves that agree with numerical bidomain predictions. The role of virtual electrodes and stimulation mechanisms in excitability at different times through the cardiac cycle is described.

Chapter 6 presents the results of field stimulation of the diastolic rabbit heart. Both shock strength and shock duration are shown to affect the shock-induced changes in transmembrane potential and activation dynamics. Shock polarity also plays a major role.

Chapter 7 discusses the effects of an artificial heterogeneity during field stimulation of cardiac tissue. The shock-induced changes in transmembrane potential around the heterogeneity are presented. Experimental results are in good agreement with bidomain predictions.

Chapter 8 summarizes the results of Chapters 3 through 7 and the overall objectives of this dissertation. The research considerations and societal implications are also discussed.

2.12. References

[1] Zipes, D. P. and Wellner, M., "Sudden cardiac death." *Circulation*, vol. 98, no. 21, pp. 2334-2351, 1998.

[2] Myerburg, R. J., Kessler, K. M., and Castellanos, A., "Sudden cardiac death: structure, function and time-dependence of risk." *Circulation*, vol. 85, no. 1 Suppl, pp. I2-I10, 1992.

[3] Streeter, D. D., "Gross morphology and fiber geometry of the heart." in Berne, R. M., Sperelakis, N., and Geiger, S. R. (eds.) *Handbook of Physiology* Bethesda, MD: American Physiological Society, 1979, pp. 61-112.

[4] Torrent-Guasp, F., *The Cardiac Muscle* Madrid: Juan March Foundation, 1973, pp. 11-39.

[5] Streeter, D. D., Spotnitz, H. M., Patel, D. P., Ross, J., Jr., and Sonnenblick, E. H., "Fiber orientation in the canine left ventricle during diastole and systole." *Circ Res*, vol. 24, no. 3, pp. 339-347, 1969.

[6] Roth, B. J. and Wikswo, J. P., "The effect of externally applied electrical fields on myocardial tissue." *Proceedings of the IEEE*, vol. 84, no. 3, pp. 379-391, 1996.

[7] Roth, B. J., "How the anisotropy of intracellular and extracellular conductivities influences stimulation of cardiac muscle." *J Math Biol*, vol. 30, no. 6, pp. 633-646, 1992.

[8] Lin, S.-F. and Wikswo, J. P., Jr., "New perspectives in electrophysiology from the cardiac bidomain." in Rosenbaum, D. S. and Jalife, J. (eds.) *Optical Mapping of Cardiac Excitation and Arrhythmias.* Armonk, NY: Futura Publishing Company, Inc., 2001, pp. 335-359.

[9] Wikswo, J. P., "Tissue anisotropy, the cardiac bidomain, and the virtual cathode effect." in Zipes, D. P. and Jalife, J. (eds.) *Cardiac Electrophysiology, From Cell to Bedside* Second ed. Philadelphia: W.B. Saunders Co., 1996, pp. 348-361.

[10] Roth, B. J., Lin, S.-F., and Wikswo, J. P., Jr., "Unipolar stimulation of cardiac tissue." *J Electrocardiol*, vol. 31, no. 6, pp. 6-12, 1998.

[11] Sepulveda, N. G. and Wikswo, J. P., Jr., "Electric and magnetic fields from two-dimensional anisotropic bisyncytia." *Biophys J*, vol. 51, no. 4, pp. 557-568, 1987.

[12] Sepulveda, N. G., Roth, B. J., and Wikswo, J. P., Jr., "Current injection into a two-dimensional anisotropic bidomain." *Biophys J*, vol. 55 pp. 987-999, 1989.

[13] Wikswo, J. P., Jr., "The complexities of cardiac cables: virtual electrode effects." *Biophys J*, vol. 66, no. 3 Pt 1, pp. 551-553, 1994.

[14] Roth, B. J., "A mathematical model of make and break electrical stimulation of cardiac tissue by a unipolar anode or cathode." *IEEE Trans Biomed Eng*, vol. 42, no. 12, pp. 1174-1184, 1995.

[15] Wikswo, J. P., Jr., Lin, S.-F., and Abbas, R. A., "Virtual electrodes in cardiac tissue: A common mechanism for anodal and cathodal stimulation." *Biophys J*, vol. 69, no. 6, pp. 2195-2210, 1995.

[16] Knisley, S. B., "Transmembrane voltage changes during unipolar stimulation of rabbit ventricle." *Circ Res*, vol. 77, no. 6, pp. 1229-1239, 1995.

[17] Neunlist, M. and Tung, L., "Spatial distribution of cardiac transmembrane potentials around an extracellular electrode: dependence on fiber orientation." *Biophys J*, vol. 68, no. 6, pp. 2310-2322, 1995.

[18] Roth, B. J., "Artifacts, assumptions, and ambiguity: Pitfalls in comparing experimental results to numerical simulations when studying electrical stimulation of the heart." *Chaos*, vol. 12, no. 3, pp. 973-981, 2002.

[19] Windisch, H., Ahammer, H., Schaffer, P., Muller, W., and Platzer, D., "Optical multisite monitoring of cell excitation phenomena in isolated cardiomyocytes." *Pflugers Arch*, vol. 430, no. 4, pp. 508-518, 1995.

[20] Cheng, D. K., Tung, L., and Sobie, E. A., "Nonuniform responses of transmembrane potential during electric field stimulation of single cardiac cells." *Am J Physiol Heart Circ Physiol*, vol. 277, no. 1, pp. H351-H362, 1999.

[21] Gray, R. A., "What exactly are optically recorded "action potentials"?" *J Cardiovasc Electrophysiol*, vol. 10, no. 11, pp. 1463-1466, 1999.

[22] Girouard, S. D., Laurita, K. R., and Rosenbaum, D. S., "Unique properties of cardiac action potentials recorded with voltage-sensitive dyes." *J Cardiovasc Electrophysiol*, vol. 7, no. 11, pp. 1024-1038, 1996.

[23] Efimov, I. R., Sidorov, V., Cheng, Y., and Wollenzier, B., "Evidence of three-dimensional scroll waves with ribbon-shaped filament as a mechanism of ventricular tachycardia in the isolated rabbit heart." *J Cardiovasc Electrophysiol*, vol. 10, no. 11, pp. 1452-1462, 1999.

[24] Al-Khadra, A., Nikolski, V., and Efimov, I. R., "The role of electroporation in defibrillation." *Circ Res*, vol. 87, no. 9, pp. 797-804, 2000.

[25] Baxter, W. T., Mironov, S. F., Zaitsev, A. V., Jalife, J., and Pertsov, A. M., "Visualizing excitation waves inside cardiac muscle using transillumination." *Biophys J*, vol. 80, no. 1, pp. 516-530, 2001.

[26] Patel, S. G. and Roth, B. J., "How electrode size affects the electric potential distribution in cardiac tissue." *IEEE Trans Biomed Eng*, vol. 47, no. 9, pp. 1284-1287, 2000.

[27] Liau, J., Dumas, J., Janks, D., Roth, B. J., and Knisley, S. B., "Cardiac optical mapping under a translucent stimulation electrode." *Ann Biomed Eng*, vol. 32, no. 9, pp. 1202-1210, 2004.

[28] Aguel, F., DeBruin, K. A., Krassowska, W., and Trayanova, N. A., "Effects of electroporation on the transmembrane potential distribution in a two-dimensional bidomain model of cardiac tissue." *J Cardiovasc Electrophysiol*, vol. 10, no. 5, pp. 701-714, 1999.

[29] Ashihara, T., Yao, T., Namba, T., Ito, M., Ikeda, T., Kawase, A., Toda, S., Suzuki, T., Inagaki, M., Sugimachi, M., Kinoshita, M., and Nakazawa, K., "Electroporation in a model of cardiac defibrillation." *J Cardiovasc Electrophysiol*, vol. 12, no. 12, pp. 1393-1403, 2001.

[30] Skouibine, K. B., Trayanova, N. A., and Moore, P. K., "Anode/cathode make and break phenomena in a model of defibrillation." *IEEE Trans Biomed Eng*, vol. 46, no. 7, pp. 769-777, 1999.

[31] Ashihara, T. and Trayanova, N. A., "Asymmetry in membrane responses to electric shocks: Insights from bidomain simulations." *Biophys J*, vol. 87, no. 4, pp. 2271-2282, 2004.

[32] Bray, M.-A. and Roth, B. J., "The effect of electroporation on the strength-interval curve during unipolar stimulation of cardiac tissue." *Proceedings of the 19th Annual IEEE/EMBS Conference*, pp. 15-18, 1997.

[33] Beeler, G. W. and Reuter, H., "Reconstruction of the action potential of ventricular myocardial fibres." *J Physiol (Lond)*, vol. 268, no. 1, pp. 177-210, 1977.

[34] Luo, C. H. and Rudy, Y., "A model of the ventricular cardiac action potential. Depolarization, repolarization, and their interaction." *Circ Res*, vol. 68, no. 6, pp. 1501-1526, 1991.

[35] Luo, C. H. and Rudy, Y., "A dynamic model of the cardiac ventricular action potential. II. Afterdepolarizations, triggered activity, and potentiation." *Circ Res*, vol. 74, no. 6, pp. 1097-1113, 1994.

[36] O'Neill, R. J. and Tung, L., "Cell-attached patch clamp study of the electropermeabilization of amphibian cardiac cells." *Biophys J*, vol. 59, no. 5, pp. 1028-1039, 1991.

[37] Roth, B. J. and Krassowska, W., "The induction of reentry in cardiac tissue. The missing link: How electric fields alter transmembrane potential." *Chaos*, vol. 8, no. 1, pp. 204-220, 1998.

[38] Newton, J. C., Knisley, S. B., Zhou, X., Pollard, A. E., and Ideker, R. E., "Review of mechanisms by which electrical stimulation alters the

transmembrane potential." *J Cardiovasc Electrophysiol*, vol. 10, no. 2, pp. 234-243, 1999.

[39] Plonsey, R. and Barr, R. C., "Effect of microscopic and macroscopic discontinuities on the response of cardiac tissue to defibrillating (stimulating) currents." *Med Biol Eng Comput*, vol. 24, no. 2, pp. 130-136, 1986.

[40] Zhou, X., Smith, W. M., Rollins, D. L., and Ideker, R. E., "Spatial changes in transmembrane potential during a shock." *PACE*, vol. 18 pp. 935, 1995.

[41] Gillis, A. M., Fast, V. G., Rohr, S., and Kleber, A. G., "Spatial changes in transmembrane potential during extracellular electrical shocks in cultured monolayers of neonatal rat ventricular myocytes." *Circ Res*, vol. 79, no. 4, pp. 676-690, 1996.

[42] Sharma, V. and Tung, L., "Theoretical and experimental study of sawtooth effect in isolated cardiac cell-pairs." *J Cardiovasc Electrophysiol*, vol. 12, no. 10, pp. 1164-1173, 2001.

[43] Trayanova, N. A., Roth, B. J., and Malden, L. J., "The response of a spherical heart to a uniform electric field: a bidomain analysis of cardiac stimulation." *IEEE Trans Biomed Eng*, vol. 40, no. 9, pp. 899-908, 1993.

[44] Entcheva, E., Trayanova, N. A., and Claydon, F. J., "Patterns of and mechanisms for shock-induced polarization in the heart: A bidomain analysis." *IEEE Trans Biomed Eng*, vol. 46, no. 3, pp. 260-270, 1999.

[45] Efimov, I. R., Aguel, F., Cheng, Y., Wollenzier, B., and Trayanova, N., "Virtual electrode polarization in the far field: implications for external defibrillation." *Am J Physiol Heart Circ Physiol*, vol. 279, no. 3, pp. H1055-H1070, 2000.

[46] Fishler, M. G., "Syncytial heterogeneity as a mechanism underlying cardiac far-field stimulation during defibrillation-level shocks." *J Cardiovasc Electrophysiol*, vol. 9, no. 4, pp. 384-394, 1998.

[47] Krassowska, W. and Kumar, M. S., "The role of spatial interactions in creating the dispersion of transmembrane potential by premature electric shocks." *Ann Biomed Eng*, vol. 25, no. 6, pp. 949-963, 1997.

[48] White, J. B., Walcott, G. P., Pollard, A. E., and Ideker, R. E., "Myocardial discontinuities: a substrate for producing virtual electrodes that directly excite the myocardium by shocks." *Circulation*, vol. 97, no. 17, pp. 1738-1745, 1998.

[49] Langrill, D. M. and Roth, B. J., "The effect of plunge electrodes during electrical stimulation of cardiac tissue." *IEEE Trans Biomed Eng*, vol. 48, no. 10, pp. 1207-1211, 2001.

[50] Langrill Beaudoin, D. and Roth, B. J., "Effect of plunge electrodes in active cardiac tissue with curving fibers." *Heart Rhythm*, vol. 1, no. 4, pp. 476-481, 2004.

[51] Frazier, D. W., Wolf, P. D., Wharton, J. M., Tang, A. S., Smith, W. M., and Ideker, R. E., "Stimulus-induced critical point. Mechanism for electrical initiation of reentry in normal canine myocardium." *J Clin Invest*, vol. 83, no. 3, pp. 1039-1052, 1989.

[52] Patel, S. G. and Roth, B. J., "How epicardial electrodes influence the transmembrane potential during a strong shock." *Ann Biomed Eng*, vol. 29, no. 11, pp. 1028-1031, 2001.

[53] Chattipakorn, N., Kenknight, B. H., Rogers, J. M., Walker, R. G., Walcott, G. P., Rollins, D. L., Smith, W. M., and Ideker, R. E., "Locally propagated activation immediately after internal defibrillation." *Circulation*, vol. 97, no. 14, pp. 1401-1410, 1998.

[54] Gettes, L. S., "The electrophysiology of acute ischemia." in Fisch, C. and Surawicz, B. (eds.) *Cardiac electrophysiolgy and arrhythmias.* New York: Elsevier, 1991, pp. 13-24.

[55] Surawicz, B., "The interrelationship of electrolyte abnormalities and arrhythmias." in Mandel, W. J. (ed.) *Cardiac arrhythmias: Their mechanisms, diagnosis, and management.* Philadelphia: J.B. Lippincoff Company, 1995, pp. 89-109.

[56] Weaver, J. C., "Electroporation: a general phenomenon for manipulating cells and tissues." *J Cell Biochem*, vol. 51, no. 4, pp. 426-435, 1993.

[57] Tovar, O. and Tung, L., "Electroporation and recovery of cardiac cell membrane with rectangular voltage pulses." *Am J Physiol*, vol. 263, no. 4 Pt 2, pp. H1128-H1136, 1992.

[58] Tsong, T., "Electroporation of cell membranes." *Biophys J*, vol. 60, no. 2, pp. 297-306, 1991.

[59] Anderson, C., Trayanova, N., and Skouibine, K., "Termination of spiral waves with biphasic shocks: Role of virtual electrode polarization." *J Cardiovasc Electrophysiol*, vol. 11, no. 12, pp. 1386-1396, 2000.

[60] Krassowska, W., "Effects of electroporation on transmembrane potential induced by defibrillation shocks." *PACE*, vol. 18, no. 9, pp. 1644-1660, 1995.

[61] DeBruin, K. A. and Krassowska, W., "Electroporation and shock-induced transmembrane potential in a cardiac fiber during defibrillation strength shocks." *Ann Biomed Eng*, vol. 26, no. 4, pp. 584-596, 1998.

[62] Ashihara, T., Namba, T., Yao, T., Ozawa, T., Kawase, A., Ikeda, T., Nakazawa, K., and Ito, M., "Vortex cordis as a mechanism of postshock activation: Arrhythmia induction study using a bidomain model." *J Cardiovasc Electrophysiol*, vol. 14, no. 3, pp. 295-302, 2003.

[63] Ohuchi, K., Fukui, Y., Sakuma, I., Shibata, N., Honjo, H., and Kodama, I., "A dynamic action potential model analysis of shock-induced aftereffects in ventricular muscle by reversible breakdown of cell membrane." *IEEE Trans Biomed Eng*, vol. 49, no. 1, pp. 18-30, 2002.

[64] Fast, V. G., Rohr, S., and Ideker, R. E., "Nonlinear changes of transmembrane potential caused by defibrillation shocks in strands of cultured myocytes." *Am J Physiol Heart Circ Physiol*, vol. 278, no. 3, pp. H688-H697, 2000.

[65] Tovar, O. and Tung, L., "Electroporation of cardiac cell membranes with monophasic or biphasic rectangular pulses." *PACE*, vol. 14, no. 11 Pt 2, pp. 1887-1992, 1991.

[66] Tung, L., Tovar, O., Neunlist, M., Jain, S. K., and O'Neill, R. J., "Effects of strong electrical shock on cardiac muscle tissue." *Ann NY Acad Sci*, vol. 720 pp. 160-175, 1994.

[67] Knisley, S. B. and Grant, A. O., "Asymmetrical electrically induced injury of rabbit ventricular myocytes." *J Mol Cell Cardiol*, vol. 27, no. 5, pp. 1111-1122, 1995.

[68] Kodama, I., Shibata, N., Sakuma, I., Mitsui, K., Iida, M., Suzuki, R., Fukui, Y., Hosoda, S., and Toyoma, J., "Aftereffects of high-intensity DC stimulation on the electromechanical performance of ventricular muscle." *Am J Physiol*, vol. 267, no. 1 Pt 2, pp. H248-H258, 1994.

[69] Kodama, I., Sakuma, I., Shibata, N., Knisley, S. B., Niwa, R., and Honjo, H., "Regional differences in arrhythmogenic aftereffects of high intensity DC stimulation in the ventricles." *PACE*, vol. 23, no. 5, pp. 807-817, 2000.

[70] Neunlist, M. and Tung, L., "Dose-dependent reduction of cardiac transmembrane potential by high-intensity electrical shocks." *Am J Physiol*, vol. 273, no. 6 Pt 2, pp. H2817-H2825, 1997.

[71] Tekle, E., Astumian, R. D., and Chock, P. B., "Selective and asymmetric molecular transport across electroporated cell membranes." *Proc Natl Acad Sci USA*, vol. 91, no. 24, pp. 11512-11516, 1994.

[72] Cheek, E. R. and Fast, V. G., "Nonlinear changes of transmembrane potential during electrical shocks: Role of membrane electroporation." *Circ Res*, vol. 94, no. 2, pp. 208-214, 2004.

[73] Jones, J. L., Jones, R. E., and Balasky, G., "Microlesion formation in myocardial cells by high-intensity electric field stimulation." *Am J Physiol*, vol. 253, no. 2 Pt 2, pp. H480-H486, 1987.

[74] Nikolski, V. P., Sambelashvili, A. T., Krinsky, V. I., and Efimov, I. R., "Effects of electroporation on optically recorded transmembrane potential responses to high-intensity electrical shocks." *Am J Physiol Heart Circ Physiol*, vol. 286, no. 1, pp. H412-H418, 2004.

[75] Sambelashvili, A. T., Nikolski, V. P., and Efimov, I. R., "Virtual electrode theory explains pacing threshold increase caused by cardiac tissue damage." *Am J Physiol Heart Circ Physiol*, vol. 286, no. 6, pp. H2183-H2194, 2004.

[76] Salama, G. and Morad, M., "Merocyanine 540 as an optical probe of transmembrane electrical activity in the heart." *Science*, vol. 191, no. 4226, pp. 485-487, Feb.1976.

[77] Dillon, S. and Morad, M., "A new laser scanning system for measuring action potential propagation in the heart." *Science*, vol. 214, no. 4519, pp. 453-456, Oct.1981.

[78] Knisley, S. B., "Optical mapping of cardiac electrical stimulation." *J Electrocardiol*, vol. 30 Suppl pp. 11-18, 1998.

[79] Girouard, S. D., Pastore, J. M., Laurita, K. R., Gregory, K. W., and Rosenbaum, D. S., "Optical mapping in a new guinea pig model of ventricular tachycardia reveals mechanisms for multiple wavelengths in a single reentrant circuit." *Circulation*, vol. 93, no. 3, pp. 603-613, Feb.1996.

[80] Lin, S.-F., Abbas, R. A., and Wikswo, J. P., Jr., "High-resolution high-speed synchronous epifluorescence imaging of cardiac activation." *Rev Sci Instrum*, vol. 68, no. 1, pp. 213-217, 1997.

[81] Gray, R. A., Pertsov, A. M., and Jalife, J., "Spatial and temporal organization during cardiac fibrillation." *Nature*, vol. 392, no. 6671, pp. 75-78, 1998.

[82] Dillon, S. M., "Optical recordings in the rabbit heart show that defibrillation strength shocks prolong the duration of depolarization and the refractory period." *Circ Res*, vol. 69, no. 3, pp. 842-856, 1991.

[83] Morad, M. and Salama, G., "Optical probes of membrane potential in heart muscle." *J Physiol (Lond)*, vol. 292 pp. 267-295, 1979.

[84] Witkowski, F. X., Leon, L. J., Penkoske, P. A., Giles, W. R., Spano, M. L., and Winfree, A. T., "Spatiotemporal evolution of ventricular fibrillation." *Nature*, vol. 392, no. 6671, pp. 78-82, 1998.

[85] Entcheva, E., Eason, J., Efimov, I. R., Cheng, Y., Malkin, R., and Claydon, F., "Virtual electrode effects in transvenous defibrillation-modulation by structure and interface: Evidence from bidomain simulations and optical mapping." *J Cardiovasc Electrophysiol*, vol. 9, no. 9, pp. 949-961, 1998.

[86] Liu, Y., Cabo, C., Salomonsz, R., Delmar, M., Davidenko, J., and Jalife, J., "Effects of diacetyl monoxime on the electrical properties of sheep and guinea pig ventricular muscle." *Cardiovasc Res*, vol. 27, no. 11, pp. 1991-1997, 1993.

[87] Noguchi, K., Masumiya, H., Takahashi, K., Kameko, K., Higuchi, S., Tanaka, H., and Shigenobu, K., "Comparative effects of gallopamil and verapamil on the mechanical and electrophysiological parameters of isolated guinea-pig myocardium." *Can J Physiol Pharmacol*, vol. 75, no. 12, pp. 1316-1321, 1997.

[88] Li, T., Sperelakis, N., Teneick, R. E., and Solaro, R. J., "Effects of diacetyl monoxime on cardiac excitation-contraction coupling." *J Pharmacol Exp Ther*, vol. 232, no. 3, pp. 688-695, 1985.

[89] Gray, R. A., Ayers, G., and Jalife, J., "Video imaging of atrial defibrillation in the sheep heart." *Circulation*, vol. 95, no. 4, pp. 1038-1047, Feb.1997.

CHAPTER III

EFFECTS OF ELEVATED EXTRACELLULAR POTASSIUM ON THE STIMULATION MECHANISM OF DIASTOLIC CARDIAC TISSUE

Veniamin Y. Sidorov[1,2], Marcella C. Woods[3], John P. Wikswo[1,2,3,4]

[1]Department of Physics and Astronomy

[2]Vanderbilt Institute for Integrative Biosystems Research and Education

[3]Department of Biomedical Engineering

[4]Department of Molecular Physiology and Biophysics

Vanderbilt University, Nashville, Tennessee

Portions of this manuscript have been published in:

VY Sidorov, MC Woods, JP Wikswo. *Biophysical Journal*,
Vol. 84, No. 5, pp. 3470-3479, 2003.

3.1. Abstract

During cardiac disturbances such as ischemia and hyperkalemia, the extracellular potassium ion concentration is elevated. This in turn changes the resting transmembrane potential and affects the excitability of cardiac tissue. To test the hypothesis that extracellular potassium elevation also alters the stimulation mechanism, we used optical fluorescence imaging to examine the mechanism of diastolic anodal unipolar stimulation of cardiac tissue under 4 mM (normal) and 8 mM (elevated) extracellular potassium. We present several visualization methods that are useful for distinguishing between anodal-make and anodal-break excitation. In the 4 mM situation, stimulation occurred by the make, or stimulus-onset, mechanism that involved propagation out of the virtual cathodes. For 8 mM extracellular potassium, the break, or stimulus termination, mechanism occurred, with propagation out of the virtual anode. We conclude that elevated potassium, as might occur in myocardial ischemia, alters not only stimulation threshold but also the excitation mechanism for anodal stimulation.

3.2. Introduction

The importance of virtual electrode mechanisms in myocardial stimulation using unipolar electrodes has been demonstrated in previous studies [1-3]. The bidomain theory revealed that the unequal electrical anisotropies of the intracellular and extracellular spaces play the key role in the virtual electrode appearance [4-7]. During anodal stimulation of myocardium, a “dog bone” shaped region of hyperpolarization oriented transverse to the fiber direction arises centrally around the stimulating electrode. The “dog bone” shaped hyperpolarized region is flanked by two regions of depolarization in the convex portions of the “dog bone”.

Virtual electrode stimulation can occur by two mechanisms, known as make and break stimulation [3,7]. In make stimulation the excitation originates in the depolarized regions (virtual cathodes) at the onset of the stimulus. Conversely, in break stimulation the excitation originates in the hyperpolarized region (virtual anode) at the termination of the stimulus pulse. The make excitation mechanism only occurs when diastolic tissue is stimulated. Break excitation may be induced in both diastolic and systolic tissue by applying a long stimulus or may be induced by means of short stimulus applied during the repolarization phase of the action potential.

In break stimulation the wave front originates in the virtual anode because of charge diffusion from the virtual cathodes to the virtual anode area [8]. The closure of sodium channel inactivation gates due to depolarization leaves the virtual cathode regions unexcitable. However, the sodium channel inactivation gates are open in the hyperpolarized virtual anode region, causing the tissue to be excitable [9].

It is well established that elevated extracellular potassium ion concentration ($[K^+]_o$), which often accompanies such heart disturbances as ischemia [10] and hyperkalemia [11], changes the resting transmembrane potential and alters the excitability of cardiac tissue. In humans normal $[K^+]_o$ is 5.4 mM, and the resting membrane potential is –84 mV. Increasing $[K^+]_o$ to 10 mM elevates the resting membrane potential to approximately –67 mV [11]. However, at transmembrane potentials above –70 mV the sodium inactivation gates are closed, rendering the tissue unexcitable [12].

We hypothesize that elevated $[K^+]_o$, as might occur during ischemia, not only alters excitation but also affects the mechanism of stimulation. In this paper we report epifluorescence data from a series of experiments utilizing diastolic anodal stimulation in

which the effect of $[K^+]_o$ elevation was examined. We show that under normal $[K^+]_o$ conditions, the excitation mechanism is anode make. However, under elevated $[K^+]_o$ conditions the excitation mechanism is revealed as anode break.

3.3. Materials and Methods

3.3.1. Experimental Preparation and Protocol

All experiments were conducted in accordance with National Institutes of Health regulations for the ethical use of animals in research and were approved in advance by the Vanderbilt Institutional Animal Care and Use Committee.

New Zealand white rabbits (n=10) weighing 2 to 3 kg were first preanesthetized with intramuscular ketamine (50 mg/kg). The animals were then intravenously heparinized (1000 units) and subsequently anesthetized with sodium pentobarbital (50 mg/kg). Following a mid-sternal incision, the hearts were rapidly excised and moved to a Langendorff perfusion system. The ascending aorta was cannulated and secured in order to perfuse the coronary arteries in a retrograde manner with an oxygenated Tyrode's solution containing (in mM) 130 NaCl, 4 KCl, 2 $CaCl_2$, 1 $MgCl_2$, 1.5 NaH_2PO_4, 23 $NaHCO_3$, and 10 glucose. In each experiment, $[K^+]_o$ was initially 4 mM (normal) and was subsequently raised to 8 mM by adding the appropriate amount of KCl to the existing perfusate solution. After $[K^+]_o$ was raised, a 10-minute equilibration time elapsed before subsequent data collection. The perfusate was continuously bubbled with a 95% oxygen/5% carbon dioxide mixture, and the temperature and pH were continuously maintained at 37°C and 7.4±0.05, respectively. Coronary perfusion pressure was regulated to 50 mm Hg. The hearts were exposed to the air during the experiments.

Following an equilibration time of 20 minutes to allow sinus rhythm stabilization, the hearts were stained with 200 μL of di-4-ANEPPS (Molecular Probes, Eugene, OR) stock solution (0.5 mg/mL dimethyl sulfoxide) administered via a bubble trap above the aorta. Diacetyl monoxime (DAM) was added to the Tyrode's solution at a concentration of 15 mM to block muscle contraction and, hence, lessen motion artifacts in the fluorescence data. In all experiments only the anterior left ventricle was imaged.

Electrical stimulation was conducted via both bipolar and unipolar electrodes. The bipolar pacing electrode (S1) was constructed from two platinum wires (0.25 mm diameter) enclosed in glass with only the tips of the wires exposed. The distance between the two tips was 1 mm. The bipolar pacing electrode was placed on the right ventricle close to septum, 8 to 9 mm from the unipolar testing electrode. The unipolar testing electrode (S2), also made from platinum wire (0.25 mm diameter), was positioned centrally on the anterior left ventricle. The camera field of view was centered around the testing electrode. A small piece of titanium mesh placed against the posterior left ventricle served as the reference testing electrode. The electrical stimuli in the experiments were provided by computer-controlled current sources (Bloom Associates Ltd., Narberth, PA). The heart was constantly paced at a 350 ms cycle length with 2 ms electrical stimuli (S1) of strength equal to two times the diastolic stimulation threshold. Anodal test stimuli (S2) of 0.1-10 mA amplitude and 10 ms duration were applied at a S1 – S2 coupling interval of 350 ms, unless otherwise stated.

To measure the transmembrane potential directly, ten additional experiments were conducted using microelectrodes. Action potentials at multiple sites were recorded by using "floating" 3 M KCl-filled microelectrodes. The microelectrodes were pulled from

borosilicate glass capillaries (World Precision Instruments, Sarasota, FL) by a micropipette puller (Model P80/PC, Sutter Instrument Co., Novato, CA). The microelectrode tips were mounted on 50 μm-diameter platinum wire. The Ag/AgCl reference electrode, 8 mm in diameter and 1 mm in thickness (EP8, World Precision Instruments), was placed in the left ventricular cavity. The electrodes were connected to the input probes of a dual differential electrometer (model FD223, World Precision Instruments). The signals were digitized, visualized, recorded, and analyzed by a digital oscilloscope (Infinium, Hewlett-Packard Co., Palo Alto, CA). The sampling rate for data acquisition was 10 kHz. All microelectrode measurements were conducted on the anterior left ventricle using the same perfusion setup as for the optical studies.

3.3.2. Optical Imaging and Data Analysis

The fluorescence was excited by a diode-pumped, solid-state laser (Verdi, Coherent Inc., Santa Clara, CA) at a wavelength of 532 nm. The illumination was delivered to the heart with a double beam illumination scheme [9]. The emitted light was passed through a cutoff filter (#25 Red, 607 nm, Tiffen Co., Hauppauge, NY) and imaged with a high-speed CCD camera (Model CA D1-0128T, Dalsa Inc., Waterloo, ON, Canada). The faceplate of the camera was cooled via a 15˚C refrigerated bath. The data were acquired at 2-ms intervals with 12-bit resolution from 128 × 128 sites simultaneously over a 12 × 12 mm area. The digitized pixel intensity from the digital camera was transferred to a PCI bus-master frame grabber board (IC-PCI, Imaging Technology Inc., Bedford, MA) mounted in an IBM-compatible personal computer (Dell Precision Workstation 610, Dell Computer Corp., Round Rock, TX).

The optical data were first normalized pixel-by-pixel according to fluorescence changes during the last pacing response and then the resulting images were voltage-calibrated according to the microelectrode measurements. The resting membrane potential and action potential amplitude were –85 mV and 112 mV under normal $[K^+]_o$ (4 mM) and –68 mV and 95 mV under elevated $[K^+]_o$ (8 mM), respectively. All data presented in this paper have been filtered to improve the signal-to-noise ratio. Data depicting the transmembrane potential distribution were spatially filtered with an 8 × 8 Gaussian filter. These spatially filtered data were used to compute the optical dV/dt_{max} measurements.

We utilized time-space analysis [13-15] to examine the stimulation mechanism. To explore the evolution of electrical activity during stimulation, time-space plots were constructed for lines along and transverse to the fiber direction. The intersection of these two lines roughly coincided with the position of the testing electrode. To construct the time-space plots, the optical data were pre-processed by applying a 5 × 5 Gaussian spatial filter and a 5-point mean temporal filter two times.

3.4. Results

3.4.1. Moderate Anodal Stimulation of Diastolic Tissue for Normal $[K^+]_o$

Figure 3.1 illustrates the tissue response to 6 mA amplitude (3× threshold), 10 ms diastolic anodal stimulation delivered at an S1-S2 coupling interval of 350 ms.

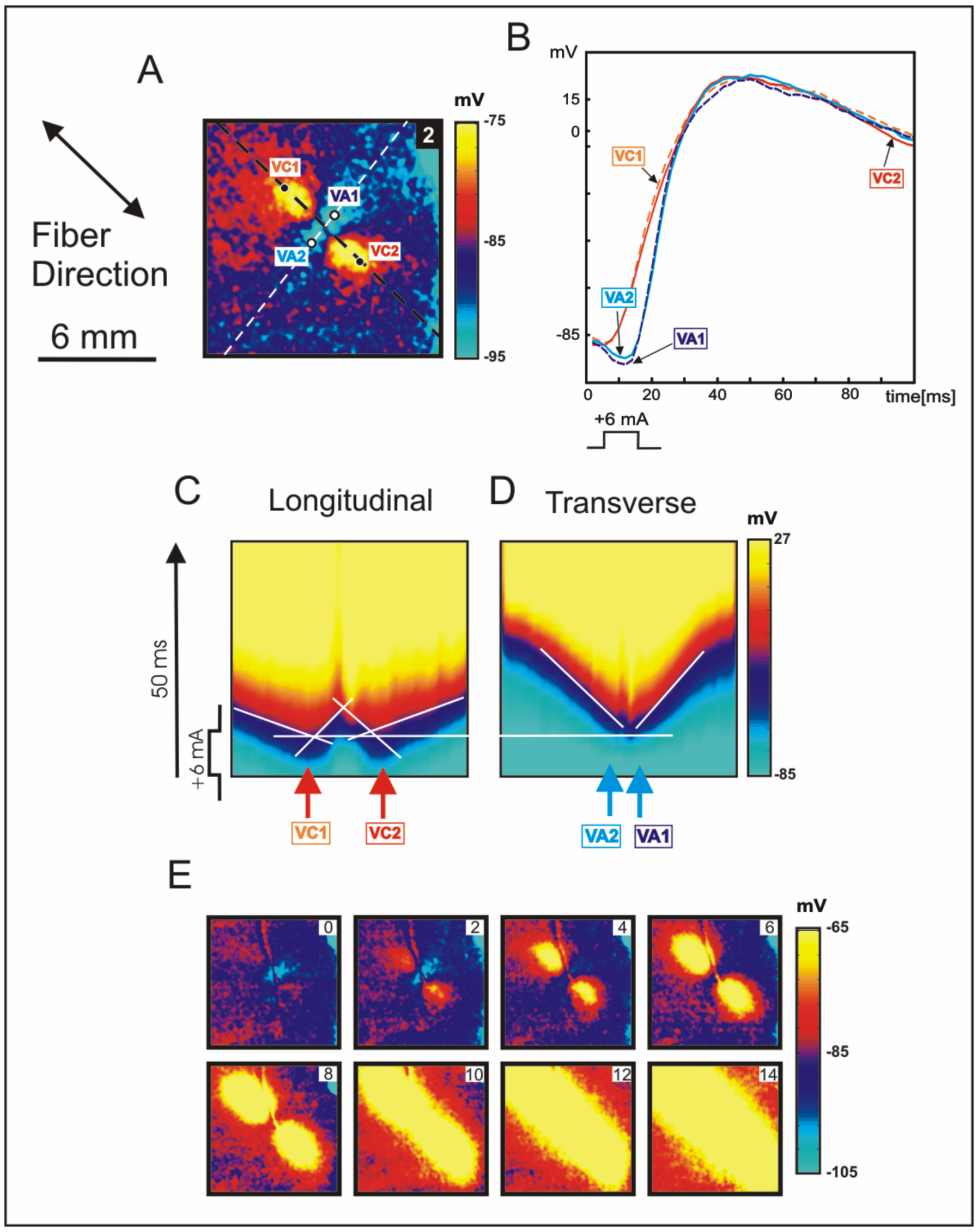

Figure 3.1. Anodal-make response to diastolic 3× threshold stimulation for normal $[K^+]_o$ (4 mM). The anodal S2 stimulus was 6 mA in amplitude, 10 ms in duration, and applied at an S1-S2 coupling interval of 350 ms. *(A)* Image of the transmembrane potential distribution 2 ms after the onset of S2 point stimulation at the center of the image. *(B)* Four representative traces recorded within the virtual cathode (red) and virtual anode (blue) areas. The pixel locations for these traces are marked with white and black dots in panel A. *(C and D)* Time-space plots for lines longitudinal and transverse to the fiber direction (white and black dashed lines in panel *A*). The white horizontal isochronal line corresponds to 8 ms after the beginning of S2. The white slanted lines in panel *C* demonstrate the inward and outward propagation velocity along the fiber direction. The white slanted lines in *D* demonstrate the outward propagation velocity transverse to the fiber direction. The blue and red arrows indicate the location of the pixels depicted by black and white dots in panel *A*. *(E)* The transmembrane potential distribution as a function of time. The numbers in the upper right represent the time [ms] since the onset of S2.

The image of the transmembrane potential distribution during stimulation is shown in Figure 3.1 *A*. The experimental data correspond to results previously reported [1-3]. The transmembrane potential distribution map exhibits the expected central "dog bone" shaped virtual anode (VA) and a pair of adjacent virtual cathodes (VC). Figure 3.1 *B* shows four superimposed optical signals: two at VC (red) locations and two at VA (blue) locations. The VC action potentials initiate at the beginning of the stimulus. The VA traces reveal initial hyperpolarization, such that the VA action potentials initiate long after the VC action potentials. The peak rate of rise, dV/dt_{max}, is greater for the VA action potentials than for the VC ones. Traces were selected for calculation by random sampling in the VA and VC regions. For eight traces in the VA region dV/dt_{max} is 12.3±0.4 mV/ms, while dV/dt_{max} is 6.0±0.8 mV/ms for eight traces in the VC regions.

The time-space plots for lines longitudinal and transverse to the fiber direction are presented in Figure 3.1, *C* and *D*, respectively. These lines are depicted with white and black dashed lines in Figure 3.1 A. Figure 3.1 C shows that excitation propagates from two locations that correspond spatially to the virtual cathodes in Figure 3.1 *A*. The red arrows in Figure 3.1 *C* indicate the two pixel locations (VC1 and VC2) of the VC traces shown in Figure 3.1 *B*. Similarly, the blue arrows in Figure 3.1 *D* show the position of the two pixels VA1 and VA2.

To compare the activation time of the VC and VA regions, we drew an isochronal line (horizontal) in both Figure 3.1 *C* and *D*. One can see that activation first begins in the VC regions. The slope of the line tangent to the depolarization front (drawn approximately at the -30 mV contour) reveals the conduction velocity along (Figure 3.1 *C*) and transverse (Figure 3.1 *D*) to the fiber direction. Conduction velocity is inversely

related to the slope of the lines drawn in the time-space plots. It is seen that propagation from the VC regions is faster in the outward direction than inward toward the central hyperpolarized VA region (Figure 3.1 *C*). Outward conduction velocities indicated by the drawn lines are 65 and 61 cm/s whereas the inward conduction velocities for the drawn lines are 27 and 24 cm/s. As was expected, there is anisotropy in the conduction velocity along and transverse to the fiber direction. Figure 3.1 *C* shows faster conduction longitudinal to the fiber direction in comparison with transverse to the fiber direction, as shown in Figure 3.1 *D*. The two transverse conduction velocities are 21 and 25 cm/s. Our longitudinal and transverse conduction velocity measurements are in agreement with those computed by Boersma *et al.* [16].

Images of the transmembrane potential distribution at 2 ms intervals following the onset of S2 are shown in Figure 3.1 *E*. Excitation originates in the two VC regions, indicating anodal-make stimulation.

3.4.2. Threshold Anodal Stimulation of Diastolic Tissue for Normal $[K^+]_o$

In contrast to the results for moderate anodal stimulation described in Figure 3.1, in most experiments we did not observe symmetric activation patterns for threshold anodal stimulation. In the particular experiment described, the threshold anodal stimulus was a 2 mA, 10 ms duration pulse delivered at an S1-S2 coupling interval of 350 ms.

Figure 3.2 demonstrates the typical situation in which one of the VC regions reveals more positive polarization than the other. This ‘stronger’ VC region is the site of excitation initiation. The time traces in Figure 3.2 *B* show delay in excitation between the two VC areas. Activation is first observed for VC2, and the resulting wave front initiates activation in the VA region (blue traces VA1 and VA2). VC1 activation occurs

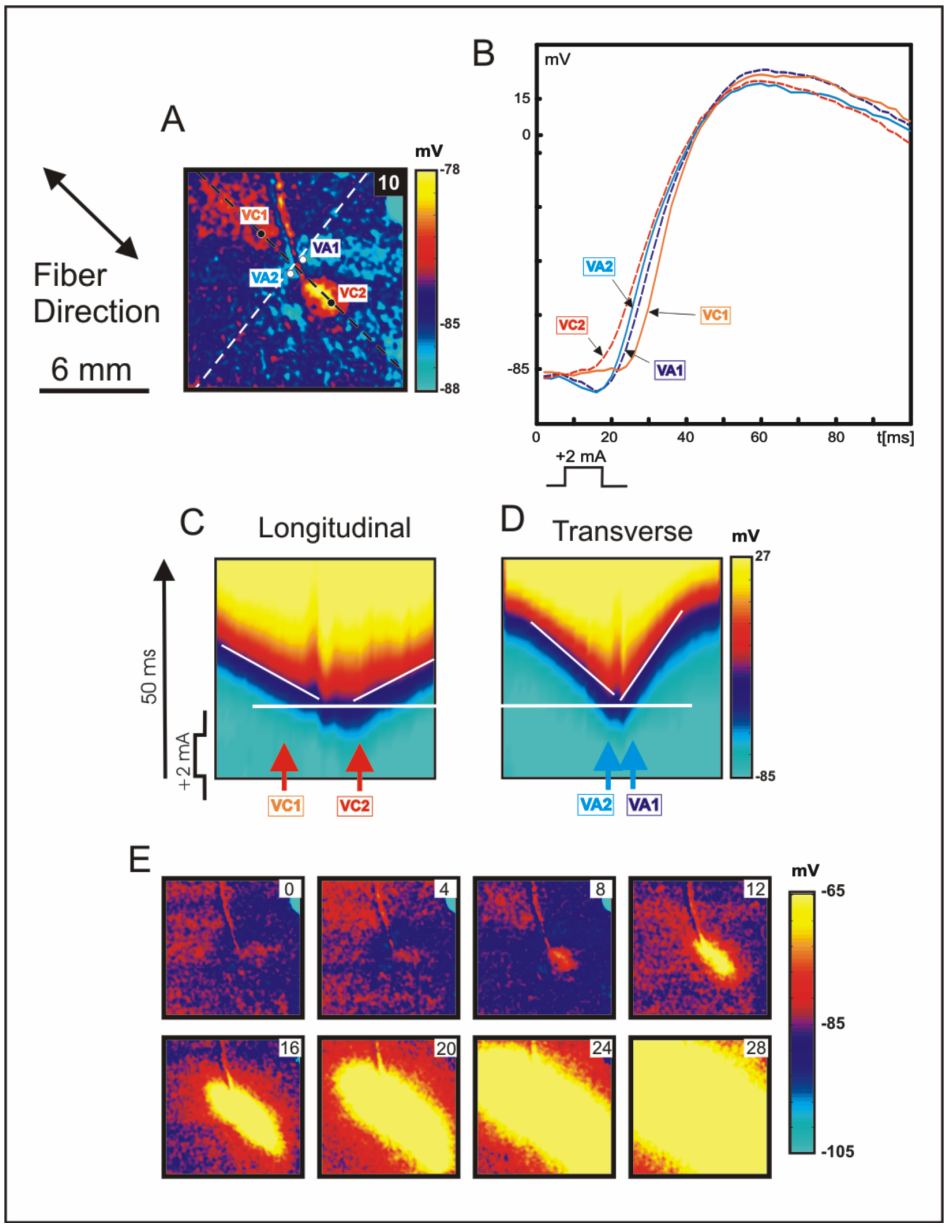

Figure 3.2. Anodal-make response to diastolic threshold stimulation for normal $[K^+]_o$ (4 mM). The anodal S2 stimulus was 2 mA in amplitude, 10 ms in duration, and applied at an S1-S2 coupling interval of 350 ms. *(A)* Image of the transmembrane potential distribution 10 ms after the onset of S2 point stimulation at the center of the image. *(B)* Four representative traces recorded within the virtual cathode (red) and virtual anode (blue) areas. The pixel locations for these traces are marked with white and black dots in panel A. *(C and D)* Time-space plots for lines longitudinal and transverse to the fiber direction (white and black dashed lines in panel *A*). The white horizontal isochronal line corresponds to 16 ms after the beginning of S2. The white slanted lines demonstrate propagation velocity along (panel *C*) and transverse (panel *D*) to the fiber direction. The blue and red arrows indicate the location of the pixels depicted by black and white dots in panel A. *(E)* The transmembrane potential distribution as a function of time. The numbers in the upper right represent the time [ms] since the onset of S2.

last. As was the case in Figure 3.1, the peak rate of rise is greater for the VA action potentials than for the VC ones. However, the magnitude of and the difference in dV/dt_{max} for the VA and VC regions are smaller for threshold stimulation. For eight randomly selected traces in the VA region dV/dt_{max} is 6.3±0.5 mV/ms, whereas for eight randomly selected traces in the VC regions, dV/dt_{max} is 4.8±0.4 mV/ms.

Figure 3.2 *C* and *D* show time-space plots for lines along and transverse to the fiber direction. Lines tangent to the depolarization front are drawn (at approximately the -30 mV contour) to show the conduction velocities. Activation is first observed in the VC2 area (Figure 3.2 *C*), followed by activation in the VA regions (Figure 3.2 *D*). Activation in the VC1 area is delayed (Figure 3.2 *C*). These time-space plots again reveal the expected anisotropic conduction velocity along (43 and 46 cm/s) and transverse (27 and 17 cm/s) to the fiber direction. Note the marked decrease in longitudinal conduction velocity for threshold stimulation in comparison with moderate stimulation (Figure 3.1 *C*). Both the time-space plot in the longitudinal direction (Figure 3.2 *C*) and the succession of the transmembrane potential images (Figure 3.2 *E*) also demonstrate asymmetric anodal-make excitation for threshold anodal stimulation.

3.4.3. Long Duration, Strong Anodal Stimulation of Refractory Tissue for Normal $[K^+]_o$

To obtain an episode of anodal-break stimulation, a 20 mA amplitude (10× threshold), 150 ms anodal S2 stimulus was delivered to refractory tissue using an S1-S2 interval of 80 ms.

Figure 3.3 *A* demonstrates the stimulation timing (black arrows at the bottom) and tissue response to S1 and S2 stimulation. The red trace corresponds to the virtual cathode pixel location VC1 while the blue trace corresponds to the virtual anode pixel location

VA2, as depicted in Figure 3.3 *B*, showing the transmembrane potential distribution 82 ms after the onset of S2. The expected "dog bone" shaped virtual anode and pair of adjacent virtual cathodes are shown.

The virtual cathode and virtual anode optical traces are presented in Figure 3.3 *C*. The beginning of the time-scale corresponds to the 130th ms of the S2 pulse (20 ms prior to the stimulus termination). During S2 stimulation, the voltage difference between the virtual anodes and virtual cathodes is approximately 40 mV. Immediately after S2 termination (second dotted black line in Figure 3.3 *A*), the voltage in the virtual cathode areas decreases (red traces), whereas the virtual anode voltage (blue traces) increases, indicating charge diffusion from the virtual cathodes to the virtual anode area. After the VC and VA traces intersect, the voltages in the virtual anode region are greater than those in the virtual cathode regions, suggesting the initiation of excitation in the virtual anode region. Figure 3.3 *F* shows images of transmembrane potential distribution as a function of time. The frame labeled 16 ms approximately corresponds to the time at which the VC and VA traces intersect in Figure 3.3 *C*. Note that the final activation pattern in the series, at 36 ms, shows dog-bone-shaped activation, consistent with a dog-bone-shaped virtual anode and anodal-break excitation.

The virtual cathodes are revealed in the longitudinal time-space plot (Figure 3.3 *D*) as red areas (indicated with red arrows) during stimulation. The color change of the virtual cathode

regions from red to blue after the stimulus is turned off reflects the diffusion of positive charge into the more negative virtual anode area, as was discussed for Figure 3.3 *C*. The isochronal lines (horizontal white lines) reveal that activation in the virtual anode occurs

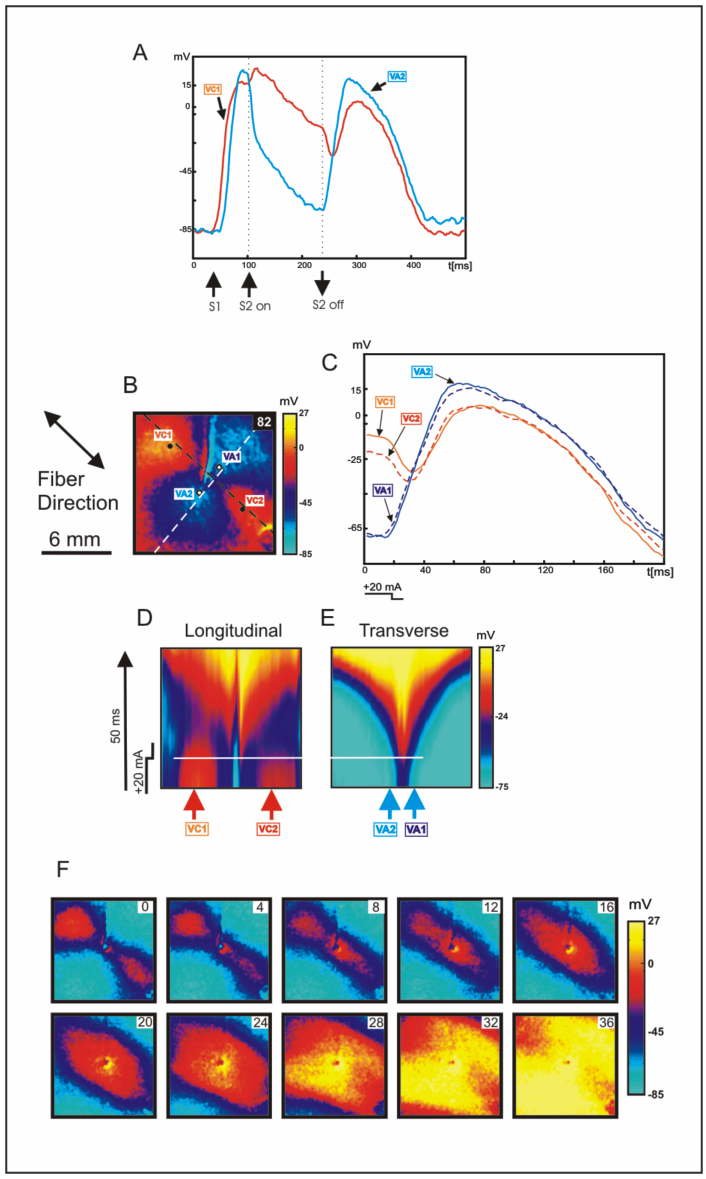

Figure 3.3. Anodal-break response to strong systolic stimulation for normal $[K^+]_o$ (4 mM). The anodal S2 stimulus was 20 mA in amplitude, 150 ms in duration, and applied at an S1-S2 coupling interval of 80 ms. *(A)* Representative traces recorded within the virtual cathode (red) and virtual anode (blue) area depicting the response to S1 and S2 stimulation. The black arrows underneath the plot show the stimulus timing. *(B)* Image of the transmembrane potential distribution 82 ms after the onset of S2 point stimulation at the center of the image. The pixel locations for the traces in *A* and *C* are indicated by the white and black dots. *(C)* Four representative traces recorded within the virtual cathode (red) and virtual anode (blue) areas depicting the response at the end of S2 and following S2 termination. *(D and E)* Time-space plots for lines longitudinal and transverse to the fiber direction (white and black dashed lines in panel *B*). The white horizontal isochronal line corresponds to the termination of S2. The white slanted lines demonstrate propagation velocity along (panel *D*) and transverse (panel *E*) to the fiber direction. The blue and red arrows indicate the location of the pixels depicted by black and white dots in panel *B*. Data artifacts caused by the testing electrode lie underneath the black W's in the images of panels *B* and *D*. *(F)* The transmembrane potential distribution as a function of time. The numbers in the upper right represent the time [ms] since the termination of S2.

earlier (Figure 3.3 *E*) than in the virtual cathodes (Figure 3.3 *D*), again indicating anodal-break stimulation. Conduction velocities were not computed for Figure 3.3, *D* and *E*, because there are no stationary velocities to measure.

3.4.4. Threshold Anodal Stimulation of Diastolic Tissue for Elevated $[K^+]_o$

Figure 3.4 illustrates the tissue response to anodal threshold stimulation during diastole for 8 mM $[K^+]_o$ conditions.

Figure 3.4 *A* shows the transmembrane potential distribution during a 6 mA (threshold), 10 ms anodal S2 stimulus using an S1-S2 interval of 350 ms for elevated $[K^+]_o$. The polarization pattern is very similar to that produced with the exact same stimulation parameters for normal $[K^+]_o$ (Figure 3.1 *A*). A hyperpolarized region lies around the point of stimulation, and a pair of adjacent depolarized regions is oriented along the fiber direction.

Four representative traces from the virtual cathodes (red) and virtual anode (blue) region are depicted in Figure 3.4 *B*. The optical signals initially reveal depolarization in the VC areas and hyperpolarization in the VA area. Moreover, although the VC regions are distal from the S2 electrode location, the magnitude of the VC depolarization is significantly larger than the magnitude of the hyperpolarization in the VA region, which surrounds the S2 electrode site. Following S2 termination, the VC traces reveal slight negative polarization whereas the VA traces exhibit depolarization. After the VC and VA traces intersect, the VA optical signals show activation prior to the VC signals. This behavior is similar to that shown for stimulation of refractory tissue in normal $[K^+]_o$ (Figure 3.3 *C*), suggesting excitation initiation in the VA region. Because of the biphasic

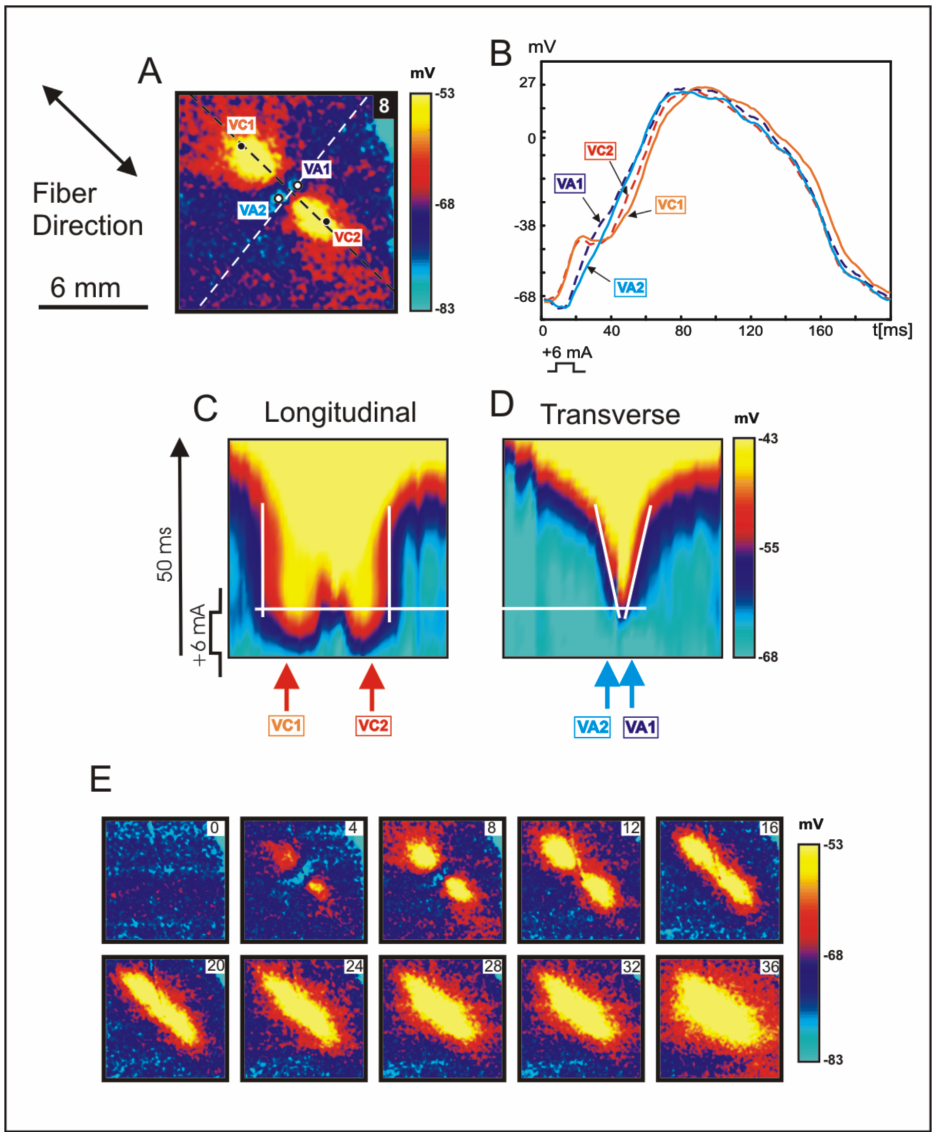

Figure 3.4. Anodal-break response to diastolic threshold stimulation for elevated $[K^+]_o$ (8 mM). The anodal S2 stimulus was 6 mA in amplitude, 10 ms in duration, and applied at an S1-S2 coupling interval of 350 ms. *(A)* Image of the transmembrane potential distribution 8 ms after the onset of S2 point stimulation at the center of the image. *(B)* Four representative traces recorded within the virtual cathode (red) and virtual anode (blue) areas. The pixel locations for these traces are marked with white and black dots in panel A. *(C and D)* Time-space plots for lines longitudinal and transverse to the fiber direction (white and black dashed lines in panel *A*). The white horizontal isochronal line corresponds to the termination of S2. The white slanted lines demonstrate propagation velocity along (panel *C*) and transverse (panel *D*) to the fiber direction. The blue and red arrows indicate the location of the pixels depicted by black and white dots in panel *A*. *(E)* The transmembrane potential distribution as a function of time expressed as a percentage of the fluorescence intensity and represented by a false-color scale. The numbers in the upper right represent the time [ms] since the onset of S2.

nature of the VC time traces, dV/dt_{max} was not measured for the virtual electrode regions for the elevated $[K^+]_o$ situation.

Time-space plots for lines longitudinal and transverse to the fiber direction are presented in Figure 3.4, *C* and *D*. In Figure 3.4 *C* the slope of the tangent line of the depolarization edge (drawn approximately at the -55 mV contour) reveals no longitudinal wave front propagation away from the S2 electrode site for 25 ms after S2 termination. However, the time-space plot in Figure 3.4 *D* shows very slow transverse propagation (6 and 5 cm/s) out of the virtual anode during this time period.

Images of the transmembrane potential distribution as a function of time are presented in Figure 3.4 *E*. The stimulus was turned on in frame 0 and was terminated 10 ms later, between the frames depicting 8 and 12 ms. Although the tissue is diastolic, S2 fails to initiate excitation in the VC areas. Instead, following the cessation of S2 (12 ms frame), the charge in the VC areas begins to diffuse into the hyperpolarized VA region located between the VC areas (16 – 36 ms frames), and excitation is initiated in the VA (16 ms frame).

It should be noted that the longitudinal axis of the spreading excitation wave (Figure 3.5 *A*, blue line) forms an approximate 35° angle with the VC location axis (Figure 3.5 *A*, green line), which was assumed to coincide with the fiber direction. However, for normal $[K^+]_o$ (4 mM), the main ellipse axis of the propagating wave front concurred with the VC location axis (Figure 3.5 *B*, green line). The data depicted for both the elevated $[K^+]_o$ (Figure 3.5 *A*) and normal $[K^+]_o$ (Figure 3.5 *B*) situations are the same data described in Figure 3.4and Figure 3.1, respectively. In both cases the anodal S2 was a 6 mA, 10 ms pulse delivered at an S1-S2 interval of 350 ms.

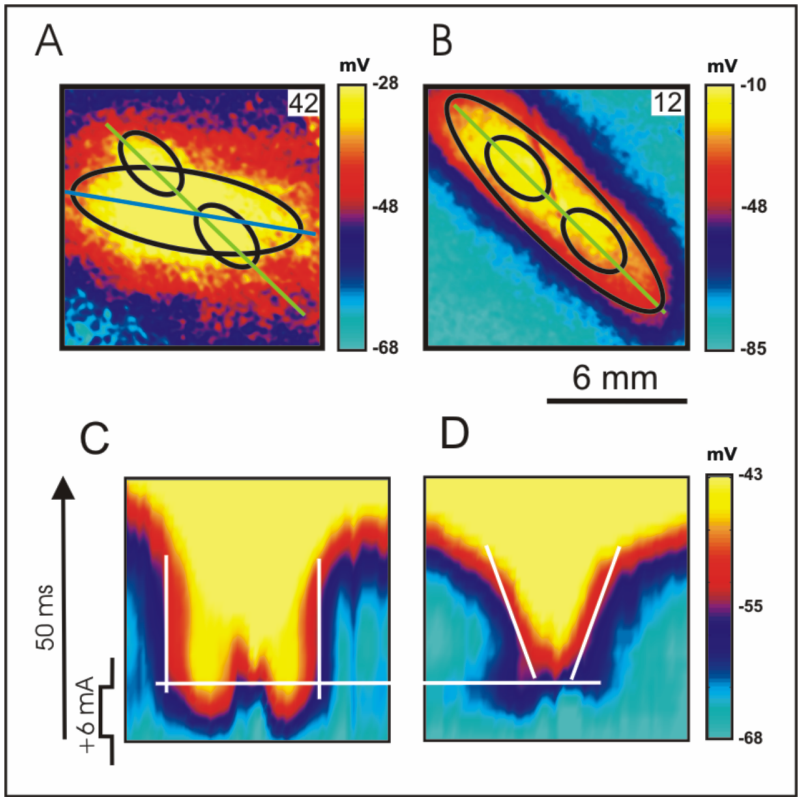

Figure 3.5. Wave front and virtual cathode location for normal (4 mM) and elevated (8 mM) $[K^+]_o$. Images of the transmembrane potential distribution for (*A*) elevated and (*B*) normal $[K^+]_o$. The smaller ellipses depict the virtual cathode locations, and the large ellipses describe the propagating wave fronts. *(C and D)* The time-space plots constructed along the (*C*) green and (*D*) blue lines in panel *A*. The white horizontal isochronal line corresponds to the termination of S2. The white slanted lines show propagation velocity along the axes in panel *A*.

Figure 3.5 also demonstrates time-space plots for the VC location axis (Figure 3.5 *C*) and the main axis of the spreading excitation wave (Figure 3.5 *D*) for the elevated $[K^+]_o$ situation (Figure 3.5 *A*). Figure 3.5 *D* shows excitation propagation after stimulus cessation, but no propagation is observed along the VC axis during the same time period (Figure 3.5 *C*). It should also be mentioned that slope of the tangent lines in Figure 3.5 *D* reveals faster conduction velocity (9 cm/s) in comparison with those in Figure 3.4 *D* for transverse to the fiber direction.

3.4.5. Effect of Elevated $[K^+]_o$ on the Transmembrane Potential

Figure 3.6 illustrates the effects of elevated $[K^+]_o$ on the transmembrane potential. Elevation of $[K^+]_o$ from 4 mM (Figure 3.6 *A*) to 8 mM (Figure 3.6 *B*) raises the resting membrane potential from -84.8±2.3 mV (75 measurements from 37 cells of 8 hearts) to -67.5±2.3 mV (66 measurements from 27 cells of 7 hearts) and reduces the action potential amplitude from 112.0±4.0 mV (74 measurements from 36 cells of 9 hearts) to 95.5±2.7 mV (68 measurements from 28 cells of 7 hearts).

3.5. Discussion

Cathodal and anodal make and break stimulation was first demonstrated by Dekker in 1970 [17]. The cellular mechanisms of these four modes for stimulating cardiac tissue remained a mystery until Roth's 1995 modeling analysis [7] demonstrated the role played by the differences between the anisotropies of the intracellular and extracellular spaces in the response of the cardiac bidomain to point stimulation. The subsequent measurements by Wikswo et al. [3] provided clear evidence that the response to suprathreshold point stimulation in the isolated rabbit heart was consistent with the

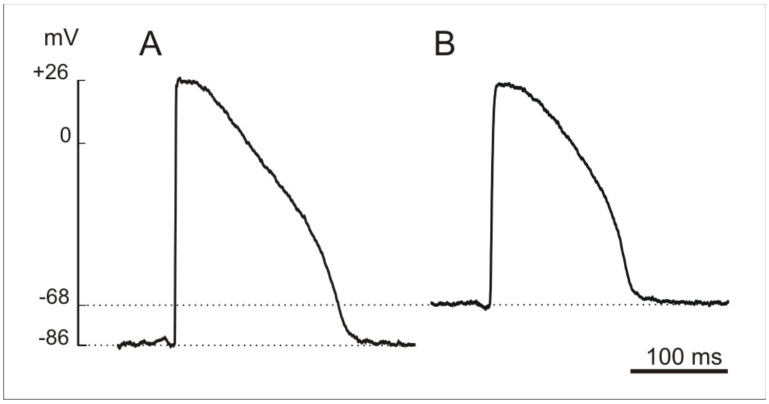

Figure 3.6. Microelectrode measurements of transmembrane potential for normal (4 mM) and elevated (8 mM) $[K^+]_o$. Typical action potentials recorded using microelectrodes for *(A)* normal and *(B)* elevated $[K^+]_o$.

explanation of the four modes provided by Roth.

Nikolski et al. [18] report 'paradoxical" results for threshold stimulation of cardiac tissue. In this paper, we demonstrate that the identification of the mode of stimulation for threshold stimulation is difficult, in part because the VC and VA areas are smaller and less pronounced and hence less easily delineated, because charge diffusion does not necessarily lead to a rapid response of the tissue, and because heterogeneities in the tissue excitability can lead to asymmetries in the threshold stimulus response. Recognizing the possible difficulty in interpreting optical recordings of excitation patterns for threshold stimuli, we have developed a series of visualization techniques and criteria that allow us to discriminate between anodal and cathodal make and break excitation. The examples we provide in Figure 3.1 through Figure 3.4 were chosen to provide a pedagogically rigorous explanation of these techniques and criteria.

Furthermore, to provide a means to adjust the response of the tissue to the stimulation while keeping the stimulus parameters constant, we have conducted a series of experiments using elevated extracellular potassium, which raises the transmembrane potential and in turn increases the sodium channel inactivation. Partial inactivation of the sodium channels is known to increase the threshold and to slow the rise of the action potential [19]. The traces presented in Figure 3.4 *B* resulting from anodal stimulation in high $[K^+]_o$ clearly show significant deceleration of the optical action potential upstrokes in comparison to those for normal $[K^+]_o$ in Figure 3.1 *B*. Under 4 mM $[K^+]_o$, dV/dt_{max} for ten randomly selected traces is 8.7±0.5 mV/ms, whereas under 8 mM $[K^+]_o$ dV/dt_{max} decreases to 5.2±0.4 mV/ms. For the microelectrode measurements dV/dt_{max} is 174.8±30 mV/ms (mean±std, n=22) and 40.3±5.4 mV/ms (mean±std, n=26) for normal and

elevated $[K^+]_o$, respectively. This deceleration of action potential upstroke is a consequence of the depolarizing effect of elevated $[K^+]_o$ on the resting membrane potential and also may be the result of a voltage-independent effect on the inwardly rectifying K^+ current [20,21]. The discrepancy between the microelectrode and optical dV/dt_{max} measurements is due to the high sampling rate of the microelectrode data and fluorescence averaging within a volume of tissue in the optical data [22].

The traces in Figure 3.4 *B* also demonstrate that for a 6 mA stimulus, because of the slowed upstroke caused by elevated $[K^+]_o$, the VC regions cannot sufficiently depolarize to reach threshold during the 10 ms stimulus duration. The hyperpolarization in the VA area appears faster that the VC depolarization, but is a much weaker response. Under the condition of the partially elevated resting membrane potential, the hyperpolarization opens voltage-dependent sodium channel inactivation gates and causes increased excitability in the VA region. Thus, although the depolarization in the VC areas is too weak to overcome threshold and initiate an action potential, there is sufficient charge accumulation in the VC areas to stimulate the VA region following S2 termination, resulting in anodal-break stimulation.

In a recent study of acute global ischemia [23], the authors found that ischemia significantly changed repolarization characteristics but only slightly decreased conduction. This is in sharp contrast with our findings of obvious slowed conduction during elevated $[K^+]_o$. The Cheng *et al.* ischemic model is created by decreasing perfusion flow rate to 25% of normal. In this decreased flow state, we believe there may still be enough flow to allow extracellular potassium to wash out. Therefore $[K^+]_o$ may

not have been significantly elevated in their study, explaining why they do not see decelerated action potential upstrokes.

The elevation of $[K^+]_o$ has biphasic effect on excitability. As was shown in pigs, the ventricular threshold of excitability decreases when the plasma $[K^+]_o$ is moderately elevated, but increases sharply when plasma $[K^+]_o$ exceeds 7 to 9 mM [24]. For intermediate concentrations of $[K^+]_o$ (6 – 7 mM) we observed make excitation for 10-ms threshold stimulation (data not shown), as was the case for the normal 4 mM $[K^+]_o$ situation. Therefore, in our rabbit experiments we analyzed the mechanism of diastolic stimulation in the $[K^+]_o$ range of 8 – 9 mM. We observed anodal-break stimulation for 8 mM $[K^+]_o$ in 7 of the 10 experiments. In these cases elevation of $[K^+]_o$ from 4 mM to 8 mM increased the anodal threshold from 1.53 ± 0.5 mA (mean ± std, n=7) to 3.41 ± 1.3 mA (mean ± std, n=7) (two-tailed, paired Student's t-test, $P<0.01$). In the remaining 3 experiments, in order to observe anodal-break stimulation $[K^+]_o$ had to be increased to 9 mM. For these hearts elevation of $[K^+]_o$ from 4 mM to 9 mM increased the anodal threshold from 1.33 ± 0.7 mA (mean ± std, n=3) to 2.77 ± 0.9 mA (mean ± std, n=3) (two-tailed, paired Student's t-test, $P<0.05$). Subsequent elevation of $[K^+]_o$ above 9 mM significantly decreases the signal-to-noise ratio. When $[K^+]_o$ was raised to 12 mM, tissue excitability was completely depressed, and stimuli as large as 10 mA elicited no response.

According to anatomical architecture, myocardium is characterized by fiber axis rotation. This rotation is counterclockwise from the epicardial to endocardial surface with a rotation angle of approximately 120˚ [25,26]. Additionally, optical recordings from the heart surface are actually weighted averages of fluorescence from a tissue depth that has

been estimated to be 300 – 500 μm [1,22] all the way up to 1 – 2 mm [27-30]. In our experiments with elevated $[K^+]_o$, the anodal-break stimulated propagating wave front forms an ellipse with axes that do not coincide with the axes longitudinal and transverse to the fiber direction (Figure 3.5 *A*). This apparent discrepancy may be explained by wave front propagation in deeper myocardial layers.

Though beyond the scope of this paper, it may be worthwhile to conduct detailed studies of the ionic mechanisms that are involved in the conversion of the stimulation mechanism during elevated $[K^+]_o$. Such experimental studies may include the addition of pharmacological sodium channel blockers and the use of another excitation-contraction decoupler, such as cytochalasin D. However, little modeling work exists to study the effects of elevated $[K^+]_o$. Detailed studies of the involved ionic mechanisms would be best and most easily conducted by mathematical modeling due to the complexity of such experimental undertakings.

Because $[K^+]_o$ elevation accompanies ischemia, our data suggest break stimulation as a likely mechanism for threshold unipolar anodal stimulation not only during hyperkalemia but also during ischemic events. Given the increased recognition of the role of break excitation in cardiac defibrillation [31], and the presence of increased extracellular potassium during fibrillation, it may be worthwhile to examine in greater detail the role of elevated $[K^+]_o$ in the defibrillation process.

3.6. Limitations of the Study

As described earlier, optical signals originate not only from surface epicardial layers but also from layers deeper beneath the surface. The resulting three-dimensional data and the three-dimensional myocardial structure make the image patterns more

difficult to interpret. Cryoablation of the endocardium to obtain a preparation in which only a thin epicardial layer is viable would help to alleviate this problem [29,32-37].

Current optical imaging techniques require the use of an excitation-contraction decoupler, such as DAM, to eliminate motion artifacts in data collection. DAM is known to change several membrane conductances, causing some electrophysiological effects including decreased action potential duration [38], decreased dV/dt_{max} [39], and decreased conduction velocity [36]. While the use of DAM may quantitatively affect our results, comparison of data in normal and high $[K^+]_o$ situations is valid because DAM was used in all experiments.

When we elevated $[K^+]_o$, we did not alter other ion concentrations in the perfusate in order to maintain the same osmolarity as the original 4 mM $[K^+]_o$ perfusate. The high $[K^+]_o$ perfusate, therefore, has a higher osmolarity than the normal $[K^+]_o$ perfusate. However, a change in $[K^+]_o$ from 4 mM to 8 mM increases the osmolarity by only 8 mOsm/L, or a total change of 2.4%. Such a small change should have minimal effect upon the myocardial cells.

3.7. Acknowledgements

We would like to thank Mark-Anthony P. Bray, Jonathan M. Gilligan, and Bradley J. Roth for their encouragement and numerous suggestions.

This work was supported by the National Institutes of Health (R01-HL58241-05 and 5T32-HL07411), the American Heart Association (0215128B), and the Academic Venture Capital Fund of Vanderbilt University.

3.8. References

[1] Knisley, S. B., "Transmembrane voltage changes during unipolar stimulation of rabbit ventricle." *Circ Res*, vol. 77, no. 6, pp. 1229-1239, 1995.

[2] Neunlist, M. and Tung, L., "Spatial distribution of cardiac transmembrane potentials around an extracellular electrode: dependence on fiber orientation." *Biophys J*, vol. 68, no. 6, pp. 2310-2322, 1995.

[3] Wikswo, J. P., Jr., Lin, S.-F., and Abbas, R. A., "Virtual electrodes in cardiac tissue: A common mechanism for anodal and cathodal stimulation." *Biophys J*, vol. 69, no. 6, pp. 2195-2210, 1995.

[4] Sepulveda, N. G. and Wikswo, J. P., Jr., "Electric and magnetic fields from two-dimensional anisotropic bisyncytia." *Biophys J*, vol. 51, no. 4, pp. 557-568, 1987.

[5] Sepulveda, N. G., Roth, B. J., and Wikswo, J. P., Jr., "Current injection into a two-dimensional anisotropic bidomain." *Biophys J*, vol. 55 pp. 987-999, 1989.

[6] Wikswo, J. P., Jr., "The complexities of cardiac cables: virtual electrode effects." *Biophys J*, vol. 66, no. 3 Pt 1, pp. 551-553, 1994.

[7] Roth, B. J., "A mathematical model of make and break electrical stimulation of cardiac tissue by a unipolar anode or cathode." *IEEE Trans Biomed Eng*, vol. 42, no. 12, pp. 1174-1184, 1995.

[8] Roth, B. J., "Strength-interval curves for cardiac tissue predicted using the bidomain model." *J Cardiovasc Electrophysiol*, vol. 7, no. 8, pp. 722-737, 1996.

[9] Lin, S.-F., Roth, B. J., and Wikswo, J. P., Jr., "Quatrefoil reentry in myocardium: An optical imaging study of the induction mechanism." *J Cardiovasc Electrophysiol*, vol. 10, no. 4, pp. 574-586, 1999.

[10] Gettes, L. S., "The electrophysiology of acute ischemia." in Fisch, C. and Surawicz, B. (eds.) *Cardiac electrophysiolgy and arrhythmias.* New York: Elsevier, 1991, pp. 13-24.

[11] Surawicz, B., "The interrelationship of electrolyte abnormalities and arrhythmias." in Mandel, W. J. (ed.) *Cardiac arrhythmias: Their mechanisms, diagnosis, and management.* Philadelphia: J.B. Lippincoff Company, 1995, pp. 89-109.

[12] Beeler, G. W. and Reuter, H., "Reconstruction of the action potential of ventricular myocardial fibres." *J Physiol (Lond)*, vol. 268, no. 1, pp. 177-210, 1977.

[13] Pertsov, A., Vinson, M., and Muller, S. C., "Three-dimensional reconstruction of organizing centers in excitable chemical media." *Physica D*, vol. 63, no. 1-2, pp. 233-240, 1993.

[14] Gray, R. A., Jalife, J., Panfilov, A., Baxter, W. T., Cabo, C., Davidenko, J. M., and Pertsov, A. M., "Nonstationary vortexlike reentrant activity as a mechanism of polymorphic ventricular tachycardia in the isolated rabbit heart." *Circulation*, vol. 91, no. 9, pp. 2454-2469, 1995.

[15] Berenfeld, O., Zaitsev, A. V., Mironov, S. F., Pertsov, A. M., and Jalife, J., "Frequency-dependent breakdown of wave propagation into fibrillatory conduction across the pectinate muscle network in the isolated sheep right atrium." *Circ Res*, vol. 90, no. 11, pp. 1173-1180, 2002.

[16] Boersma, L., Brugada, J., Kirchhof, C. J., and Allessie, M. A., "The effects of potassium on anisotropic conduction." in Sideman, S., Beyar, R., and Kleber, A. G. (eds.) *Cardiac Electrophysiology, Circulation, and Transport* Boston, MA: Kluwer Academic Publishers, 1991, pp. 101-108.

[17] Dekker, E., "Direct current make and break thresholds for pacemaker electrodes on the canine ventricle." *Circ Res*, vol. 27, no. 5, pp. 811-823, 1970.

[18] Nikolski, V. P., Sambelashvili, A. T., and Efimov, I. R., "Mechanisms of make and break excitation revisited: paradoxical break excitation during diastolic stimulation." *Am J Physiol Heart Circ Physiol*, vol. 282, no. 2, pp. H565-H575, 2002.

[19] Katz, A. M., "The cardiac action potential." *Physiology of the Heart.* 2nd ed. New York: Raven Press, 1992, pp. 438-473.

[20] Whalley, D. W., Wendt, D. J., Starmer, C. F., Rudy, Y., and Grant, A. O., "Voltage-independent effects of extracellular K+ on the Na+ current and phase 0 of the action potential in isolated cardiac myocytes." *Circ Res*, vol. 75, no. 3, pp. 491-502, 1994.

[21] Nygren, A. and Giles, W. R., "Mathematical simulation of slowing of cardiac conduction velocity by elevated extracellular [K^+] in a human atrial strand." *Ann Biomed Eng*, vol. 28, no. 8, pp. 951-957, 2000.

[22] Girouard, S. D., Laurita, K. R., and Rosenbaum, D. S., "Unique properties of cardiac action potentials recorded with voltage-sensitive dyes." *J Cardiovasc Electrophysiol*, vol. 7, no. 11, pp. 1024-1038, 1996.

[23] Cheng, Y., Mowrey, K. A., Nikolski, V., Tchou, P. J., and Efimov, I. R., "Mechanisms of shock-induced arrhythmogenesis during acute global ischemia." *Am J Physiol Heart Circ Physiol*, vol. 282, no. 6, pp. H2141-H2151, 2002.

[24] Gettes, L. and Surawicz, B., "Effects of low and high concentrations of potassium on the simultaneously recorded Purkinje and ventricular action potentials of the perfused pig moderator band." *Circ Res*, vol. 23, no. 6, pp. 717-729, 1968.

[25] Streeter, D. D., Spotnitz, H. M., Patel, D. P., Ross, J., Jr., and Sonnenblick, E. H., "Fiber orientation in the canine left ventricle during diastole and systole." *Circ Res*, vol. 24, no. 3, pp. 339-347, 1969.

[26] Streeter, D. D., "Gross morphology and fiber geometry of the heart." in Berne, R. M., Sperelakis, N., and Geiger, S. R. (eds.) *Handbook of Physiology* Bethesda, MD: American Physiological Society, 1979, pp. 61-112.

[27] Efimov, I. R., Sidorov, V., Cheng, Y., and Wollenzier, B., "Evidence of three-dimensional scroll waves with ribbon-shaped filament as a mechanism of ventricular tachycardia in the isolated rabbit heart." *J Cardiovasc Electrophysiol*, vol. 10, no. 11, pp. 1452-1462, 1999.

[28] Al-Khadra, A., Nikolski, V., and Efimov, I. R., "The role of electroporation in defibrillation." *Circ Res*, vol. 87, no. 9, pp. 797-804, 2000.

[29] Baxter, W. T., Mironov, S. F., Zaitsev, A. V., Jalife, J., and Pertsov, A. M., "Visualizing excitation waves inside cardiac muscle using transillumination." *Biophys J*, vol. 80, no. 1, pp. 516-530, 2001.

[30] Ding, L., Splinter, R., and Knisley, S. B., "Quantifying spatial localization of optical mapping using Monte Carlo simulations." *IEEE Trans Biomed Eng*, vol. 48, no. 10, pp. 1098-1107, 2001.

[31] Skouibine, K. B., Trayanova, N. A., and Moore, P. K., "Anode/cathode make and break phenomena in a model of defibrillation." *IEEE Trans Biomed Eng*, vol. 46, no. 7, pp. 769-777, 1999.

[32] Allessie, M. A., Schalij, M. J., Kirchhof, C. J., Boersma, L., Huybers, M., and Hollen, J., "Experimental electrophysiology and arrhythmogenicity. Anisotropy and ventricular tachycardia." *Eur Heart J*, vol. 10 Suppl E pp. 2-8, 1989.

[33] Brugada, J., Boersma, L., Kirchhof, C. J., Brugada, P., Havenith, M., Wellens, H. J., and Allessie, M., "Double-wave reentry as a mechanism of acceleration of ventricular tachycardia." *Circulation*, vol. 81, no. 5, pp. 1633-1643, 1990.

[34] Brugada, J., Boersma, L., Kirchhof, C. J., Heynen, V. V., and Allessie, M. A., "Reentrant excitation around a fixed obstacle in uniform anisotropic ventricular myocardium." *Circulation*, vol. 84, no. 3, pp. 1296-1306, 1991.

[35] Schalij, M. J., Lammers, W. J., Rensma, P. L., and Allessie, M. A., "Anisotropic conduction and reentry in perfused epicardium of rabbit left ventricle." *Am J Physiol*, vol. 263, no. 5 Pt 2, pp. H1466-H1478, 1992.

[36] Knisley, S. B. and Hill, B. C., "Effects of bipolar point and line stimulation in anisotropic rabbit epicardium: assessment of the critical radius of curvature for longitudinal block." *IEEE Trans Biomed Eng*, vol. 42, no. 10, pp. 957-966, 1995.

[37] Girouard, S. D., Pastore, J. M., Laurita, K. R., Gregory, K. W., and Rosenbaum, D. S., "Optical mapping in a new guinea pig model of ventricular tachycardia reveals mechanisms for multiple wavelengths in a single reentrant circuit." *Circulation*, vol. 93, no. 3, pp. 603-613, Feb.1996.

[38] Liu, Y., Cabo, C., Salomonsz, R., Delmar, M., Davidenko, J., and Jalife, J., "Effects of diacetyl monoxime on the electrical properties of sheep and guinea pig ventricular muscle." *Cardiovasc Res*, vol. 27, no. 11, pp. 1991-1997, 1993.

[39] Li, T., Sperelakis, N., Teneick, R. E., and Solaro, R. J., "Effects of diacetyl monoxime on cardiac excitation-contraction coupling." *J Pharmacol Exp Ther*, vol. 232, no. 3, pp. 688-695, 1985.

CHAPTER IV

SPATIO-TEMPORAL DYNAMICS OF DAMPED PROPAGATION IN EXCITABLE CARDIAC TISSUE

Veniamin Y. Sidorov[1], Rubin R. Aliev[1], Marcella C. Woods[2],

Franz Baudenbacher[1], Petra Baudenbacher[1], John P. Wikswo[1,2,3]

Departments of [1]Physics & Astronomy, [2]Biomedical Engineering, and

[3]Molecular Physiology & Biophysics

Vanderbilt University, Nashville, Tennessee

Portions of this manuscript have been published in:

VY Sidorov, RR Aliev, MC Woods, F Baudenbacher, P Baudenbacher, JP Wikswo. *Physical Review Letters*, Vol. 91, No. 20, pp. 208140-1─208140-4, 2003.

4.1. Abstract

Compared to steadily propagating waves (SPW), damped waves (DW), another solution to the non-linear wave equation, are seldom studied. In cardiac tissue after electrical stimulation in an SPW wake, we observe DW with diminished amplitude and velocity that either gradually decrease as the DW dies, or exhibit a sharp amplitude increase after a delay to become an SPW. The cardiac DW-SPW transition is a key link in understanding defibrillation and stimulation close to the refractory period, and is ideal for general study of DW dynamics.

4.2. Introduction

The physics of the propagation of continuous waves in passive (linear) media has been studied exhaustively and exhibit reflection, refraction, and interference. In the classic example of electromagnetic (EM) waves in vacuum, waves of all frequencies propagate with the same phase velocity, so that a solitary EM pulse can propagate without distortion and can pass through another pulse unchanged. In lossy media, where energy is dissipated, wave amplitude decays as it propagates. In dispersive media, where wavelength depends upon propagation velocity, the wave shape can change with time and anomalous dispersion can occur.

In active (non-linear) media, for which losses in the media are accompanied by the release of stored energy, solitary waves of a particular shape can propagate without distortion. The wave shape is determined by the governing non-linear differential equations. Propagating nerve and cardiac action potentials (APs) are examples of solitary waves for which nonlinearities determine biologically important phenomena [1]: AP initiation requires a suprathreshold electrical stimulus, which in turn depends upon both

the stimulus duration and the elapsed time since the previous AP. A minimum time interval, termed the absolute refractory period (ARP), must separate the leading edges of sequential APs, regardless of stimulus strength. Because of the ARP, upon collision APs will annihilate each other. Despite the common assumption that the AP has a constant shape and a uniform conduction velocity, experiments reveal that an AP following immediately after another AP will have a deformed shape (termed restitution) and reduced propagation velocity (termed dispersion) as compared to one after a longer separation in time [2]. Most of these phenomena are evident, for example, in reentrant cardiac arrhythmias [3]. Reduction of the threshold can increase the sensitivity to extraneous electrical activity and can lead to the spontaneous generation of waves that form expanding target patterns. AP annihilation upon collision results in a volume of tissue being refractory, so that any conduction through that region is blocked for a time longer than the ARP. Conduction block can lead to an AP that propagates over a closed path to form a vortex or more complex reentrant patterns [4]. A reduction in the ARP can lead to higher reentry frequencies, as seen in fibrillation, the most dangerous of all cardiac reentries. Finally, there is an ongoing controversy as to whether reexcitation following an unsuccessful defibrillation shock arises from an unstable point focus (triggered activity), an intramural reentry not visible from the epicardium, or slow propagation in the electrically altered post-shock tissue [5,6].

In this paper, we demonstrate experimentally that non-uniform propagation and AP amplitude decay can play an important role in both conduction block and delayed activation. We used isolated rabbit hearts and applied a conditioning electrical stimulus (S_1), which produced a solitary AP propagating with constant shape and amplitude.

Following a specified interval, we applied a second stimulus (S_2), which launches another wave into the wake of the initial one. This protocol is of special interest to the study of the vulnerability of the heart to the initiation of self-maintained, high frequency wave sources that have long been regarded as a precursor to dangerous cardiac arrhythmias [7-9]. A widely accepted mathematical description of vulnerability assumes that the effect of stimulation depends on the S_2 timing: an S_2 soon after S_1 dies out, because it is applied to absolutely refractory tissue; an S_2 long after S_1 freely propagates, because it is applied to resting tissue; an S_2 applied close to the boundary of absolute refractoriness may result in a discontinuous front that evolves into reentry (see ref. [9] for details). This description bears its roots in the simple cellular automata model by Wiener and Rosenblueth [8], which assumes only discrete states of the medium occur, *i.e.,* a wave either has a constant shape and propagates steadily, or it disappears. However, as mentioned above, theoretical and experimental observations indicate that the shape, amplitude, and velocity of a propagating wave are not always constant. Our experiments were designed to test quantitatively in cardiac tissue theoretical predictions regarding the spatio-temporal effects of S_2 stimulation in the wake of the previous conditioning wave, particularly those by Aliev and Panfilov in the Belousov-Zhabotinsky reaction [10].

4.3. Experimental Procedures

We used cryoablation to obtain a 1 mm thick, quasi-2D layer of left ventricular epicardium [11] from 2 – 3 kg New Zealand white rabbits (n = 10). We visualized the distribution of the transmembrane potential using a standard fluorescence mapping system, and voltage-calibrated the fluorescence images with microelectrode measurements [12]. We used the important pinwheel stimulation protocol [13]: To

initiate planar conditioning S_1 waves propagating across the left ventricle, we placed a linear wire electrode, oriented perpendicular to the fibers, on the lower part of the left ventricular wall, and paced the heart at a cycle length of 300 ms. S_2 was applied with a point electrode approximately at the center of the imaging area. The current used for S_1 pacing was just above the threshold, whereas the current for the S_2 was 2 mA (about 20× diastolic threshold). The stimulus duration was 2 ms for S_1 and 10 ms for S_2 pulses. During each experiment, the S_1–S_2 interval was progressively shortened in 5 - 10 ms steps starting from 250 ms down to the ARP, when S_2 no longer produced a propagating wave. The slow-wave dynamics described below were observed in all ten hearts when S_2 was applied near the refractory tail of the S_1 response.

4.4. Results

The results displayed in Figure 4.1 and Figure 4.2 depict the analysis for one typical recording using an S_1–S_2 interval of 180 ms and a 2 mA cathodal S_2. Figure 4.1 demonstrates the dynamics observed after application of S_2 close to the refractory period. The frames of the false color voltage movie in Figure 4.1(a) show the response of the heart following S_2 termination. The movie starts at the end of S_2, which was applied when the preceding S_1 wave produced a gradient of repolarization in the vicinity of the S_2 electrode location. The S_1-induced planar wave had already propagated along the fiber direction from the lower-right to the upper-left of the image area, with the tail of the S_1 steadily propagating wave (SPW) disappearing in the upper left corner of the 0 and 8 ms frames. As a result of S_2, two low amplitude waves appear to propagate in opposite directions (arrows in the 16 ms frame). The wave moving left and upward dies out by 28 ms, while the wave propagating right and downward becomes a full amplitude response,

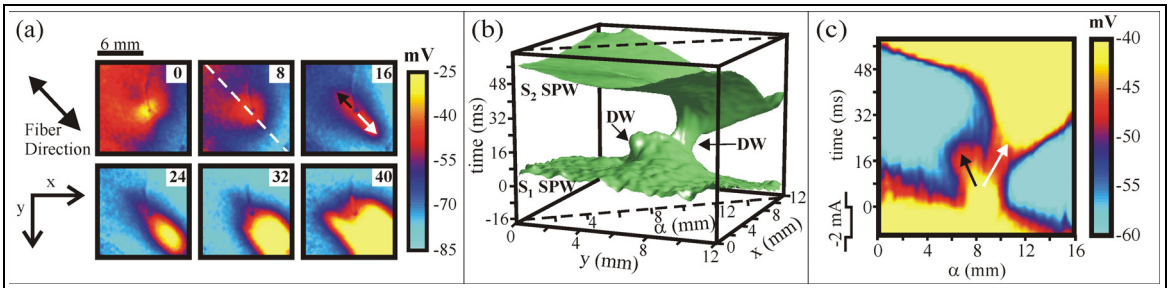

Figure 4.1. Damped propagation resulting from S_2 stimulation in the wake of a conditioning S_1 wave using a cathodal 2 mA, 10 ms S_2 (S_1-S_2 interval of 180 ms). (a) Frames of a movie of the transmembrane potential distribution, $V_m(x,y)$. The S_2 point electrode is located at the center of the images. The numbers in the upper right represent the time (ms) since S_2 termination. The arrows at 16 ms indicate DW propagation. (b) A 3-D presentation of $V_m(x,y,t)$ following S_2 stimulation, constructed by stacking sequentially recorded 2-D plots of $V_m(x,y)$, applying spatio-temporal filtering, and selecting V_m = -50 mV as the threshold to show the repolarization phase of the S_1 SPW and the post-S_2 activation dynamics. The dashed α-axis is parallel to the fiber direction and corresponds to the white dashed line in the 8 ms image in panel (*a*). (c) The DW and S_2 SPW spatio-temporal dynamics. The time-space plot $V_m(\alpha,t)$ was constructed along the α-axis. Black and white arrows indicate the propagation direction for the two DW. In all panels, S_2 ended at *Time* = 0.

which starts to propagate in all directions (last frame). A time lag of approximately 40 ms exists between the termination of S_2 and the appearance of the full amplitude response.

Figure 4.1(b) shows two damped waves (DW) forming following S_2 stimulation, which was applied to the refractory tail of the SPW from S_1, but only one DW causes a fully propagating wave front (S_2 SPW). More detailed spatio-temporal characteristics of the dynamics are illustrated in the time-space plot of Figure 4.1(c), for which the data movie was sliced along the dashed α-axis in panel (b). From this plot, one clearly sees that the left wave dies, while the wave on the right results in a full amplitude response.

Figure 4.2(a) and (b) show the DW dynamics in terms of signal upstroke (dV_m/dt). Figure 4.2 (a) elucidates the wave front dynamics following S_2 stimulation (S_1 activity has been removed from the plot). The two waves propagate in opposite directions (white and black arrows) from the dog-bone shaped polarization [14] located at the center of the (x,y) plane. One of the waves decays, and the other transforms into a wave similar to the S_1-induced, high-amplitude SPW. Figure 4.2 (b) demonstrates dV_m/dt amplitude for the

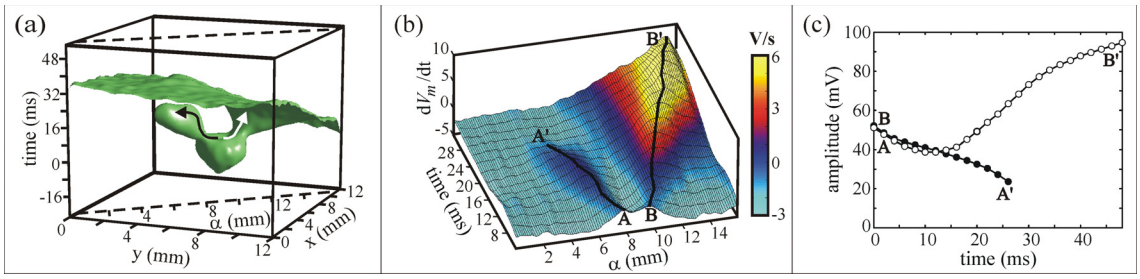

Figure 4.2. Detailed analysis of damped wave propagation. (a) 3-D presentation of signal upstroke ($dV_m(x,y,t)/dt$) following S_2 stimulation, constructed by stacking sequential 2-D plots of $dV_m(x,y,t)/dt$, applying spatio-temporal filtering, and selecting dV_m/dt = -1.1 V/s as the threshold. The arrows indicate the DW with decaying propagation (black) and the growing wave (white). (b) $dV_m(\alpha,t)/dt$ as a function of time and space along the α-axis. A-A' and B-B' are the two S_2 DW: A-A' decays and dies, while B-B' eventually grows into an SPW. (c) The amplitude of waves A-A' (filled) and B-B' (open) from (*b*). S_2 terminated at *Time* = 0.

two waves as a function of time along the dashed α-axis in (a). The decaying wave, A-A', exhibits very small dV_m/dt until it finally dies, while for the other wave, B-B', dV_m/dt eventually increases. The crest-position of the waves reflects the dynamics of the propagation velocity: A-A' has slower velocity (16.1 ± 0.5 cm/s) which approaches zero around 25 ms after S_2 termination, while B-B' exhibits a higher, fairly stable velocity for the interval shown (21.4 ± 0.4 cm/s). The two types of DW dynamics are clearly seen in Figure 4.2 (c). For A-A' the amplitude of the wave decreases with time until it disappears almost 25 ms after S_2 cessation (filled circles). B-B' (open circles) initially has similar dynamics, but instead of disappearing, eventually gains amplitude to produce a full-scale SPW.

The distance of low-amplitude DW propagation and the time delay between S_2 application and the transition of the DW into an SPW depends on the S_1–S_2 interval. Figure 4.3 illustrates the DW propagation distance and S_2-SPW delay as a function of S_1–S_2 interval. The data presented in this figure were acquired from a different heart than the data shown in Figure 4.1and Figure 4.2. Two phases are distinguishable in this curve: as the S1-S2 interval is decreased toward refractoriness, the character of the curve changes

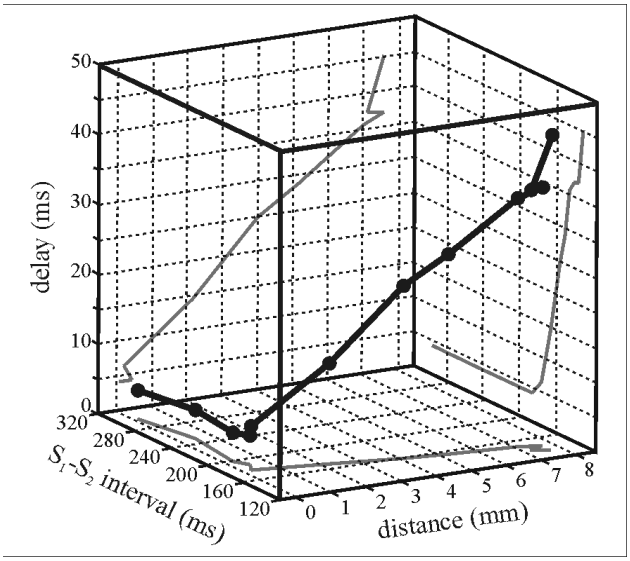

Figure 4.3. Delay between S_2 and SPW appearance versus distance between electrode position and location of SPW origination as a function of S_1-S_2 interval. The threshold of 95 mV amplitude was used to locate the earliest conversion of DW to SPW. The delay was calculated as the period between S_2 onset and full amplitude response activation time $((dV_m/dt)_{max})$. Projections of the curve onto the three axes are in gray. The sharp change in the curve corresponds to the transition of the stimulation mechanism from make to break.

dramatically, with the distance and delay rising dramatically below 180 ms. This sharp change is caused by the transition of the stimulation mechanism from make to break [12,14]. In addition, the X-Z projection demonstrates approximately linear distance-delay dependence for S_1–S_2 intervals between 180 and 150 ms, indicating only slight influence of S_1–S_2 interval shortening on DW velocity (18.2 ± 2 cm/s). The minimal S_1–S_2 interval for response was 135 ms.

4.5. Discussion

The "S_1-S_2" stimulation protocol has been widely used to study the cardiac response to premature stimulation. The dynamics are of special interest when the S_1-S_2 interval is close to the refractory period. We show damped propagating waves that either died out or evolved into a full-scale SPW. These dynamics are unusual from the point of

view of classical theory [9] and, in our opinion, have received too little attention in either the theoretical or experimental literature.

Previously, the appearance of DW, sometimes referred to as decaying propagation, has been shown near the vulnerable window boundaries in both FitzHugh-Nagumo and Beeler-Reuter models of excitable media [9,15,16]. In a simulated nerve fiber using the 1-D FitzHugh-Nagumo model under temperature gradient conditions, a slow-velocity, unstable wave and a fast-velocity, stable wave originating from the same point and traveling in opposite directions have also been demonstrated [17]. Recent findings show that multiple responses exist after a single stimulation near the boundary of vulnerable window, and are the result of propagation and conversion of DW into normal pulses [10]. Similar patterns were observed in a theoretical study of an inhomogeneous medium [18], where the patterns occurred near the boundary of an inhomogeneity. An interesting insight to the problem was recently suggested by Biktashev [19], who reformulated the classical Hodgkin-Huxley approach to excitable systems to include two equations describing the front of the pulse. He found that under proper conditions, propagation loses stability and becomes dissipative.

In experimental cardiac studies, responses different than all-or-none activity were initially reported by Kao and Hoffman [20]. They used isolated papillary muscles and Purkinje fibers to produce graded and decremental responses by varying the S_2 strength applied at a fixed time during repolarization or by varying the S_1-S_2 interval using a fixed S_2 strength. Additionally, the differences between the experimental study by Jalife and Moe, examining the role of passive tissue properties in conduction delay and impulse reflection [21], and the present work, describing an active response to stimulation in the

repolarization phase, should be emphasized. They used an isotonic sucrose solution as an isolator to produce an unexcitable gap between the proximal and distal sections of a Purkinje strand preparation, such that the transmission of the excitation between the two excitable segments is accomplished electrotonically by a passive response, in contrast to the active mechanism in our DW study.

It is important to note that, until now, DW dynamics have been experimentally studied only for chemical media in the Belousov-Zhabotinsky reaction [10]. Cardiac research has begun to address this subject in terms of a "graded response" [22]. Gotoh *et al.* [23] used a stimulation protocol similar to ours to investigate the induction of reentry, and observed that a propagating lower-amplitude response could initiate normal activation distantly from the S_2 site. Although we suggest that the DW dynamics described in this present work may underlie the graded response effect, some important differences should be emphasized. Specifically, in contrast with this DW study in which S_2 monopolar cathodal pulses were applied in the wake of planar S_1 SPW, Gotoh *et al.* used bipolar electrodes for S_1 and S_2 stimulation, with the cathodal S_2 pole located nearer the S_1 and the S_2 poles oriented along the fiber direction. It has been shown that bipolar stimulation produces complex polarization patterns, which depends on both interelectrode distance and the position of the stimulating dipole with respect to the fiber direction [24]. Hence, the tissue response is determined not only by stimulus parameters but also by bipolar electrode location. Another important difference is the S_2 stimulus strength, in that Gotoh *et al.* studied vulnerability to reentry and hence examined high amplitude stimulation. On the contrary, we used low intensity S_2 pulses to produce DW that could propagate over the polarization area.

Our work along with theoretical findings show that either functional inhomogeneity, which exists in the refractory tail [10], or an anatomical inhomogeneity [18] can result in damped propagation and, hence, demand a substantial revision of the classical explanation of vulnerability of cardiac tissue. Damped propagation must be examined in the context of apparent focal activity after a defibrillation shock [5]. We also conclude that cardiac tissue can serve as an ideal excitable medium to refine the measurement and understanding of the physics of damped propagation of waves in non-linear, active media, particularly for reentrant, vortex-like excitation.

4.6. Acknowledgements

This work was supported by the NIH (R01-HL58241), the AHA (0215128B), gifts from William McMinn, and the Academic Venture Capital Fund of Vanderbilt University.

4.7. References

[1] Scott, A. C., "The nerve fiber." *Neurophysics* New York: John Wiley & Sons, 1977, pp. 90-104.

[2] Cao, J. M., Qu, Z., Kim, Y.-H., Wu, T.-J., Garfinkel, A., Weiss, J. N., Karagueuzian, H. S., and Chen, P.-S., "Spatiotemporal heterogeneity in the induction of ventricular fibrillation by rapid pacing: Importance of cardiac restitution properties." *Circ Res*, vol. 84, no. 11, pp. 1318-1331, 1999.

[3] "Path VIII: Arrhythmia mechanisms." in Zipes, D. P. and Jalife, J. (eds.) *Cardiac Electrophysiology: From Cell to Bedside* 3rd ed. Philadelphia: W. B. Saunders, 2000, pp. 345-422.

[4] Fenton, F. and Karma, A., "Fiber-rotation-induced vortex turbulence in thick myocardium." *Phys Rev Lett*, vol. 81, no. 2, pp. 481-484, 1998.

[5] Chattipakorn, N., Fotuhi, P. C., Chattipakorn, S. C., and Ideker, R. E., "Three-dimensional mapping of earliest activation after near-threshold ventricular defibrillation shocks." *J Cardiovasc Electrophysiol*, vol. 14, no. 1, pp. 65-69, 2003.

[6] Efimov, I. R., Cheng, Y., Van Wagoner, D. R., Mazgalev, T., and Tchou, P. J., "Virtual electrode-induced phase singularity: a basic mechanism of defibrillation failure." *Circ Res*, vol. 82, no. 8, pp. 918-925, 1998.

[7] Wiggers, C. J. and Wegria, R., "Ventricular fibrillation due to single localized induction and condenser shocks applied during the vulnerable phase of ventricular systole." *Am J Physiol*, vol. 128 pp. 500-505, 1940.

[8] Wiener, N. and Rosenblueth, A., "The mathematical formulation of the problem of conduction of impulses in a network of connected excitable elements, specifically in cardiac muscle." *Arch Inst Cardiol Mex*, vol. 16 pp. 205-265, 1946.

[9] Starmer, C. F., Biktashev, V. N., Romashko, D. N., Stepanov, M. R., Makarova, O. N., and Krinsky, V. I., "Vulnerability in an excitable medium: analytical and numerical studies of initiating unidirectional propagation." *Biophys J*, vol. 65, no. 5, pp. 1775-1787, 1993.

[10] Aliev, R. R. and Panfilov, A. V., "Multiple responses at the boundaries of the vulnerable window in the Belousov-Zhabotinsky reaction." *Phys Rev E*, vol. 52, no. 3, pp. 2287-2293, 1995.

[11] Allessie, M. A., Schalij, M. J., Kirchhof, C. J., Boersma, L., Huybers, M., and Hollen, J., "Experimental electrophysiology and arrhythmogenicity. Anisotropy and ventricular tachycardia." *Eur Heart J*, vol. 10 Suppl E pp. 2-8, 1989.

[12] Sidorov, V. Y., Woods, M. C., and Wikswo, J. P., "Effects of elevated extracellular potassium on the stimulation mechanism of diastolic cardiac tissue." *Biophys J*, vol. 84, no. 5, pp. 3470-3479, 2003.

[13] Winfree, A. T., *When Time Breaks Down: The Three-Dimensional Dynamics Of Electrochemical Waves And Cardiac Arrhythmias* Princeton: Princeton University Press, 1987, pp. 128-131.

[14] Wikswo, J. P., Jr., Lin, S.-F., and Abbas, R. A., "Virtual electrodes in cardiac tissue: A common mechanism for anodal and cathodal stimulation." *Biophys J*, vol. 69, no. 6, pp. 2195-2210, 1995.

[15] Maginu, K., "Stability of periodic travelling wave solutions of a nerve conduction equation." *J Math Biol*, vol. 6, no. 1, pp. 49-57, 1978.

[16] Maginu, K., "Existence and stability of periodic traveling wave solutions to Nagumo's nerve equation." *J Math Biol*, vol. 10, no. 2, pp. 133-153, 1980.

[17] Fitzhugh, R., "Mathematical models of excitation and propagation in nerve." in H.P.Schwan (ed.) *Biological Engineering* New York: McGraw-Hill, 1969, pp. 1-85.

[18] Ermentrout, G. B. and Rinzel, J., "Reflected waves in an inhomogeneous excitable medium." *SIAM J Appl Math*, vol. 56, no. 4, pp. 1107-1128, 1996.

[19] Biktashev, V. N., "Dissipation of the excitation wave fronts." *Phys Rev Lett*, vol. 89, no. 16, pp. 168102, 2002.

[20] Kao, C. Y. and Hoffman, B. F., "Graded and decremental responses in heart muscle fibers." *Am J Physiol*, vol. 194, no. 1, pp. 187-196, 1958.

[21] Jalife, J. and Moe, G. K., "Excitation, conduction, and reflection of impulses in isolated bovine and serum cardiac purkinje fibers." *Circ Res*, vol. 49, no. 1, pp. 233-247, 1981.

[22] Trayanova, N. A., Gray, R. A., Bourn, D. W., and Eason, J. C., "Virtual electrode-induced positive and negative graded responses: New insights into fibrillation induction and defibrillation." *J Cardiovasc Electrophysiol*, vol. 14, no. 7, pp. 756-763, July2003.

[23] Gotoh, M., Uchida, T., Mandel, W. J., Fishbein, M. C., Chen, P.-S., and Karagueuzian, H. S., "Cellular graded responses and ventricular vulnerability to reentry by a premature stimulus in isolated canine ventricle." *Circulation*, vol. 95, no. 8, pp. 2141-2154, 1997.

[24] Sepulveda, N. G. and Wikswo, J. P., Jr., "Bipolar stimulation of cardiac tissue using an anisotropic bidomain model." *J Cardiovasc Electrophysiol*, vol. 5, no. 3, pp. 258-267, 1994.

CHAPTER V

EXAMINATION OF THE STIMULATION MECHANISM AND STRENGTH-INTERVAL CURVE IN CARDIAC TISSUE

Veniamin Y. Sidorov[1,2], Marcella C. Woods[1],

Petra Baudenbacher[2], Franz Baudenbacher[1,2]

[1]Department of Biomedical Engineering and [2]Department of Physics and Astronomy

Vanderbilt University, Nashville, Tennessee

Portions of this manuscript have been published in:

VY Sidorov, MC Woods, P Baudenbacher, F Baudenbacher.
American Journal of Physiology – Heart and Circulatory Physiology,
Vol. 289, No. 6, pp. H2602-H2615, 2005.

5.1. Abstract

Understanding the basic mechanisms of excitability through the cardiac cycle is critical to both the development of new implantable cardiac stimulators and improvement of the pacing protocol. Although numerous works have examined excitability in different phases of the cardiac cycle, no systematic experimental research has been conducted to elucidate the correlation among the virtual electrode polarization pattern, stimulation mechanism, and excitability under unipolar cathodal and anodal stimulation. We used a high-resolution imaging system to study the spatial and temporal stimulation patterns in 20 Langendorff-perfused rabbit hearts. The potential-sensitive dye di-4-ANEPPS was utilized to record the electrical activity using epi-fluorescence. We delivered S1-S2 unipolar point stimuli with durations of 2-20 ms. The anodal S-I curves displayed a more complex shape in comparison with the cathodal curves. The descent from refractoriness for anodal stimulation was extremely steep, and a local minimum was clearly observed. The subsequent ascending limb had either a dome-shaped maximum or was flattened, appearing as a plateau. The cathodal S-I curves were smoother, closer to a hyperbolic shape. The transition of the stimulation mechanism from break to make always coincided with the final descending phase of both anodal and cathodal S-I curves. The transition is attributed to the bidomain properties of cardiac tissue. The effective refractory period was longer when negative stimuli were delivered than for positive stimulation. Our spatial and temporal analyses of the stimulation patterns near refractoriness show always an excitation mechanism mediated by damped wave propagation after S2 termination.

5.2. Introduction

Earlier studies of excitability during the cardiac cycle demonstrated that recovery of excitability is not a smoothly progressive process, but has an interval of increased excitability or period of superexcitability [1,2]. In the S-I curve this interval appears as a "dip" and, in the family of strength-duration curves, the period of increased excitability is manifested as displacement of the curves under stimulation during the relative refractory period (RRP) [3,4]. Investigations of unipolar cathodal and anodal stimulation of the heart with short pulses revealed that periods of superexcitability are characteristic of positive (anodal) stimulation, whereas the S-I curve for negative (cathodal) stimulation is close to hyperbolic shape [5,6].

Cranefield showed in 1957 that during stimulation by a pair of separated electrodes in diastole, the excitation originates from the site of cathodal stimulation starting with the beginning of the pulse, indicating cathodal make stimulation, but for stimulation in the RRP the excitation occurs at the location of the anode after stimulus termination, indicating anodal break stimulation [5,7]. In 1970, Dekker established the heart's ability to respond to all four modes of direct current activation: anodal make, anodal break, cathodal make, and cathodal break [8]. He also demonstrated the composite nature of the anodal and cathodal S-I curves. He showed that, due to differences in threshold for make and break stimulation, the S-I curve for short stimuli includes the most effective portions of the curves created individually for make and break stimulation.

A theoretical framework for these observations was first established in 1996 using the bidomain model [9,10]. During unipolar myocardial stimulation, both regions of negative and positive polarizations are present. These depolarized and hyperpolarized

regions are called the virtual cathode (VC) and virtual anode (VA), respectively [11-13]. The difference in the ratios of electrical conductivities parallel and perpendicular to the fiber direction in the intracellular and interstitial spaces, also called "unequal anisotropy ratios", cause the formation of virtual electrodes [14,15]. The bidomain model incorporates this feature of cardiac tissue explicitly [10,16-18]. During anodal stimulation, a dog-bone-shaped region of hyperpolarization, oriented transverse to the fiber direction, arises centrally around the stimulating electrode. This hyperpolarized area is flanked by two regions of depolarization in the convex portions of the dog-bone. During cathodal stimulation, the tissue polarization has similar geometry but opposite polarity. In make stimulation, the excitation originates in the depolarized region (VC) at the onset of the stimulus. In break stimulation, the wave front originates in the hyperpolarized area (VA) because of charge diffusion from the VC to the VA area after termination of the stimulus. Bidomain model simulations have demonstrated the importance of virtual electrodes in the complexity of S-I curve shape [9]. Specifically, the dip results from an interaction between the VC and VA areas. The plateau is caused by break stimulation, while the abrupt descent of the plateau phase at the end of the RRP is associated with the change of the stimulation mechanism from break to make.

Although a number of prior studies have explored excitability through the cardiac cycle, this work is the first attempt of a systematic investigation of the role of virtual electrodes in excitability at different S1-S2 coupling intervals. The goal of our study was to investigate experimentally the spatio-temporal effects underlying the mechanism of the S-I relation for unipolar cathodal and anodal stimulation.

5.3. Methods

5.3.1. Experimental Preparation

All experiments followed the guidelines of the National Institutes of Health for the ethical use of animals in research and were approved in advance by the Vanderbilt Institutional Animal Care and Use Committee.

New Zealand White rabbits of either sex weighing 2.2 to 2.5 kg were first preanesthetized with ketamine (50 mg/kg), then heparinized (1000 units), and anesthetized by sodium pentobarbital injection (60 mg/kg) into an ear vein. Following a mid-sternal incision, the heart was removed and placed onto a Langendorff apparatus, where it was retrogradely perfused via the coronary arteries with oxygenated (95% O_2 / 5% CO_2) Tyrode's solution of the following composition (in mM): 133 NaCl, 4 KCl, 2 $CaCl_2$, 1 $MgCl_2$, 1.5 NaH_2PO_4, 20 $NaHCO_3$, and 10 glucose. The excitation-contraction uncoupler 2,3-butanedione monoxime (BDM [Sigma-Aldrich, St. Louis, MO]) was added to the perfusate (15 mM) to eliminate contractile artifacts in the optical recordings. The temperature and pH were continuously maintained at $37^{o} \pm 0.5^{o}$C and 7.4 ± 0.05, respectively. Coronary perfusion pressure was regulated to 50 mm Hg. The hearts were exposed to air during the experiments. A 30-minute stabilization period followed the staining of the heart with 200 μL of di-4-ANEPPS (Molecular Probes, Eugene, OR) stock solution (0.5 mg/mL dimethyl sulfoxide) administered via a bubble trap above the aorta.

5.3.2. Experimental Protocol

In all experiments the anterior left ventricle (LV) was mapped. The heart was continuously paced at a cycle length of 300 ms via a bipolar teflon-coated platinum

electrode (0.125 mm in diameter, 1 mm distance between poles) placed on the right ventricle close to the septum, 8–9 mm from the unipolar testing electrode. The pacing stimulus strength was adjusted to twice the diastolic threshold of excitation. The unipolar testing electrode (delivering S1 and S2), made from platinum wire (0.25-mm diameter), was placed on the center of the anterior LV. The camera field of view was centered with respect to the testing electrode. For S1 stimuli (4 ms duration), the current strength was set slightly above diastolic threshold. A piece of titanium mesh against the posterior LV served as the reference electrode for the S1 and S2 stimuli.

S2 pulses of 20 ms duration for both negative and positive polarities were examined. To test the excitability of the myocardium through the cardiac cycle, the S1-S2 interval was decremented in 20 ms steps beginning at 270 ms. When approaching refractoriness, the testing interval was progressively shortened in 5-10 ms steps until S2 no longer produced a propagating wave in response to currents as large as 10 mA. To measure the threshold current, the S2 pulse was progressively decreased in amplitude in 0.1 mA steps for anodal stimulation and 0.05 mA steps for cathodal stimulation for each examined S1-S2 interval. After the stimulation protocol was completed, the stability of the diastolic threshold was additionally verified. The electrical stimuli in the experiments were provided by computer-controlled current sources (Bloom Associates, Narberth, PA). The light emitting diode (LED) was placed in the right upper corner of the imaged area to indicate the time of S2 application. EGs were continuously monitored using two Ag-AgCl pellet electrodes (EP8, World Precision Instruments) placed on opposite sides of the heart.

5.3.3. Imaging System and Data Acquisition

A high spatial and temporal resolution imaging system was utilized. The main components of the optical system are a Coherent diode-pumped, solid-state Verdi laser (532 nm), bundles of optical fiber for illumination delivery, and a high-speed DALSA 12-bit digital camera with spatial resolution of 128×128 pixels and temporal resolution of 490 frames/second (Model CA D1-0128T, Dalsa, Waterloo, Ontario, Canada). The faceplate of the camera was cooled via a 15^{o}C refrigerated bath. The fluorescence emitted from the imaged area of the heart was collected by a 52-mm lens (+4, Tiffen, Japan) and passed through a cutoff filter (#25 Red, 607 nm, Tiffen, Japan). The magnification was adjusted to focus on a 12×12 mm area.

The camera was connected to a Bitflow R3-DIF image acquisition board (Bitflow, Boston, MA) in a Dell 650 Pentium IV/2 GHz Precision Workstation equipped with 2 GB of random access memory. Custom data acquisition software written in LabVIEW (National Instruments, Austin, TX) records the ~12 MB/s data stream. Following acquisition, data were visualized with a custom MATLAB viewer.

5.3.4. Data Processing and Analysis

Data were first spatially filtered with an 8x8 Gaussian filter and then normalized pixel-by-pixel according to fluorescence changes during the last pacing response. Voltage-calibration was performed according to our previous microelectrode measurements: the resting membrane potential is -85 mV and the action potential (AP) amplitude is 112 mV [19]. To illustrate the net effect of the S2 stimulation on the transmembrane potential distribution (V_m), the previous S1 response was subtracted from the S2 response for some analyses. We refer to this potential distribution as ΔV_m.

To study the development of the cardiac electrical response during stimulation and immediately after termination of the stimulus, time-space plot (TSP) analysis was utilized [19]. TSPs were constructed for lines along and transverse to the fiber direction. The intersection of these two lines roughly coincided with the position of the pacing (S1 and S2) electrode.

To visualize damped propagation after break stimulation three-dimensional stack plots were used. For this purpose data were additionally preprocessed by employing a 5x5 Gaussian spatial filter and a 5-point mean temporal filter; then, two-dimensional plots of dV_m/dt were sequentially stacked yielding the isosurface plot.

The duration of the effective refractory period (ERP) was defined as the minimal S1-S2 interval under which the threshold excitation current exceeded 10 mA. To estimate the relative refractory period (RRP), the maximal S1-S2 interval (T_{max}) for threshold current of 0.1 mA higher than diastolic threshold current was determined. Thereafter RRP was defined as the difference between T_{max} and ERP.

Because excitation of cardiac tissue can originate from either the VC (make stimulation) or from the VA (break stimulation), four spatial locations were examined in the analysis: two points in the central VA and one in each of the adjacent VC regions for anodal stimulation or two points in the central VC and one in each of the flanking VA areas for cathodal stimulation. We refer to these locations as VA1, VA2, VC1, and VC2. While stimulation at threshold intensity does not always yield obvious positive or negative virtual electrode polarizations, for convenience and consistency in analyzing each data set, we will refer to these areas as VC or VA as indicated by the stimulus polarity.

5.3.5. Statistical Analysis

Nine rabbit hearts were used to study cathodal stimulation, and eleven hearts were used for examining anodal stimulation. In addition three experiments were conducted without BDM in the perfusate. Group data are presented as mean values ± std. Statistical analysis was accomplished utilizing the unpaired t-test. Differences were considered significant if $P<0.05$.

5.4. Results

5.4.1. Experimental Cathodal and Anodal Strength-Interval Curves

Figure 5.1 shows the variation of cathodal (Figure 5.1) and anodal (Figure 5.1B) S-I curves from different rabbit hearts. In spite of some variability, common trends inherent in the cathodal and anodal S-I curves are evident. Anodal S-I curves (Figure 5.1B) always contain a dip under stimulation close to the ERP (D), a plateau (P), and then abruptly falloff at the end of the RRP (F). These characteristics are not as evident in the cathodal S-I curves (Figure 5.1A).

For anodal stimulation, the dip was located at an S1-S2 interval of 136.4 ± 13 ms (N = 11) with current magnitude of 1.6 ± 0.7 mA (N = 11). The local maximum for the plateau phase was 2.3 ± 0.8 mA (N = 11) at an S1-S2 interval of 176.4 ± 9.2 ms (N = 11). The subsequent decrease to a constant diastolic threshold was observed at S1-S2 coupling intervals ranging between 178 ± 7.0 ms and 183 ± 7.0 ms (N = 9) for cathodal stimulation and between 185 ± 8.4 ms and 190 ± 8.4 ms (N = 11) for anodal stimulation. The mean values of threshold current in diastolic tissue were 0.15 ± 0.09 mA (N = 9) and 1.05 ± 0.36 mA (N = 11) for cathodal and anodal stimulation, respectively. The experimentally

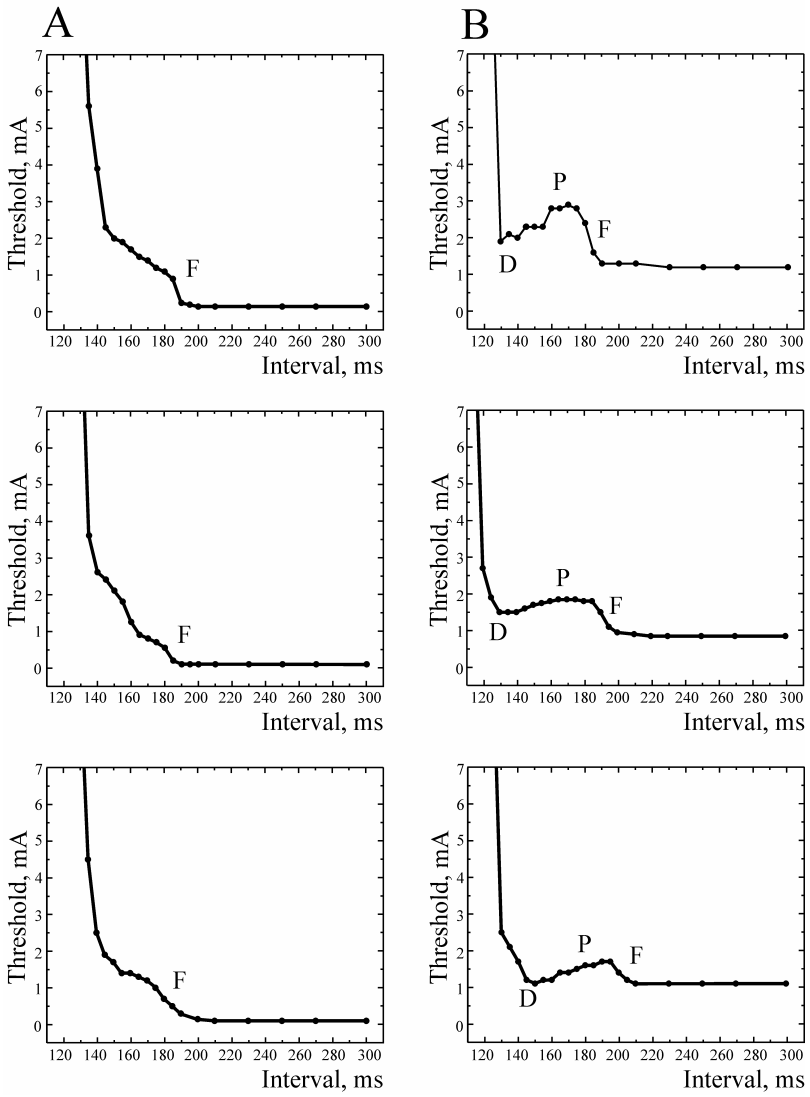

Figure 5.1. Typical cathodal (column A) and anodal (column B) experimental S-I curves illustrating the variability in the measurements among 6 rabbit hearts. The S2 stimulus duration was 20 ms.

measured RRP was longer under anodal stimulation (62.3 ± 12.1 ms; N = 11) than under cathodal stimulation (49.4 ± 5.8 ms; N = 9) ($P<0.01$). However, the duration of the ERP was insignificantly longer for cathodal (134.4 ± 5.8 ms; N = 9) than for anodal testing (129.5 ± 13.3 ms; N = 11).

To determine if BDM affects the S-I curve shape, control experiments without BDM were conducted. Figure 5.2A and B illustrate cathodal and anodal S-I curves for stimulus durations of 20, 10, 5 and 2 ms. The measurements for each polarity were attained in two separate experiments. Figure 5.2C shows the 20-ms cathodal and anodal S-I curves measured in one heart. One can see the shortening of the plateau phase and increase of the ERP as the S2 duration decreases. In addition, the 20-ms S-I curves

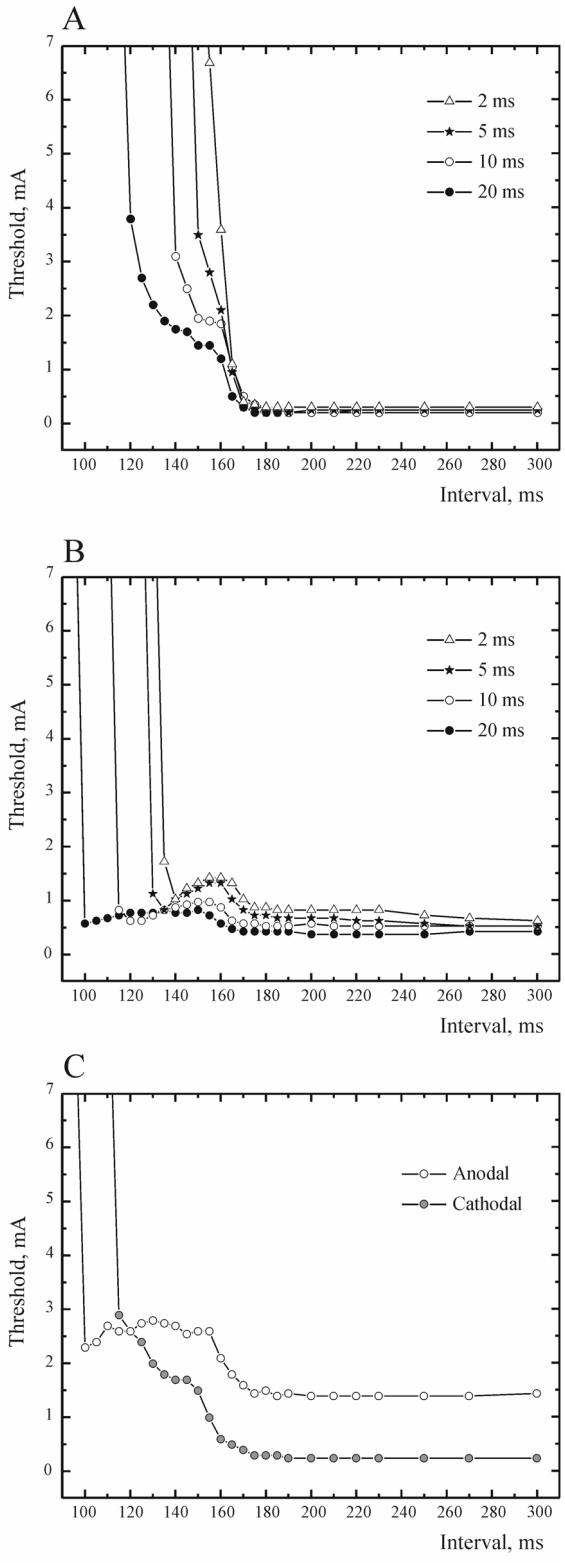

Figure 5.2. Variation of S-I curves as a function of S2 duration obtained without the use of BDM. Cathodal (A) and anodal (B) S-I curves have been constructed with S2 durations of 2 ms, 5 ms, 10 ms and 20 ms. (C) Cathodal and anodal 20-ms S-I curves measured in one heart.

reproduce all of the characteristic phases observed in Figure 5.1 when BDM was used. Because some of these characteristic properties of S-I curves are not apparent for stimuli of shorter durations, the S-I curves constructed for 20-ms pulses were chosen for analysis.

In terms of stimulation mechanism, every curve can be divided into make and break portions (Figure 5.3). The transition between these two segments is illustrated in the following sections.

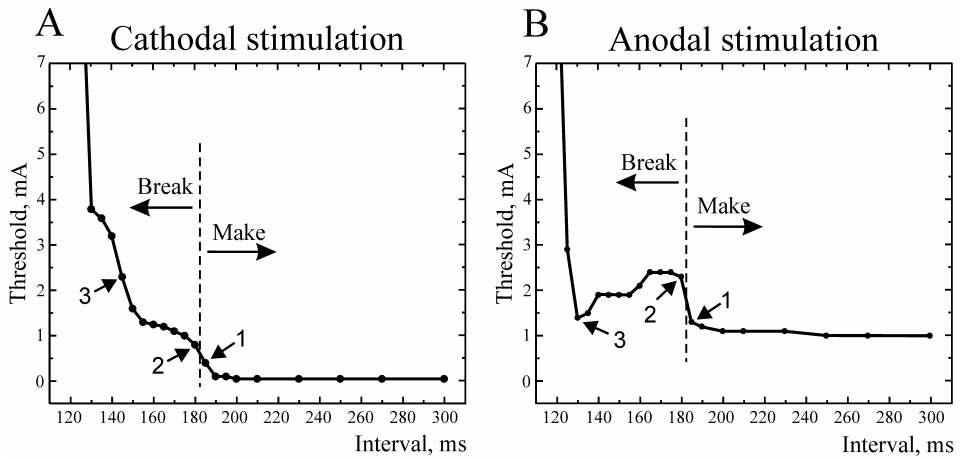

Figure 5.3. Experimental cathodal (A) and anodal (B) S-I curves consisting of two sections: make and break stimulation. The vertical dashed line corresponds to the S1-S2 interval of the transition from the make to break stimulation mechanism. The points of the curves corresponding to the shortest interval for make stimulation and the longest interval for break stimulation are depicted by the numbers "1" and "2", respectively. The number "3" corresponds to the S1-S2 interval close to the ERP when the S2 pulse initiates damped waves. The S2 stimulus duration was 20 ms.

5.4.2. Stimulation at the end of the Relative Refractory Period: transition of the stimulation mechanism from make to break

Cathodal Stimulation. For cathodal stimulation the duration of the RRP was 49.4 ± 5.8 ms (N = 9). Figure 5.4 demonstrates the analysis of the tissue response to

stimulation of –0.4 mA in magnitude with an S1-S2 coupling interval of 185 ms. The corresponding point on the S-I curve in Figure 5.3A is indicated by "1". The images of transmembrane potential (V_m) distribution at 4-ms intervals after the onset of S2 are

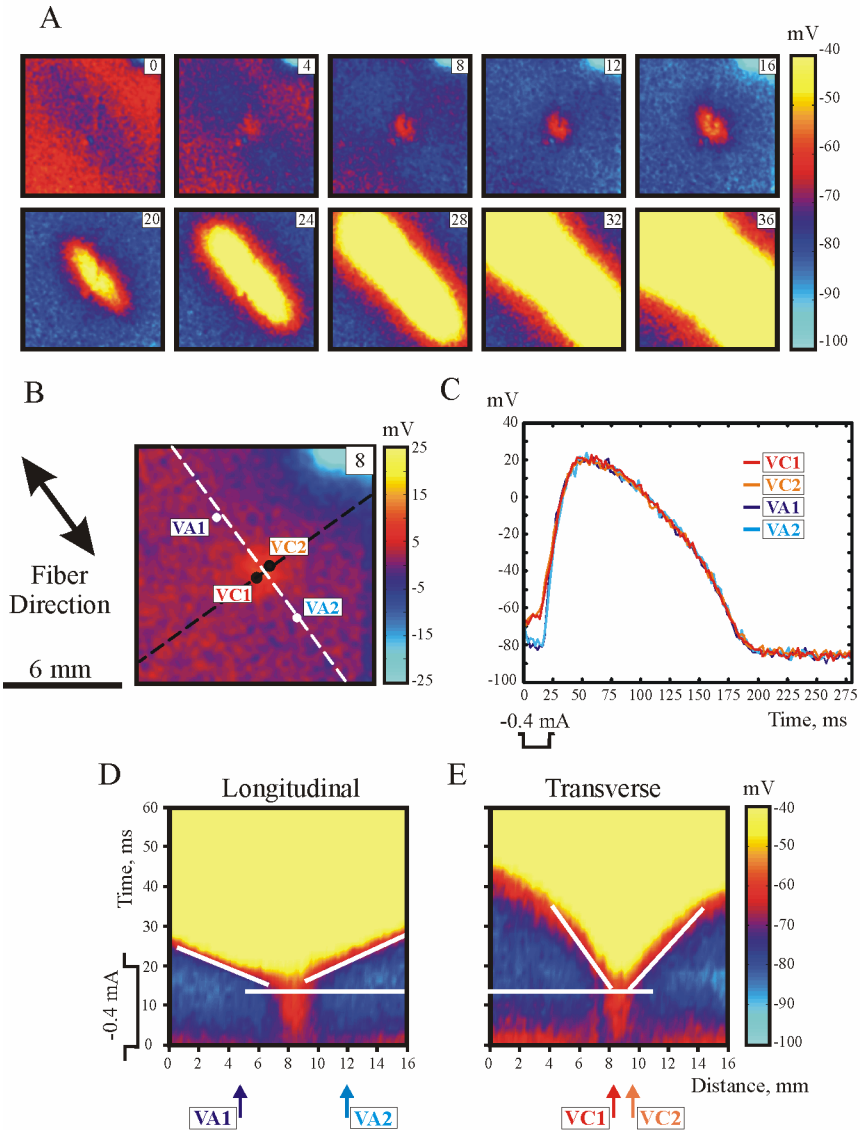

Figure 5.4. Cathodal-make response to threshold stimulation at the end of the RRP using an S1-S2 interval of 185 ms. A: The transmembrane potential distribution as a function of time. The numbers in the upper right represent the elapsed time (ms) since S2 onset. The stimulation electrode is located at the center of the images. The bright blue spot in right upper corner during the first 20 ms is an LED artifact. B: Image of ΔV_m during S2. C: Four traces recorded within the VC (red) and VA (blue) areas. D and E: Time-space plots for lines longitudinal and transverse to the fiber direction (white and black dashed lines in B). The red and blue arrows indicate the location of the pixels depicted by the black and white dots in B. The white horizontal isochronal line corresponds to 13 ms after S2 onset. The white slanted lines in D and E demonstrate propagation velocity along and transverse to the fiber direction, respectively.

presented in Figure 5.4A. Excitation originates in the center of the mapped region, which coincides with the point electrode location and forms the spreading wave of elliptical shape. The image of ΔV_m corresponding to the 8-ms image in Figure 5.4A is shown in Figure 5.4B. Negative polarization in the regions flanking the central VC area is not revealed. In addition, due to stimulation of threshold intensity, the dog-bone contour of the VC is not as evident as for stimulation with larger currents [20]. Four superimposed calibrated optical signals from the VC (red) and VA (blue) regions are demonstrated in Figure 5.4C. The VC APs initiate before S2 termination. The falling of the VA traces during S2 indicates tissue repolarization at these regions. Figure 5.4D and Figure 5.4E illustrate the time-space plots for lines longitudinal and transverse to the fiber direction. These lines are depicted in Figure 5.4B with white and black dashed lines. One can see that activation starts simultaneously at the same location for both longitudinal (Figure 5.4D) and transverse directions (Figure 5.4E). This location corresponds to the VC area. The origination of the excitation at the VC indicates cathodal-make stimulation.

Figure 5.5 illustrates the tissue response to stimulation of –0.8 mA in magnitude. The S1-S2 interval of 180 ms was 5 ms shorter than in the above-described recording. The corresponding position on the S-I curve in Figure 5.3A is indicated by "2". Figure 5.5B illustrates the distribution of ΔV_m at 8 ms after the S2 onset. No prominent VA hyperpolarization is observed. However, after S2 termination (20-ms frame, Figure 5.5A) charge diffusion occurs from the central VC area into the adjacent VA region, which serves as the origin for the later excitation (36-ms frame). In Figure 5.5C the optical signals reveal depolarization in the VC region during S2, while the VA signals exhibit continuation of the recovery from S1. After S2 termination the VC traces reveal negative

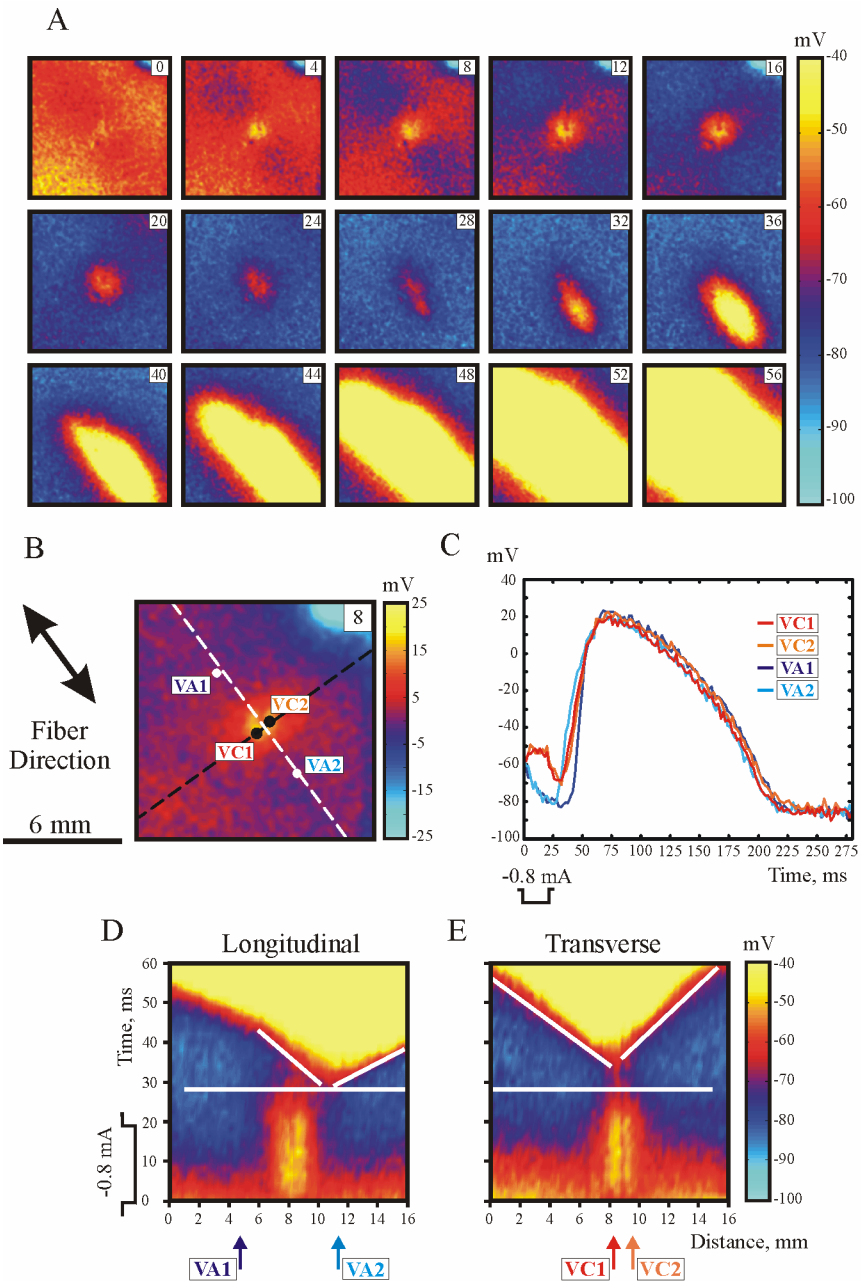

Figure 5.5. Cathodal-break response to threshold stimulation at the end of the RRP. The S1-S2 coupling interval is 180 ms. For the detailed description of the figure parts, refer to the caption for Figure 5.4. In this figure, the white horizontal isochronal line in D and E corresponds to 28 ms after the onset of S2.

polarization whereas the VA2 signal exhibits depolarization. After intersecting with the VC traces, the VA2 trace shows activation prior to the traces from the VC region. Though VC depolarization is very noticeable in Figure 5.5D and E, the time-space plot for the longitudinal direction displays an asymmetric activation pattern suggesting

excitation from the VA2 region. In addition, the horizontal isochronal line indicates activation of the VC area (Figure 5.5E) after VA stimulation (Figure 5.5D) with a delay of 15 ms after S2 termination. The origination of excitation from the VA region after termination of the stimulus indicates cathodal-break as the stimulation mechanism.

The transmembrane potential distribution around the stimulating electrode (1x1 mm^2 area) at the beginning of S2 was –69.8 ± 2.0 mV (121 pixels) for make stimulation and –60.7 ± 2.1 mV (121 pixels) for break stimulation.

Figure 5.6 shows the mean (N = 9) ΔV_m profiles (10 ms after S2 onset) along the fiber direction for both make (Figure 5.6A) and break (Figure 5.6B) cathodal stimulation. The maximal VC depolarization is +16.1 mV and +22.5 mV for make and break stimulation, respectively. No obvious hyperpolarization is detected in the regions flanking the VC.

Anodal Stimulation. The RRP for the anodal stimulation was estimated as 62.3 ± 12.1 ms (N = 11). Analysis of the tissue response to stimulation of +1.3 mA in magnitude with an S1-S2 coupling interval of 185 ms is presented in Figure 5.7. The point on the S-I curve that corresponds to the stimulus under consideration is indicated in Figure 5.3B by "1". Two distinguishable VC depolarizations can be seen during S2 in both the set of consecutive V_m distributions starting with the 12-ms frame (Figure 5.7A) and the image of ΔV_m (Figure 5.7B). The VA hyperpolarization is not visible in Figure 5.7B. At the termination of S2, V_m in the lower right VC achieves threshold and thereafter produces the asymmetric pattern of activation. The time traces in Figure 5.7C demonstrate delay in excitation between the two VC regions. Activation is first observed in the VC2 area

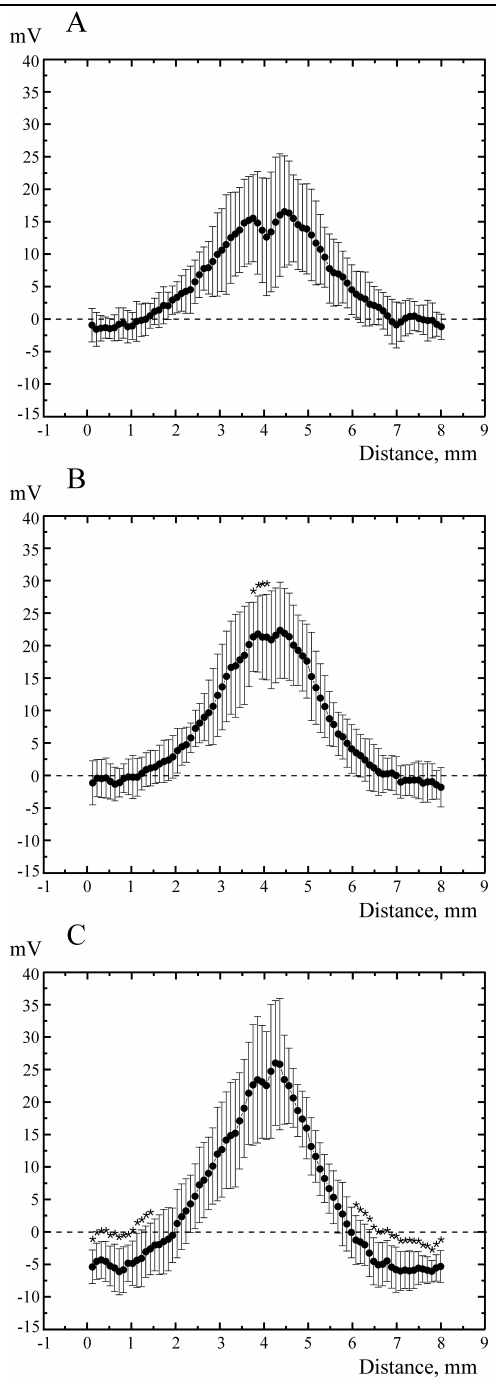

Figure 5.6. ΔV_m profiles during S2 of cathodal make (A), break (B), and DW mediated responses (C). The repolarization of the previous S1 wave was subtracted, and then ΔV_m profiles were extracted for an 8-mm segment along the fiber direction 10 ms after S2 onset. The data is represented as mean ± std, as indicated by the error bars (N = 9). The stimulation site is located at the middle (4 mm) of the segment. Asterisks in B indicate significant difference ($P<0.05$) between the make (A) and break (B) profiles, and those in C indicate significant difference ($P<0.05$) between the break (B) and DW (C) profiles. The S2 strengths were 0.6 ± 0.4 mA for make (A), 1.2 ± 0.7 mA for break (B), and 2.6 ± 0.6 mA for DW (C).

(Figure 5.7B), and then the wave propagates into the VA area (Figure 5.7C blue traces). VC1 activation occurs last. The time-space plots in Figure 5.7D and E show the activation begins in the VC2 area, followed by activation in the VA region. Both the succession of V_m images (Figure 5.7A) and the longitudinal time-space plot (Figure 5.7D) demonstrate asymmetric anodal-make stimulation.

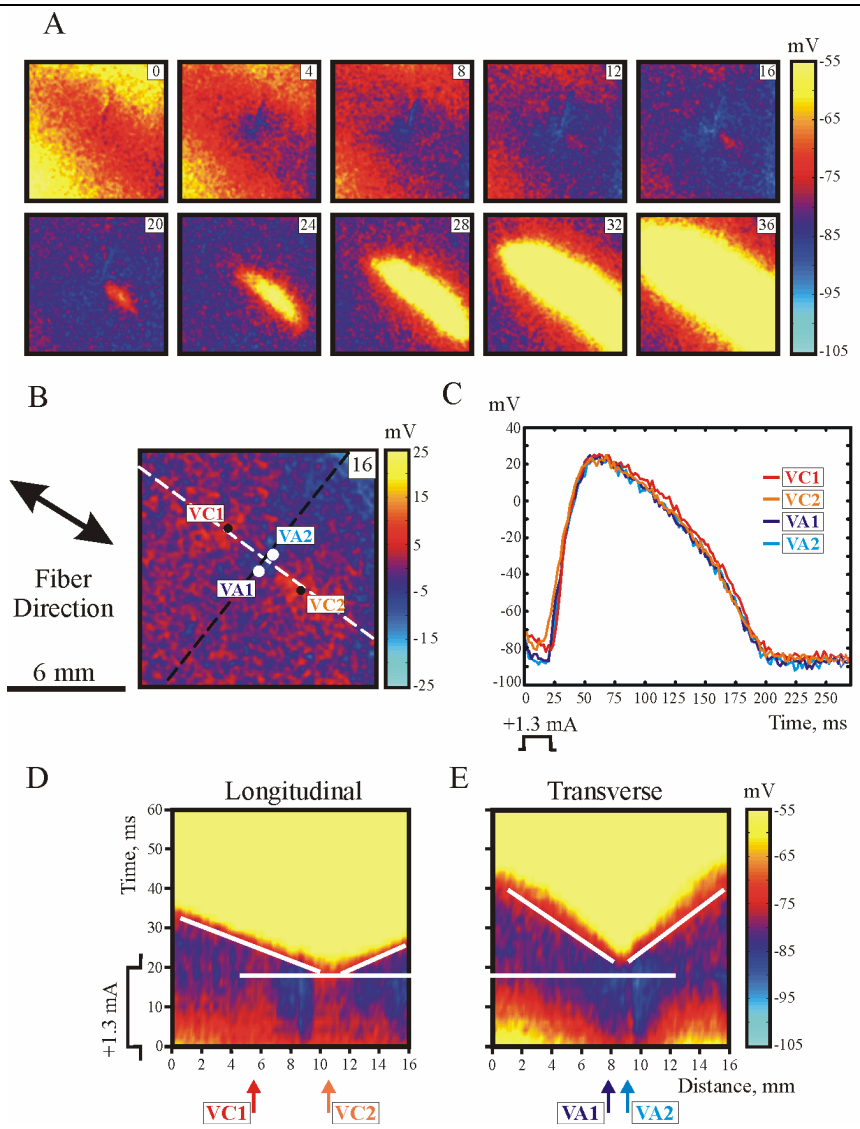

Figure 5.7. Anodal-make response to threshold stimulation at the end of the RRP using an S1-S2 interval of 185 ms. For the detailed description of the figure parts, refer to the caption for Figure 5.4. The white horizontal isochronal line in D and E corresponds to 18 ms after the onset of S2.

Figure 5.8 illustrates the tissue response to stimulation of +2.3 mA in magnitude with an S1-S2 coupling interval of 180 ms. The corresponding location on the S-I curve is indicated by "2" in Figure 5.3B. The central region of negative polarization and the adjacent areas of more prominent positive polarization can be observed in Figure 5.8A and B. Despite the more distinctive positive polarization in comparison with Figure 5.7A, the activation does not happen at the VC regions; instead, charge diffusion occurs from

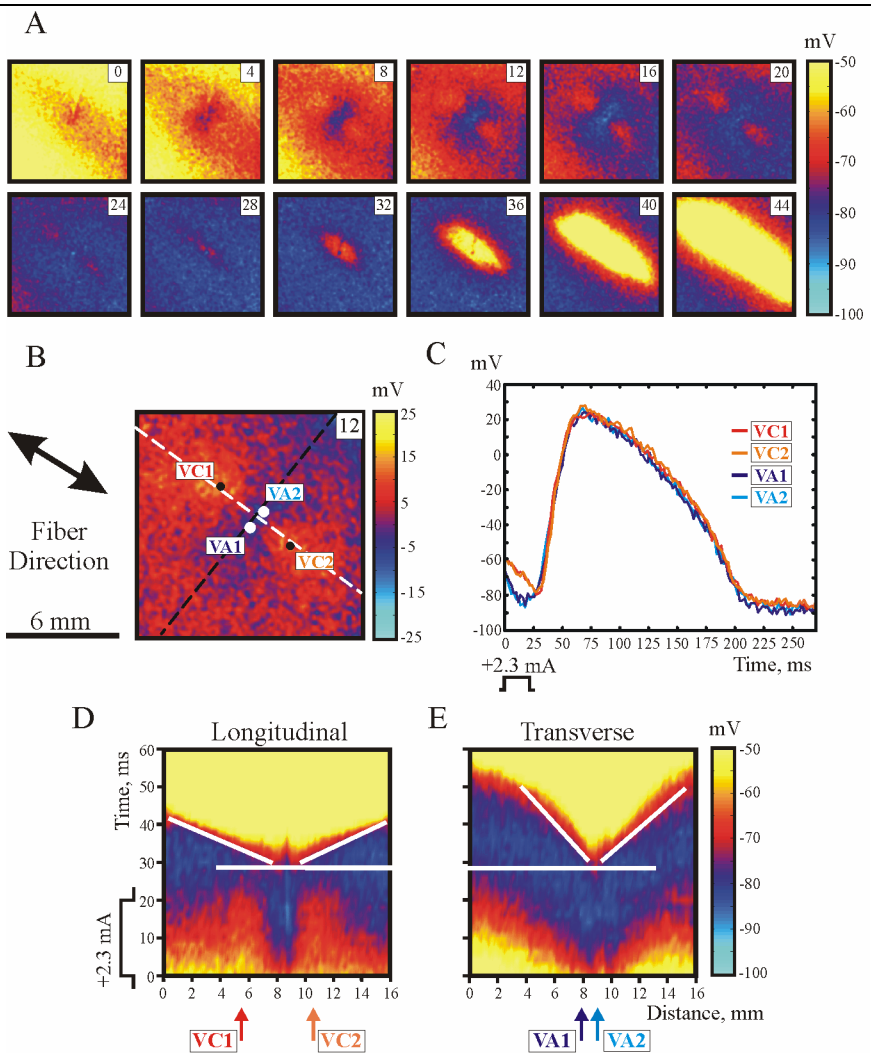

Figure 5.8. Anodal-break response to threshold stimulation in the RRP. The S1-S2 coupling interval is 180 ms. For the detailed description of the figure parts, refer to the caption for Figure 5.4. The white horizontal isochronal line in D and E corresponds to 28 ms after S2 onset.

the VC to the VA area (interval between 24 and 32 ms) after S2 termination. As a result, after the V_m reaches threshold at the VA site, the excitation initiates and propagates in a similar manner as the cathodal-make stimulation in Figure 5.4A. Four representative VC and VA optical APs in Figure 5.8C also indicate that excitation occurs first at the VA region. Two areas of depolarization corresponding to VCs are very distinguishable in Figure 5.8D during S2. However, the horizontal white isochronal line reveals that activation occurs at the same time in the two time-space plots: 10 ms after S2 termination, originating at the VA. The initiation of excitation at the central VA area with delay after S2 termination is characteristic of the anodal-break stimulation mechanism.

The V_m distribution over the stimulation site (1x1 mm^2) at the time of S2 application was –71.2 ± 2.0 mV (121 pixels) for make stimulation and –60 ± 2.4 mV (121 pixels) when stimulation occurred via the break mechanism.

Although VA hyperpolarization is not obvious in Figure 5.7B, small negative polarization can be observed in Figure 5.9A. The VC depolarization is stronger than VA hyperpolarization and displays maximums of +6.5 mV for the VC1 region and +6.1 mV for VC2 region versus the VA minimum of –4.7 mV. In break stimulation the stronger S2 strength induces a larger ΔV_m (Figure 5.9B). However, the difference in ΔV_m between make and break stimulation is more prominent for the VCs than for the VA area, and is statistically significant.

5.4.3. Stimulation close to the Effective Refractory Period: damped wave mediated response

Cathodal Stimulation. The ERP measured for cathodal stimulation was 134.4 ± 5.8 ms (N = 9). Figure 5.10 illustrates the analysis of the tissue response to stimulation

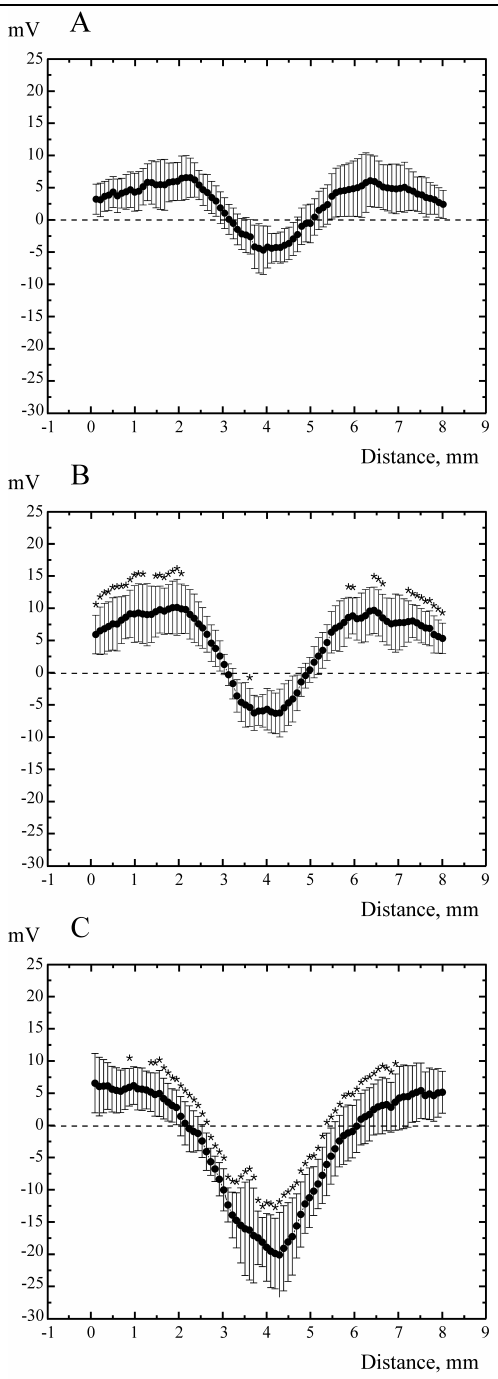

Figure 5.9. ΔV_m profiles during S2 of anodal make (A), break (B), and DW stimulation. ΔV_m profiles are represented as mean ± std. Asterisks in B indicate significant difference ($P<0.05$) between the make (A) and break (B) profiles, and those in C indicate significant difference ($P<0.05$) between the break (B) and DW (C) profiles. The mean values of the anodal S2 current were 1.48 ± 0.5 mA for make (A), 2.1 ± 0.7 mA for break (B), and 1.6 ± 0.7 mA for DW (C). N=11.

–2.3 mA in amplitude and 145 ms for the S1-S2 coupling interval. The corresponding point on the S-I curve in Figure 5.3A is indicated by "3". At the time of S2 delivery, the V_m around the electrode is –21.2 ± 1.2 mV (1x1 mm^2, 121 pixels). However, 16 ms after S2 onset the negative polarizations at VA1 and VA2 have magnitudes of -47.4 ± 1.9 mV and –43.5 ± 1.7 mV (1x1 mm^2, 121 pixels), accordingly. The depolarization at the VC at this time is elevated to –10.4 ± 3.4 mV (1x1 mm^2, 121 pixels). Similar to the previously described episode of cathodal-break stimulation (Figure 5.5A, 24-ms through 32-ms frames), charge diffusion from the VC to VA regions occurs after S2 termination (Figure 5.10A, 24-ms through 32-ms frames). However, charge diffusion does not successfully

generate full-amplitude APs at the VA regions, but initiates low amplitude damped waves (DW) (Figure 5.10A, 36-ms through 56-ms frames), that develop into regenerative responses at 6.6 mm and 6.2 mm from the stimulation site. The dog bone shaped VC and two VAs are very prominent in Figure 5.10B. Figure 5.10C shows that immediately after

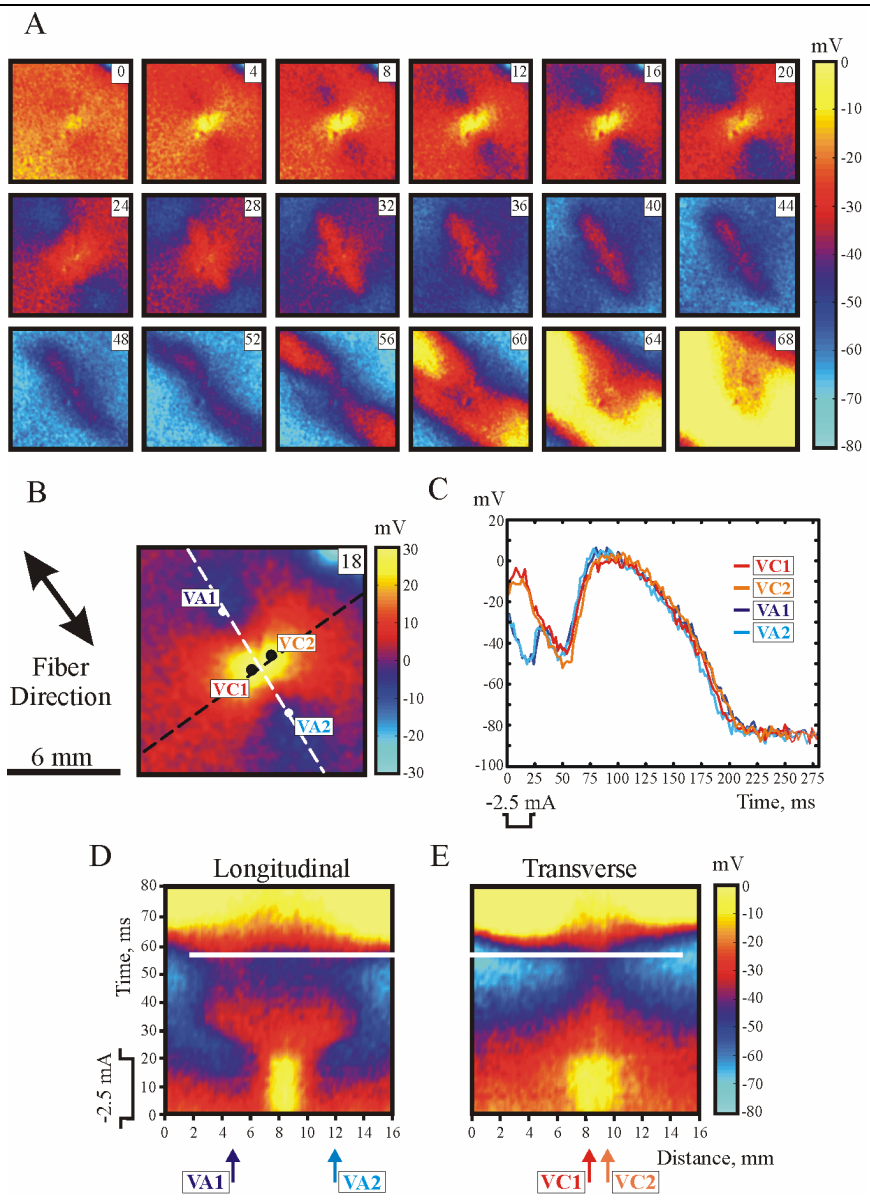

Figure 5.10. DW mediated response as a result of cathodal threshold stimulation close to the ERP using S1-S2 interval of 145 ms. A: The images of V_m distribution following S2 onset as a function of the time. B: ΔV_m during S2. C: Four VC and VA traces. D and E: TSPs along and transverse to the fiber direction. The white horizontal isochronal line corresponds to 56 ms after the start of S2.

S2 termination the voltage at the VC decreases whereas voltage at the VAs increases, indicating charge diffusion from the VC to VA areas. About 35 ms after S2 onset, the voltage at the VC and VA regions is almost equal. Thereafter, the VC and VA time traces do not intersect as V_m at the VA increases, which takes place for break stimulation (Figure 5.5). In this situation, the VA optical signals first exhibit decreasing voltage and then subsequent activation approximately 65 ms after S2 onset. The failure of the S2 stimulus to initiate full-amplitude responses at VA areas is obvious in the time-space plots (Figure 5.10D, E). After S2 termination, the transmembrane voltage immediately spreads out from the VC region about 2.5 mm and dissipates. Afterwards, longitudinal and transverse time-space plots reveal the excitation occurs about 45 ms after S2 termination.

Because of color saturation, it is difficult to show clearly both large and small V_m deflections with the same color scale in Figure 5.10A. To demonstrate that depolarization does not disappear between 36 and 56 ms, the movie of this time interval was further analyzed. The images of ΔV_m distribution as a function of time are displayed in Figure 5.11A. The detailed evolution of the wave front beginning at 28 ms is presented in Figure 5.11B and C. The dV_m/dt dynamics show decreasing amplitude between 28 and 36 ms followed by propagation to the upper left and lower right corners of the image. The isosurface plot in Figure 5.11C was constructed using a threshold of –0.2 mV/ms. Two knobs reflect the charge diffusion to the VAs, and two isthmuses represent DWs that eventually develop into the regenerative response.

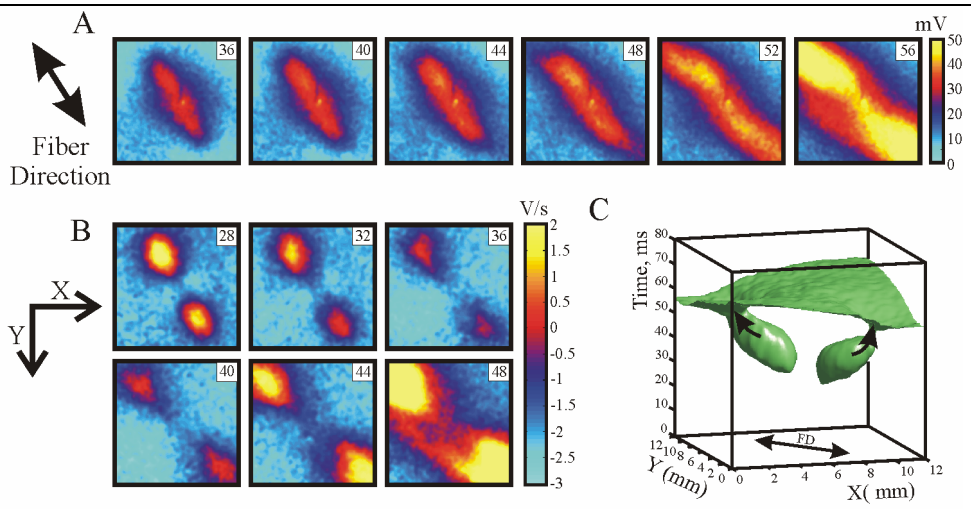

Figure 5.11. DW propagation after cathodal stimulation near refractoriness. A: Successive images of ΔV_m computed by subtracting the previous S1 AP from the S2 response. The numbers in the upper right represent the time (ms) since S2 onset. B: Images of dV_m/dt as a function of time. C: Isosurface plot of signal upstroke, constructed by sequential stacks of dV_m/dt contours using –0.2 V/s as the threshold. Black one-ended arrows indicate DWs, and the double arrow at the bottom shows the fiber direction.

The mean ΔV_m profile during stimulation early in the RRP, when excitability sharply decreases with shortening of the S1-S2 interval, is shown in Figure 5.6C. As compared with break stimulation at the end of RRP (Figure 5.6B), the most important difference between the two profiles is the increased negative polarization that occurs when the stronger S2 stimulus is applied. The differences in the minimum areas between the two profiles are 4.7 mV (VA1) and 4.2 mV (VA2). There is also a difference in the positive deflection (VC): this difference is smaller, however, at 3.7 mV.

Anodal Stimulation. The ERP for anodal stimulation was 129.5 ± 13.3 ms (N = 11). Figure 5.12 represents the response of the tissue to a +1.4 mA amplitude stimulus applied at a 130 ms S1-S2 coupling interval. The corresponding point in Figure 5.3B is indicated by "3" and is located in the dip of the S-I curve. Before S2 application V_m in the vicinity of the stimulation electrode was –11.7 ± 4.8 mV (1x1 mm^2, 121 pixels). During S2 the polarization at VC1 and VC2 was –22.8 ± 1.7 mV and –26 ± 1.3 mV, respectively;

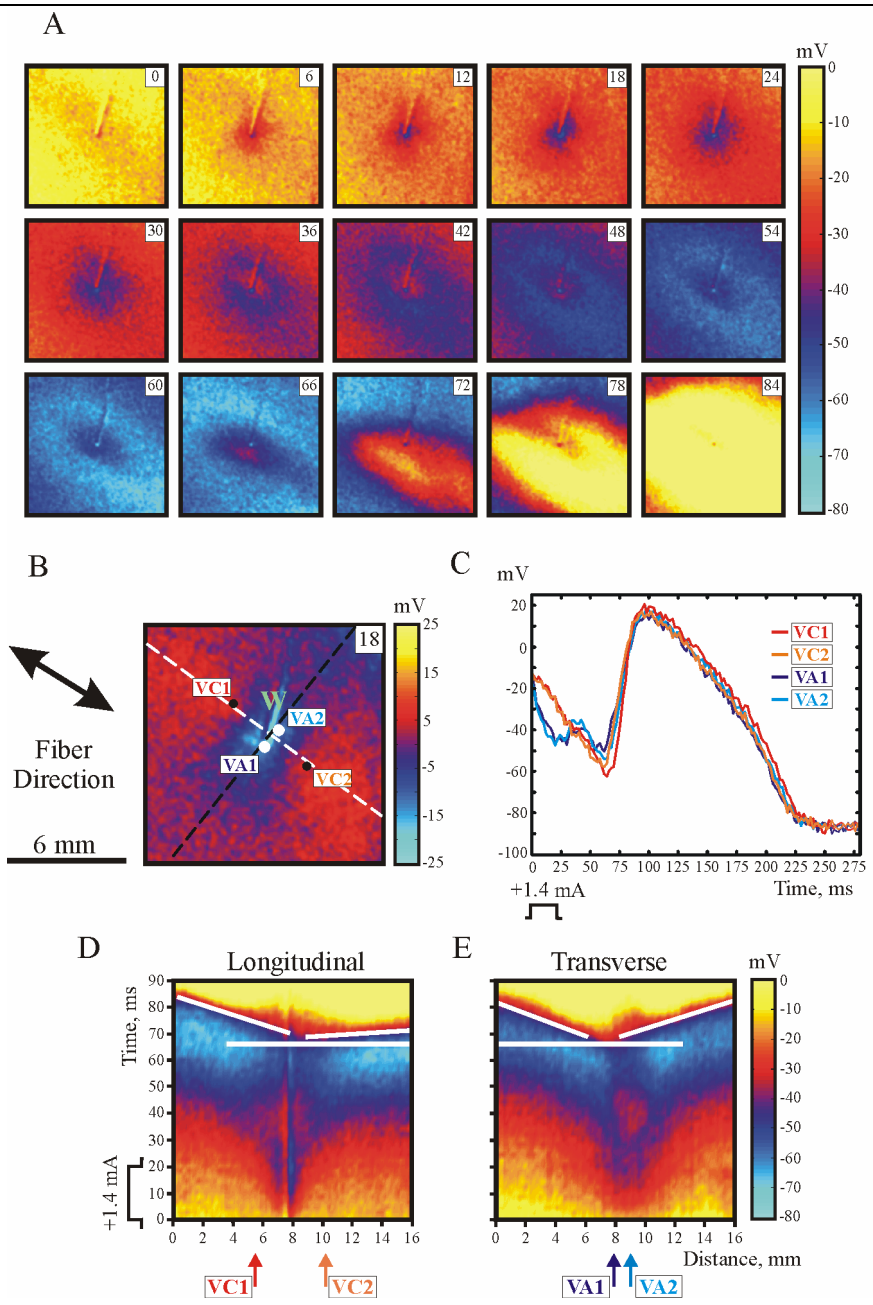

Figure 5.12. DW mediated response as a result of anodal threshold stimulation close to the ERP. The S1-S2 coupling interval is 130 ms. For the detailed description of the figure parts, refer to the caption for Figure 5.4. The artifact of the stimulating electrode is marked by the green "W" in B. The white horizontal isochronal line corresponds to 67 ms after S2 onset.

the transmembrane potential at the VA was –41.8 ± 5.2 mV (16ms, 1x1 mm^2, 121 pixels). After S2 termination, charge diffusion to the VA region is observed (24-ms through 42-ms frames, Figure 5.12A), but this voltage elevation fails to initiate a full-amplitude AP

at the VA area. The regenerative response occurs below the VA region with considerable delay, approximately 52 ms after S2 termination (72-ms frame, Figure 5.12A). While positive polarization is barely observed during S2 in Figure 5.12A, it is visible after S1 subtraction (Figure 5.12B). The VA traces presented in Figure 5.12C intersect the VC optical signals around the time interval of 35-40 ms, but then do not elevate to become regenerative APs as for anodal-break stimulation shown in Figure 5.8C; instead, the VA signals decrease in amplitude to –50 mV. Successive activation of the VC and VA regions occurs in the range of 70-78 ms. TSPs along and transverse to fiber direction in Figure 5.12D and E demonstrate an increase of the transmembrane potential in the central hyperpolarized area after stimulus termination, but no activation occurs immediately afterwards. The horizontal isochronal line shows the initiation of excitation at a delay about 50 ms after S2 termination. The site of origination of activation in Figure 5.12E is spatially shifted from the center in comparison with the time-space plot in Figure 5.8E, suggesting the stimulation occurs outside of the VA area.

Because the V_m deflection at the VA is too small to be distinguishable with color scale in Figure 5.12A, the movie section between 38 and 68 ms was extracted for additional analysis and represented separately in Figure 5.13. The set of ΔV_m (Figure 5.13A) and dV_m/dt (Figure 5.13B) images demonstrate that VA depolarization propagates towards the lower left corner of the image (Figure 5.13B) and converts into a regenerative response 2.3 mm from the location of the stimulation electrode. The isosurface plot in Figure 5.13C illustrates wave front dynamics after charge diffusion from the VCs to the central VA area. The central knob represents VA depolarization after

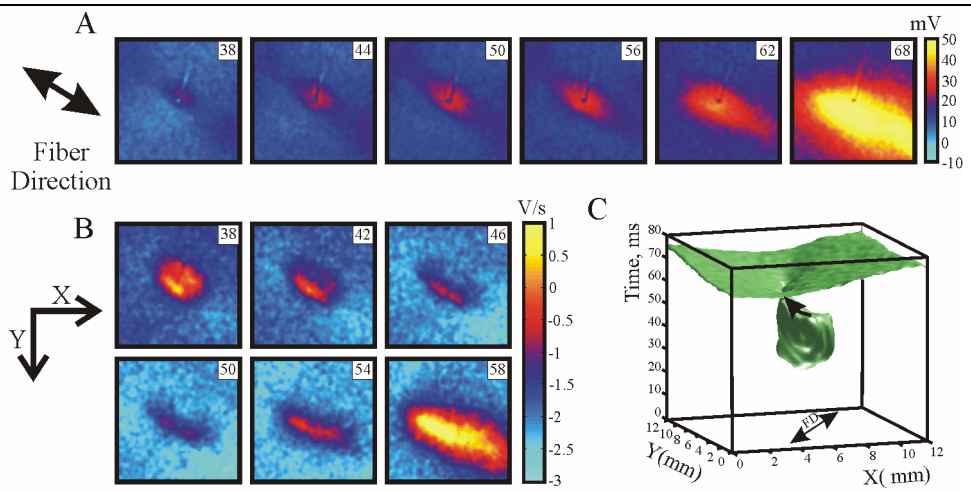

Figure 5.13. DW propagation after anodal stimulation near refractoriness. A: Successive ΔV_m images created by subtracting the previous S1 AP from the S2 response. B: Images of dV_m/dt as a function of time. C: Isosurface plot illustrating signal upstroke dynamics after S2 termination. The threshold for creating the isosurface was –0.85 V/s.

charge diffusion, which narrows into a thin isthmus with time and then evolves in a fast propagating AP.

Figure 5.9C shows the average ΔV_m profile at 10 ms after S2 onset for the S1-S2 intervals corresponding to the local minima of the dips of the S-I curves for anodal stimulation, indicating DW mediated excitation. One can see stronger central VA hyperpolarization for the DW mediated mode in comparison with the curve shown for break stimulation in Figure 5.9B.

5.5. Discussion

The shape of the S-I curve depends on inherent cardiac tissue properties, as well as the electrode design [6] and parameters of the stimulus pulses [8,9,21,22]. There is significant variability in the S-I curve appearance among different hearts even when the same electrode and stimulation protocol are used [8]. However, anodal stimulation always yields more complex dynamics through the cardiac cycle than cathodal

stimulation. The manifestation of supernormal excitability, wherein the excitability is higher than expected, is a more important distinction.

In Roth's theoretical study using Beeler-Reuter membrane dynamics [9], he computed S-I curves using stimuli durations of 2, 5, 10, and 20 ms. Our experimentally measured anodal S-I curves (Figure 5.2B) have the same characteristic shape of the numerical curves: a dip, plateau phase, and descent at the end of the RRP. In the numerical cathodal S-I curves, the dip only appeared for the 20-ms duration. For the shorter stimuli, the behavior of the theoretical cathodal S-I curves is very similar to our experimentally measured S-I curves illustrated in Figure 5.2A. The difference between the cathodal numerical and experimental data for stimulation of 20-ms duration could be the result of discrepancy in repolarization dynamics between the BR model and real cardiac tissue. In addition, though the numerical model is a three-dimensional bidomain with cylindrical symmetry, it does not represent realistic anatomical structure with fiber rotation, which can affect the spatial current distribution at the stimulation location. Another discrepancy is the lower thresholds for resting tissue in Roth's simulations (0.038 mA for cathodal and 0.41 mA for anodal stimulation) in comparison with our experimental measurements (0.15 ± 0.09 mA (N = 9) for cathodal and 1.05 ± 0.36 mA (N = 11) for anodal stimulation). The disparity in unipolar stimulation thresholds in numerical and experimental studies is well-known and has been discussed in the literature, although a definitive explanation has not been determined [23]. However, the anodal-cathodal threshold ratio for the theoretical data (factor of 10.8) is close to the ratio from our experiments (factor of 7.0). Additionally, the calculated S-I curves are shifted

toward longer S1-S2 coupling intervals in comparison with our experimentally measured curves: this is a result of the longer AP duration in the BR model (300 ms).

Roth [9] suggested three effects combined to produce the complicated shape of the S-I curve: weak active response at the VC regions, the change in membrane resistance, and depolarization of the tissue immediately before S2 application. During stimulation at the end of the RRP, when tissue is recovering from refractoriness, the weak nonpropagating VC active response can affect the threshold. Roth hypothesized that if stimulation is cathodal, the weak nonpropagating active response prolongs the refractoriness in the border region between the VC and VA. As a result, stronger stimulation is needed to overcome this refractoriness. Therefore the weak active response increases the stimulation threshold. However, under anode break stimulation late in the RRP, the elevation of depolarization at the VC due to local weak active response causes descent of the S-I curve as the interval increases. We believe that as long as the VC weak response increases depolarization, it elevates the voltage gradient between the VA and VC area. This increased voltage gradient will facilitate excitation and decrease threshold.

It is known that a steep change of resistance during an AP coincides with a phase of faster recovery during repolarization [24]. This faster recovery facilitates polarization at shorter of S1-S2 intervals and decreases the threshold. However, this phenomenon does not equally affect cathodal and anodal stimulation. It has been shown that stimulation during the plateau phase induces asymmetrical changes in V_m, yielding larger negative V_m changes than positive ones [25-28]. The L-type calcium current was suggested to underlie this nonlinear V_m change [29].

Why does a dip appear in the anodal S-I curve but not in the cathodal curve? If anodal stimulation is delivered early in the RRP, the effect of the nonlinear cardiac cell membrane behavior at the VA area overcomes the elevation of V_m due to the short S1-S2 interval and facilitates stimulation, causing the positive slope of the anodal S-I curve. When cathodal stimulation takes place early in the RRP, the spatial geometry of virtual electrode polarization dominates. Hyperpolarizing two VAs distant from the electrode requires larger current. Therefore no dip is observed in the cathodal S-I curve.

Thus, the transmembrane voltage immediately before S2 application determines the membrane conductance and affects the membrane nonlinear properties. In addition, for stimulation close to the ERP, the pre-stimulation V_m is crucial for unstable DWs with diminished amplitude and velocity, causing them to either dissipate or become full amplitude steadily propagating waves.

It has been shown that stimulation during the RRP can induce a graded response that depends on the stimulus magnitude and S1-S2 interval [28,30-34]. This response can be local or can propagate [31,35], forming DW with diminished amplitude and velocity [36]. What is the ionic mechanism of DW? In our study at the time of anodal S2 onset, the mean V_m around the electrode (1x1 mm^2) for S1-S2 intervals corresponding to the dip locations in the S-I curves is -16.1 ± 6.2 mV (1331 pixels, 11 experiments). During cathodal stimulation close to the ERP when excitability sharply increases with decreasing S1-S2 intervals, this value is -17.3 ± 3.9 (1089 pixels, 9 experiments). The mean values of depolarization measured at the end of the RRP when stimulation occurs via the break mechanism are -55.7 ± 4.6 mV (1331 pixels) and -53.7 ± 6.2 mV (1089 pixels) for anodal and cathodal stimulation, respectively. The gating of activation and inactivation

for the calcium current is known to operate under membrane potentials more positive than –40 mV, whereas the sodium current starts to activate at potentials higher than –70 mV and is almost completely inactivated under voltages higher than –60 mV [37]. Hence, it reasonable to expect that the calcium current is the dominant current in damped propagation, while the composition of the current underlying the break response during stimulation at the end of the RRP is similar to the current composition of the AP during diastolic stimulation. Further studies using simultaneous Ca^{2+} and Vm imaging are needed to validate this hypothesis.

Nikolski et al. [38] reported about break excitation during diastole. When stimulation was of near-threshold intensity, cathodal and bipolar stimulation revealed break excitation. If stimulation was anodal, the excitation followed the make mechanism. Later, they demonstrated that anodal break excitation also can occur in diastole, but was accompanied by an overshoot of the pacing current because of the half-cell double layer discharge. The addition of a diode in the stimulation circuit eliminated both the overshoot and the break excitation [39].

Lindblom et al. [40] conducted a theoretical study of excitability and arrhythmogenesis in the pinwheel experiment using the Beeler-Reuter Drouhard-Roberge model to represent membrane kinetics. Although they examined pinwheel stimulation protocol rather than point stimulation, their results for S2 stimuli occurring after 95% repolarization were similar to Roth's simulations in diastole [9]: make excitation was always observed. In our experiments the stimulation mechanism in diastole was make for both positive and negative polarities (Figure 5.3).

Limitations. To eliminate the mechanical distortion of optical signals, the electro-mechanical uncoupler BDM was utilized. It is known that this reagent can modify ion conductances [41-43] and, hence, can affect excitability. To determine if BDM affects the S-I curve, control measurements of excitability through the cardiac cycle without BDM were conducted. It was demonstrated that all typical characteristics of the cathodal and anodal S-I curves also were observed in hearts perfused without BDM.

Optical signals are estimated to originate from depths of 300-500 μm [11,44] up to about 1-2 mm [45-49]. On the other hand, tissue polarization falls off over a few electrotonic space constants. The space constants follow tissue anisotropy, with the smallest being transverse to the fiber direction. As was demonstrated in dog hearts, the value of the space constant depends on the type of cardiac tissue and varies from 920 μm to 1250 μm along the fiber direction and between 115 μm and 595 μm for the direction transverse to the fibers [50]. The depth of penetration for the polarization beneath the stimulating electrode is unknown, but it is assumed that this value is a few transverse space constants. Hence, the voltage measurements at the VA and VC can be underestimated if the electrical space constant is less than the optical decay constant [51]. In addition, averaging of the fluorescence over depth also can attenuate the appearance of damped propagation, causing DW to appear less prominent than they actually are.

5.6. Acknowledgements

The authors would like to thank John P. Wikswo for his support and encouragement and Bradley J. Roth for his comments and suggestions.

This work was supported by the National Institutes of Health (R01-HL58241) and the Academic Venture Capital Fund of Vanderbilt University. The work of M.C. Woods

was partially supported by a predoctoral fellowship from the American Heart Association (0215128B).

5.7. References

[1] Hoff, H. E. and Nahum, L. H., "The supernormal period in the mammalian ventricle." *Am J Physiol*, vol. 124 pp. 591-595, 1938.

[2] Adrian, E. D., "The recovery process of excitable tissues." *The Journal of Physiology*, vol. 54 pp. 1-31, 1920.

[3] Orias, O., Brooks, C., Suckling, E., Gilbert, L., and Siebens A., "Excitability of the mammalian ventricle throughout the cardiac cycle." *Am.J.Physiol.*, vol. 163 pp. 272-282, 1950.

[4] Hoffman, B. F., Gorin, E. F., Wax, F. S., Siebens, A. A., and Brooks, M. J., "Vulnerability to fibrillation and the ventricular-excitability curve" *Am J Physiol*, vol. 167 pp. 88-94, 1951.

[5] Cranefield, P. F., Hoffman, B. F., and Siebens, A. A., "Anodal excitation of cardiac muscle." *Am J Physiol*, vol. 190, no. 2, pp. 383-390, 1957.

[6] Mehra, R. and Furman, S., "Comparison of cathodal, anodal, and bipolar strength-interval curves with temporary and permanent pacing electrodes." *British Heart Journal*, vol. 41, no. 4, pp. 468-476, 1979.

[7] Brooks, C., Cranefield, P., Hoffman, B., and Siebens A., "Anodal effects during the refractory period of cardiac muscle." *J.Cell Physiol.*, vol. 48 pp. 237-241, 1956.

[8] Dekker, E., "Direct current make and break thresholds for pacemaker electrodes on the canine ventricle." *Circ Res*, vol. 27, no. 5, pp. 811-823, 1970.

[9] Roth, B. J., "Strength-interval curves for cardiac tissue predicted using the bidomain model." *J Cardiovasc Electrophysiol*, vol. 7, no. 8, pp. 722-737, 1996.

[10] Wikswo, J. P., Jr., "The complexities of cardiac cables: virtual electrode effects." *Biophys J*, vol. 66, no. 3 Pt 1, pp. 551-553, 1994.

[11] Knisley, S. B., "Transmembrane voltage changes during unipolar stimulation of rabbit ventricle." *Circ Res*, vol. 77, no. 6, pp. 1229-1239, 1995.

[12] Neunlist, M. and Tung, L., "Spatial distribution of cardiac transmembrane potentials around an extracellular electrode: dependence on fiber orientation." *Biophys J*, vol. 68, no. 6, pp. 2310-2322, 1995.

[13] Wikswo, J. P., Jr., Lin, S.-F., and Abbas, R. A., "Virtual electrodes in cardiac tissue: A common mechanism for anodal and cathodal stimulation." *Biophys J*, vol. 69, no. 6, pp. 2195-2210, 1995.

[14] Roth, B. J., "Electrical conductivity values used with the bidomain model of cardiac tissue." *IEEE Trans.Biomed.Eng.*, vol. 44 1997.

[15] Wikswo, J. P., "Tissue anisotropy, the cardiac bidomain, and the virtual cathode effect." in Zipes, D. P. and Jalife, J. (eds.) *Cardiac Electrophysiology, From Cell to Bedside* Second ed. Philadelphia: W.B. Saunders Co., 1995, pp. 348-361.

[16] Sepulveda, N. G. and Wikswo, J. P., Jr., "Electric and magnetic fields from two-dimensional anisotropic bisyncytia." *Biophys J*, vol. 51, no. 4, pp. 557-568, 1987.

[17] Sepulveda, N. G., Roth, B. J., and Wikswo, J. P., Jr., "Current injection into a two-dimensional anisotropic bidomain." *Biophys J*, vol. 55 pp. 987-999, 1989.

[18] Roth, B. J., "A mathematical model of make and break electrical stimulation of cardiac tissue by a unipolar anode or cathode." *IEEE Trans Biomed Eng*, vol. 42, no. 12, pp. 1174-1184, 1995.

[19] Sidorov, V. Y., Woods, M. C., and Wikswo, J. P., "Effects of elevated extracellular potassium on the stimulation mechanism of diastolic cardiac tissue." *Biophys J*, vol. 84, no. 5, pp. 3470-3479, 2003.

[20] Wikswo, J. P., Altemeier, W., Balser, J. R., Kopelman, H. A., Wisialowski, T., and Roden, D. M., "Virtual cathode effects during stimulation of cardiac muscle: Two-dimensional in vivo measurements." *Circ Res*, vol. 68, no. 2, pp. 513-530, 1991.

[21] Alferness, C., Bayly, P. V., Krassowska, W., Daubert, J. P., Smith, W. M., and Ideker, R. E., "Strength-interval curves in canine myocardium at very short cycle lengths." *PACE*, vol. 17, no. 5 Pt 1, pp. 876-881, 1994.

[22] Bennett, J. A. and Roth, B. J., "Dependence of cardiac strength-interval curves on pacing rate." *Med Biol Eng Comput*, vol. 37, no. 1, pp. 108-109, 1999.

[23] Roth, B. J., "Artifacts, assumptions, and ambiguity: Pitfalls in comparing experimental results to numerical simulations when studying electrical stimulation of the heart." *Chaos*, vol. 12, no. 3, pp. 973-981, 2002.

[24] Goldman, Y. and Morad, M., "Ionic membrane conductance during the time course of the cardiac action potential." *J.Physiol.*, vol. 268 pp. 655-695, 1977.

[25] Zhou, X. H., Smith, W. M., Rollins, D. L., and Ideker, R. E., "Transmembrane potential changes caused by shocks in guinea pig papillary muscle" *Am J Physiol Heart Circ Physiol*, vol. 271, no. 6, pp. H2536-H2546, 1996.

[26] Fast, V. G., Rohr, S., and Ideker, R. E., "Nonlinear changes of transmembrane potential caused by defibrillation shocks in strands of cultured myocytes." *Am J Physiol Heart Circ Physiol*, vol. 278, no. 3, pp. H688-H697, 2000.

[27] Cheng, D. K., Tung, L., and Sobie, E. A., "Nonuniform responses of transmembrane potential during electric field stimulation of single cardiac cells." *Am J Physiol Heart Circ Physiol*, vol. 277, no. 1, pp. H351-H362, 1999.

[28] Gray, R. A., Huelsing, D. J., Aguel, F., and Trayanova, N. A., "Effect of strength and timing of transmembrane current pulses on isolated ventricular myocytes." *J Cardiovasc Electrophysiol*, vol. 12, no. 10, pp. 1129-1137, 2001.

[29] Cheek, E. R., Ideker, R. E., and Fast, V. G., "Nonlinear changes of transmembrane potential during defibrillation shocks - Role of Ca2+ current" *Circ.Res.*, vol. 87, no. 6, pp. 453-459, 2000.

[30] Gotoh, M., Uchida, T., Mandel, W. J., Fishbein, M. C., Chen, P.-S., and Karagueuzian, H. S., "Cellular graded responses and ventricular vulnerability to reentry by a premature stimulus in isolated canine ventricle." *Circulation*, vol. 95, no. 8, pp. 2141-2154, 1997.

[31] Kao, C. Y. and Hoffman, B. F., "Graded and decremental responses in heart muscle fibers." *Am J Physiol*, vol. 194, no. 1, pp. 187-196, 1958.

[32] Evans, F. G. and Gray, R. A., "Shock-induced epicardial and endocardial virtual electrodes leading to ventricular fibrillation via reentry, graded responses, and transmural activation." *J.Cardiovasc.Electrophysiol.*, vol. 15 pp. 79-87, 2004.

[33] Hoffman, B. F., Kao, C. Y., and Suckling, E. E., "Refractoriness in cardiac muscle." *Am.J.Physiol.*, vol. 190 pp. 473-482, 1957.

[34] Efimov, I. R., Gray, R. A., and Roth, B. J., "Virtual electrodes and deexcitation: New insights into fibrillation induction and defibrillation." *J Cardiovasc Electrophysiol*, vol. 11, no. 3, pp. 339-353, 2000.

[35] Trayanova, N. A., Gray, R. A., Bourn, D. W., and Eason, J. C., "Virtual electrode-induced positive and negative graded responses: New insights into fibrillation induction and defibrillation" *J.Cardiovasc.Electrophysiol.*, vol. 14, no. 7, pp. 756-763, 2003.

[36] Sidorov, V. Y., Aliev, R. R., Woods, M. C., Baudenbacher, F., Baudenbacher, P., and Wikswo, J. P., "Spatiotemporal dynamics of damped propagation in excitable cardiac tissue." *Phys Rev Lett*, vol. 91, no. 20, pp. 208104, 2003.

[37] Beeler, G. W. and Reuter, H., "Reconstruction of the action potential of ventricular myocardial fibres." *J Physiol (Lond)*, vol. 268, no. 1, pp. 177-210, 1977.

[38] Nikolski, V. P., Sambelashvili, A. T., and Efimov, I. R., "Mechanisms of make and break excitation revisited: paradoxical break excitation during diastolic stimulation." *Am J Physiol Heart Circ Physiol*, vol. 282, no. 2, pp. H565-H575, 2002.

[39] Nikolski, V., Sambelashvili, A., and Efimov, I. R., "Anode-break excitation during end-diastolic stimulation is explained by half-cell double layer discharge" *IEEE Trans.Biomed.Eng.*, vol. 49, no. 10, pp. 1217-1220, 2002.

[40] Lindblom, A. E., Roth, B. J., and Trayanova, N. A., "Role of virtual electrodes in arrhythmogenesis: Pinwheel experiment revisited" *J.Cardiovasc.Electrophysiol.*, vol. 11, no. 3, pp. 274-285, 2000.

[41] Biermann, M., Rubart, M., Moreno, A., Wu, J., Josiah-Durant, A., and Zipes, D. P., "Differential effects of cytochalasin D and 2,3 butanedione monoxime on isometric twitch force and transmembrane action potential in isolated ventricular muscle: implications for optical measurements of cardiac repolarization." *J Cardiovasc Electrophysiol*, vol. 9, no. 12, pp. 1348-1357, 1998.

[42] Cheng, Y., Li, L., Nikolski, V., Wallick, D. W., and Efimov, I. R., "Shock-induced arrhythmogenesis is enhanced by 2,3-butanedione monoxime compared with cytochalasin D." *Am J Physiol Heart Circ Physiol*, vol. 286, no. 1, pp. H310-H318, 2004.

[43] Watanabe, Y., Iwamoto, T., Matsuoka, I., Ohkubo, S., Ono, T., Watano, T., Shigekawa, M., and Kimura, J., "Inhibitory effect of 2,3-butanedione monoxime (BDM) on Na^+/Ca^{2+} exchange current in guinea-pig cardiac ventricular myocytes." *Br.J.Pharmacol.*, vol. 132, no. 6, pp. 1317-1325, 2001.

[44] Girouard, S. D., Laurita, K. R., and Rosenbaum, D. S., "Unique properties of cardiac action potentials recorded with voltage-sensitive dyes." *J Cardiovasc Electrophysiol*, vol. 7, no. 11, pp. 1024-1038, 1996.

[45] Al-Khadra, A., Nikolski, V., and Efimov, I. R., "The role of electroporation in defibrillation." *Circ Res*, vol. 87, no. 9, pp. 797-804, 2000.

[46] Baxter, W. T., Mironov, S. F., Zaitsev, A. V., Jalife, J., and Pertsov, A. M., "Visualizing excitation waves inside cardiac muscle using transillumination." *Biophys J*, vol. 80, no. 1, pp. 516-530, 2001.

[47] Efimov, I. R., Sidorov, V., Cheng, Y., and Wollenzier, B., "Evidence of three-dimensional scroll waves with ribbon-shaped filament as a mechanism of ventricular tachycardia in the isolated rabbit heart." *J Cardiovasc Electrophysiol*, vol. 10, no. 11, pp. 1452-1462, 1999.

[48] Ding, L., Splinter, R., and Knisley, S. B., "Quantifying spatial localization of optical mapping using Monte Carlo simulations." *IEEE Trans Biomed Eng*, vol. 48, no. 10, pp. 1098-1107, 2001.

[49] Bray, M. A. and Wikswo, J. P., "Examination of optical depth effects on fluorescence imaging of cardiac propagation" *Biophys.J.*, vol. 85, no. 6, pp. 4134-4145, Dec.2003.

[50] Kukushkin, N. I., Bukauskas, F. F., Sakson, M. E., and Nasonova, V. V., "Anisotropy of stationary rates and delays in extrasystolic waves in the dog heart." *Biofizika*, vol. 20, no. 4, pp. 687-692, 1975.

[51] Janks, D. L. and Roth, B. J., "Averaging over depth during optical mapping of unipolar stimulation." *IEEE Trans Biomed Eng*, vol. 49, no. 9, pp. 1051-1054, 2002.

CHAPTER VI

FIELD STIMULATION OF THE DIASTOLIC RABBIT HEART: THE ROLE OF SHOCK STRENGTH AND DURATION ON EPICARDIAL ACTIVATION AND PROPAGATION

Marcella C. Woods[1], Veniamin Y. Sidorov[1,2,3], Mark R. Holcomb[2], David N. Mashburn[2], John P. Wikswo[1,2,3,4]

[1]Department of Biomedical Engineering

[2]Department of Physics and Astronomy

[3]Vanderbilt Institute for Integrative Biosystems Research and Education

[4]Department of Molecular Physiology and Biophysics

Vanderbilt University, Nashville, Tennessee

This chapter presents the experimental diastolic field shock data. In mid-November we are meeting with M. M. Maleckar and N. A. Trayanova of Tulane University to combine our experimental work with their corresponding bidomain simulations using an anatomically accurate model of the rabbit ventricles. The resulting manuscripts will be submitted for publication in *Circulation Research*.

6.1. Abstract

Although defibrillation therapy has become an invaluable medical procedure, the mechanisms by which strong external shocks alter the cardiac transmembrane potential to terminate fibrillation are still unclear. Much research has been directed at examining field stimulation of systolic tissue, but field stimulation of the diastolic heart is also important. Field shocks of 1 to 50 V/cm of varying duration were delivered during diastole to di-4-ANEPPS stained isolated rabbit hearts placed in a bath of Tyrode's solution. High-speed optical imaging was utilized to observe the tissue response to the shocks. We found decreasing activation time with increasing shock strength when the stimulus duration was 2 ms. When shock duration was varied for strong stimulation (50 V/cm), activation time first decreased rapidly then increased more slowly with increasing shock duration. Shock-induced negative virtual electrode polarization caused delayed activation at longer shock durations. Delayed activation from hyperpolarization was more prominent for the left ventricle than for the right ventricle.

6.2. Introduction

Externally-applied electric fields are known to cause changes in transmembrane potential (V_m) at locations distant from the stimulating electrodes, a phenomenon termed "far-field" stimulation. This is counter to the predictions of standard cable models in which the changes in V_m fall off exponentially with distance from the stimulating electrodes. Many possible explanations for far-field stimulation have been presented. Plonsey and Barr [1] hypothesized that intercellular resistances at gap junctions cause depolarization and hyperpolarization on opposite ends of each myocyte. However, attempts to experimentally verify the "saw-tooth" effect in intact cardiac tissue have

failed [2,3]. Theoretical simulations using the bidomain model of cardiac tissue predict that fiber curvature and unequal anisotropy ratios between the intra- and extracellular spaces cause depolarization and hyperpolarization throughout the heart [4-6]. These regions of positive and negative polarization far from the stimulating electrodes are called virtual cathodes and virtual anodes, respectively; collectively, they are known as "virtual electrode" polarization.

Other heterogeneities have been hypothesized as contributors to the mechanism of far-field stimulation. Computer models incorporating syncytial heterogeneities of the bulk myocardium revealed islands of hyperpolarization and depolarization during an external electric shock [7]. On the level of macroscopic heterogeneities, the heart can be modeled as a collection of short fibers that, when exposed to an external electrical field, should produce hyperpolarization and depolarization in a patchy manner corresponding with each region [8]. In addition, cleavage planes between muscle layers may cause non-uniform, anisotropic propagation and also provide a substrate for bulk resetting of the myocardium during defibrillation [9].

The boundary conditions of the heart surfaces also impact how an electric field alters V_m. Latimer and Roth [10] modeled a slab of tissue with an intercavitary electrode in two conditions: the epicardium bounded by air and the epicardium bounded by a conductive bath. They found that the conductive bath reverses the sign of V_m in some regions and dramatically increases the magnitude of the shock-induced changes in V_m at the epicardial surface. Additionally, V_m falls off rapidly with depth into the tissue, suggesting that the optically-measured V_m would be much smaller than the true epicardial V_m. Entcheva *et al.* [11] modeled an ellipsoid bidomain heart with transmural fiber

rotation using different boundary conditions. They found that the induced change in V_m partially results from the tissue boundary conditions, and is not fully determined by tissue anisotropy. When the bath is highly conductive, border polarization occurs at the surfaces, potentially masking the surface virtual electrode effects. If the bath is less conductive or if the boundary is insulating (*i.e.* tissue against glass) bulk virtual electrode polarization can break through and appear on the epicardial surface. Additionally, the conductivity of the bath changes the appearance of the virtual electrode polarization on the epicardial surface.

Each of these hypotheses incorporates heterogeneities as a mechanism for producing adjacent regions of positive and negative polarization during an external electric shock. These adjacent areas of polarization are potential sources of wave front generation that could cause the far-field stimulation observed during field shocks.

Although much research has been directed at studying the effects of field stimulation on systolic tissue, the effects of field stimulation on diastolic tissue are equally important but have been less investigated because of the complication of sodium channel activation [12,13]. In one experimental study of diastolic field stimulation, Sharifov and Fast applied shocks transmurally across an isolated pig left ventricle [14]. They found direct and rapid activation of the ventricular bulk and delayed activation and multi-phasic transmembrane potential responses at very strong shock strengths. However, because they were imaging the cut end of a preparation, the extent to which the angles of the cut fibers at the tissue surface, damage, and ischemia contributed to their results is unknown [15,16]. To our knowledge, there has not been a systematic, quantitative experimental examination of the response of the isolated whole, intact heart to field

shocks applied during diastole. In this chapter, we present analyses of the roles of both shock strength and shock duration on whole heart epicardial activation and propagation.

6.3. Materials and Methods

6.3.1. Experimental Preparation

All experiments conformed to the National Institutes of Health guidelines for the ethical use of animals in research and were pre-approved by the Vanderbilt Institutional Animal Care and Use Committee.

New Zealand white rabbits (2.2-3.6 kg) were first preanesthetized with intramuscular ketamine (50 mg/kg). Intravenous heparin (2000 units) and pentobarbital (60 mg/kg) were then administered, and the hearts were excised quickly and Langendorff-perfused on a custom-built "C-shaped" glass arm. The ascending aorta was cannulated and secured for retrograde perfusion of the coronary arteries with oxygenated (95% O2; 5% CO2) Tyrode's solution of the following composition (in mM): 133 NaCl, 4 KCl, 2 $CaCl_2$, 1 $MgCl_2$, 1.5 NaH_2PO_4, 20 $NaHCO_3$, and 10 glucose. The temperature of the solution was maintained at 37° C, and the pH was regulated to 7.4 ± 0.05. To minimize motion artifacts, the excitation-contraction decoupler diacetyl monoxime (DAM, Sigma-Aldrich, St. Louis, MO) was added to the Tyrode's solution at a concentration of 15-20 mmol/L. To prevent buoyancy of the heart in the bath, the heart was secured to the glass arm by two sutures: one near the apex and one through the posterior heart, carefully avoiding major vessels. The heart was then positioned in a warmed, oxygenated, circulating bath of Tyrode's solution such that the anterior heart could be imaged.

6.3.2. Stimulation Protocol

Pacing stimuli (S1) were delivered via an insulated bipolar electrode with less than 1 mm of the platinum wire tips exposed (0.2 mm diameter, 2 mm spacing between poles). The S1 stimuli, provided by a computer-controlled current source (Bloom Associates, Narberth, PA), were 4 ms long and 2 times threshold intensity and continuously delivered at a basic cycle length of 300-350 ms. Ten conditioning S1 pulses preceded the field shocks.

The field shocks (S2) were produced by a custom, computer-controlled high-voltage stimulator (Ventritex, Sunnyvale, CA) and applied via titanium plates positioned at both ends of the bath, such that they faced right and left ventricles. To examine the role of shock strength, 2 ms S2 shocks of 1 to 30 V/cm were applied during diastole (S1-S2 coupling interval of 300-350 ms). The short 2 ms duration was used to separate the shock-induced response from sodium channel activation. To examine the role of shock duration, 50 V/cm shocks of 0.1 to 8 ms duration were delivered to diastolic tissue at a S1-S2 coupling interval of 350 ms. Current and voltage wave forms were monitored on a digital phosphor oscilloscope (TDS5034B, Tektronix, Richardson, TX) via a current probe (TCP305, Tektronix) and a high voltage differential probe (P5205, Tektronix) connected to two Ag-AgCl electrodes (2 mm diameter, model E252, In Vivo Metric, Healdsburg, CA) in the bath.

6.3.3. Optical Imaging

To view changes in V_m, 200 μL of the voltage-sensitive fluorescent dye di-4-ANEPPS (0.5 mg/mL dimethyl sulfoxide; Molecular Probes, Eugene, OR) was administered via a bolus injection into a bubble trap above the aorta. The anterior heart

was illuminated by a diode-pumped, solid-state 532 nm laser (Verdi, Coherent, Santa Clara, CA). The emitted light was passed through a cutoff filter (no. 25 Red, 607 nm, Tiffen, Japan). In some experiments, images were simultaneously acquired with a high spatial resolution Dalsa CCD camera (Waterloo, Ontario, Canada; 128×128 pixels, 487 frames/sec) and a high temporal resolution Redshirt CCD camera (Decatur, GA; 26×26 pixels, 5051 frames/sec) by using a partially silvered mirror with 70% transmission and 30% reflection. In other experiments, the Dalsa camera alone was used. Figure 6.1 shows the view of the anterior rabbit heart with the Dalsa CCD camera. The typical field of view required to image the whole rabbit heart was 5×5 cm^2.

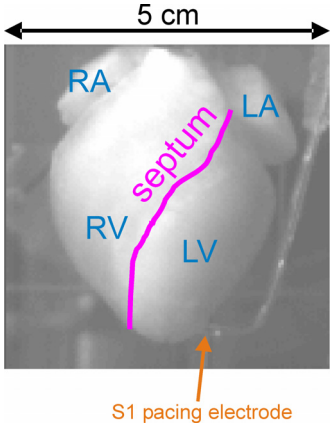

Figure 6.1. View of the anterior rabbit heart. The locations of the right atrium (RA), left atrium (LA), right ventricle (RV), left ventricle (LV), and septum are marked. The placement of the S1 pacing bipolar electrode is shown near the apex. The field of view was typically 5×5 cm^2.

6.3.4. Data Processing and Analysis

Data acquired with the Dalsa camera were spatially filtered with a 3×3 Gaussian filter. When necessary to improve signal quality, data acquired with the Redshirt camera were also spatially filtered. To preserve the shock timing, no temporal filtering was utilized. In some figures the fluorescence (F) data are presented as the ratio of the change in F to the background F before the shock ($\Delta F/F$). In other analyses, data were first normalized on a pixel-by-pixel basis according to the change in F during the S1 pacing response. The resulting normalized data (F_{norm}) ranged from 0 (rest) to 1 (peak) for the S1 response. Pixels corresponding to atrial tissue were digitally removed from the data and subsequent analyses.

Field shock activation times (AT) for each ventricular pixel were computed as the elapsed time from stimulus onset until 50% of the S1 action potential amplitude was reached (0.5 for F_{norm}). Total AT is the time from shock onset until the last ventricular pixel achieves the activation threshold of 0.5. Total AT was also computed for regions of interest corresponding to the left ventricle (LV) and right ventricle (RV) in order to discern activation differences between the two chambers. In these cases, total AT is the time from shock onset until the last pixel in the region of interest reaches the activation threshold.

To obtain a measure of activation dynamics for the whole heart, the sum of F_{norm} for all ventricular pixels for each movie frame was computed. The result was normalized by dividing by the number of pixels summed to yield F_{avg}. This signal is functionally equivalent to a whole-heart surface recording of V_m.

6.4. Results: Role of Shock Strength

We examined the role of shock strength using a shock duration of 2 ms. Shock strengths of 1 to 30 V/cm were tested.

6.4.1. Response to Weak Shocks

Figure 6.2 shows the V_m response of two different hearts to 2 ms, 1 V/cm electric field stimulation of both polarities. Hyperpolarization is not observed for the weak shock strengths. Activation is very slow, mostly resulting from propagation from the site of initial epicardial activation, and does not begin until long after the shock is terminated. The initial site of shock-induced activation may be a transmural location corresponding to an anatomical heterogeneity, such as a papillary muscle insertion, or in other cases appears to originate from within the septal wall. We observe different activation timing

and patterns in different hearts, suggesting that anatomical differences amongst hearts and variations in the way the heart is mounted on the goniometer may play a role in activation in response to weak shock strengths.

The green asterisks in the first frames of Figure 6.2 mark the sites of initial epicardial activation from 1 V/cm field stimulation. In Figure 6.2A, the initial site of activation is high on the left ventricle when the field is applied from left to right (top row). When the field is reversed, the initial site of activation corresponds to the septal wall near the apex (Figure 6.2A, bottom row). For this heart, activation is quite slow: the first signs of epicardial activation do not appear for 32 ms after shock onset, and activation of the whole heart is not complete until approximately 96 ms after the shock. For a different heart, 1 V/cm field stimulation results in much faster activation. When the electric field is

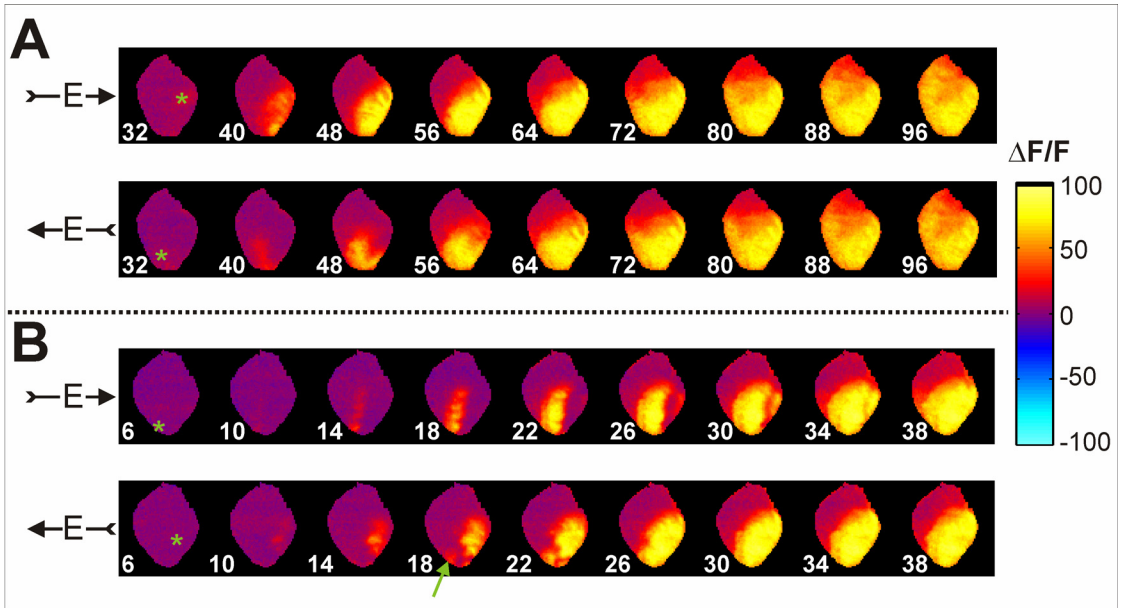

Figure 6.2. Response to weak field stimulation. This figure shows the response of two different hearts (A and B) to 1 V/cm field stimulation of both polarities. The shock duration is 2 ms. The numbers in the lower left of each frame indicate the time [ms] since shock onset. Green asterisks in the first frames indicate the site of first activation on the epicardial surface. Green arrow in the bottom row of *B* indicates a second site of epicardial activation. Direction of the shock is indicated by the arrows: when the anode faces the LV, the direction is "←", and when the cathode faces the LV the direction is "→". Images were acquired with the Dalsa CCD camera (128×128 pixels at 487 frames/sec).

applied from left to right, activation begins approximately 6 ms after shock onset and originates at the septal wall near the apex (Figure 6.2B, top row). Further activation of the septum occurs in the 10-18 ms frames. The site of initial activation changes to a mid-LV location when the field is reversed (Figure 6.2B, bottom row).In the 18-ms frame, the initial site of activation for the opposite polarity (RV near the apex, as indicated by the green arrow in the bottom row of Figure 6.2B) appears to activate at a rate which is faster than would be expected from propagation from the mid-LV site of initial activation. This second region of epicardial activation suggests that there is a second site of transmural activation that is farther away from the epicardial surface than the first site. The resulting propagation from the second site has to move across a longer distance to reach the epicardial surface, resulting in a delayed epicardial site of activation breakthrough. By 38-ms most of the epicardial surface is activated for both polarities.

6.4.2. Response to Strong Shocks

Figure 6.3 shows the response of one rabbit heart to 30 V/cm field stimulation (2 ms duration) as imaged with the high temporal resolution Redshirt camera. Here we see rapid, direct activation of the heart in comparison with the weak shock strength. Dependence of activation upon the polarity of the electric field is also observed. When the anode faces the LV (Figure 6.3A), hyperpolarization of the LV is stronger and more obvious than RV hyperpolarization when the polarity is reversed (Figure 6.3B). Additionally, when the anode is at the LV, hyperpolarization of the LV slows activation in comparison with the other field polarity.

Figure 6.4 shows the high spatial resolution images acquired simultaneously with the Dalsa CCD. These images show the importance of high temporal resolution for

viewing the shock-induced negative virtual electrode polarization of diastolic tissue. In Figure 6.3, which shows the high temporal resolution data acquired with the Redshirt camera (5051 frames/sec), there are 10 frames corresponding to the shock application in which hyperpolarization can be viewed and characterized. In Figure 6.4 the 2-ms shock corresponds to less than one frame (487 frames/sec). LV hyperpolarization is noted in the 0 and 2-ms frames (Figure 6.4A), and for the opposite polarity RV hyperpolarization is only visible in the 0-ms frame (Figure 6.4B).

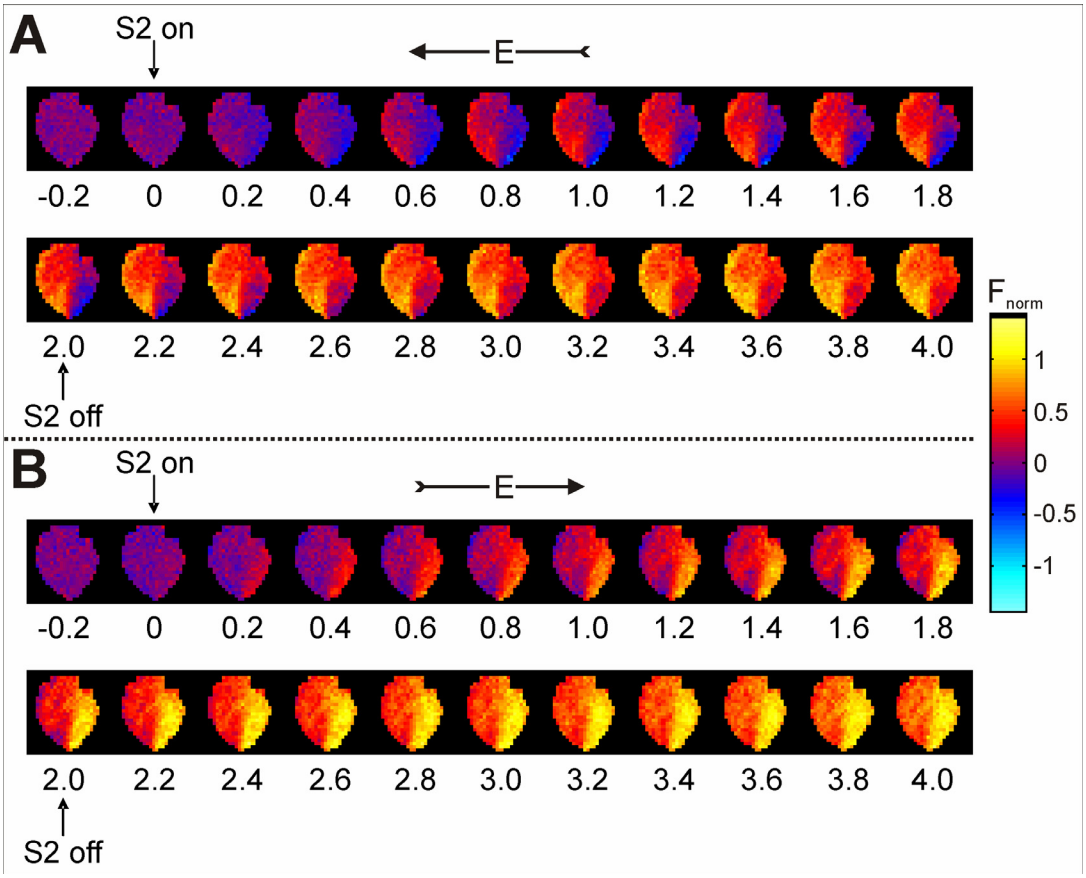

Figure 6.3. Response to strong field stimulation, acquired with high temporal resolution. This figure shows the spatiotemporal response of one heart to 30 V/cm field stimulation. The shock duration is 2 ms. In (A) the electric field is applied from right to left and in (B) the field is applied from left to right. The numbers below frame indicate the time [ms] since shock onset. Images were acquired with the Redshirt CCD camera (26×26 pixels at 5051 frames/sec).

6.4.3. *Analysis of Shock Strength*

Figure 6.5 shows the V_m response at the onset of the field shock for the range of strengths tested. For the weakest shocks (1 and 3 V/cm) no immediate activity is observed with S2 onset; activation occurs long after S2 onset. At 5 V/cm, hyperpolarization and depolarization of the LV occurs, depending upon shock polarity. When the field is applied from right to left, we begin to see hyperpolarization of the LV and depolarization of the RV for 7 and 10 V/cm stimulation. When the anode faces the RV, depolarization of the LV edge occurs but hyperpolarization of the RV is not observed. At 15 and 20 V/cm, when the anode faces the LV we see strong RV depolarization and LV hyperpolarization. When the

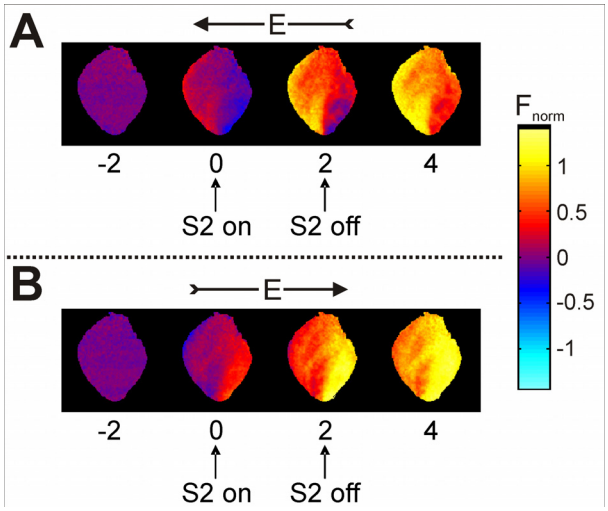

Figure 6.4. Response to strong field stimulation, acquired with high spatial resolution but only 2 ms temporal resolution. This figure shows the high spatial resolution data that was acquired simultaneously with the high temporal resolution data shown in Figure 6.3. The electric field strength is 30 V/cm applied (A) right-to-left and (B) left-to-right. The shock duration is 2 ms. The numbers below the frame indicate the time [ms] since shock onset. Images were acquired with the Dalsa CCD camera (128×128 pixels at 487 frames/sec).

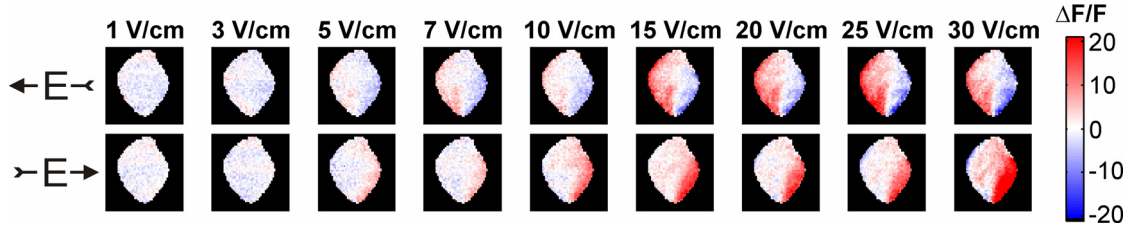

Figure 6.5. Summary of response to diastolic field stimulation of the isolated rabbit heart as a function of shock strength and polarity. The frames depicted correspond to S2 onset. Shocks of 2 ms duration were applied in the direction indicated. The upper limit of the color scale is saturated at the strongest strengths. These data were acquired with high spatial resolution (Dalsa camera, 128×128 pixels at 487 frames/sec).

anode faces the RV, we see strong LV depolarization and some slight hyperpolarization of the RV edge and RV near the junction of the apex and septum. For the strongest shocks (25 and 30 V/cm), when the anode faces the LV we see strong RV depolarization and strong LV hyperpolarization. For the opposite polarity, LV depolarization is very strong and RV hyperpolarization of small magnitude is noted at the RV edge and on the RV side of the apex.

To compare whole heart activation as a function of shock strength and polarity, we computed F_{avg} for all ventricular pixels (Figure 6.6A). F_{avg} was also calculated for a normally propagating paced response (S1) and for sinus activation. The S1 trace was aligned with the field shock traces according to stimulus pulse onset. The sinus trace was aligned with S2 onset according to the first frame where sinus activation appears on the epicardial surface.

Comparing the F_{avg} traces in Figure 6.6A, the S1 activation is obviously slowest, with the traces of the weak, 1 V/cm shocks being significantly faster. F_{avg} for sinus activation falls in line with those for the 3 V/cm shocks, but has longer repolarization. The upstroke velocities of F_{avg} increase with increasing shock strength.

The activation dynamics immediately after shock onset for strong shocks are better viewed in Figure 6.6B. When the electric field is applied from right to left (cathode at LV), activation is immediate with shock onset for the 20, 25, and 30 V/cm F_{avg} traces. When the shock direction is reversed, hyperpolarization is evident after shock onset for those strong shocks. LV hyperpolarization is delaying whole heart activation at the strongest fields tested.

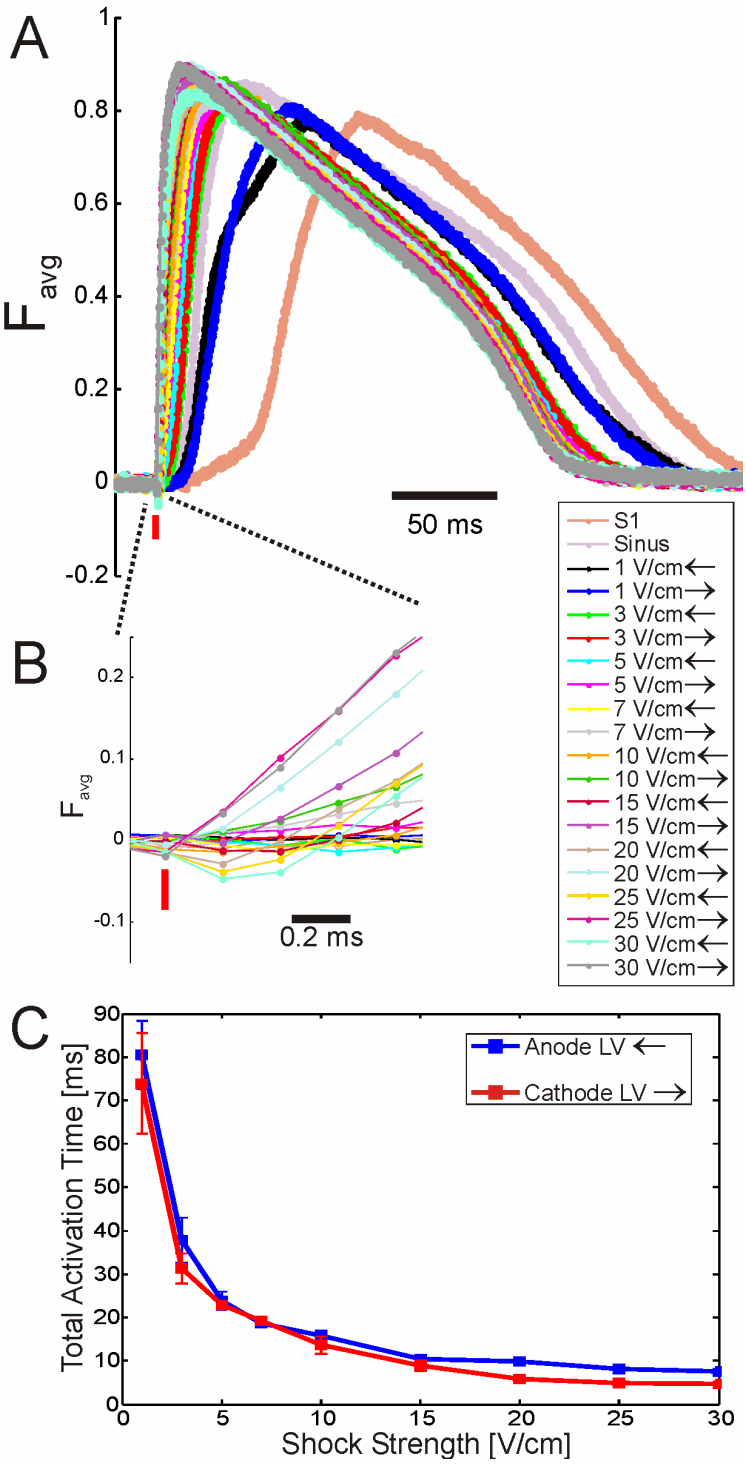

Figure 6.6. F_{avg} and total activation time as a function of shock strength and polarity. The shocks were 2 ms long. (A) F_{avg} from one heart. Red vertical line indicates shock onset. (B) Magnified view of *A* to show activation dynamics immediately after shock onset. (C) Total activation time from two hearts. Error bars represent standard error of the mean (n=2). Direction of the shock is indicated by the arrows: when the anode faces the LV, the direction is "←", and when the cathode faces the LV the direction is "→". Data acquired with the Redshirt camera (26×26 pixels at 5051 frames/sec).

Total AT for all ventricular pixels is graphed in Figure 6.6C as a function of shock strength and polarity. Total AT decreases rapidly with increasing shock strength from 1 to 5 V/cm, then continues decreasing at a much slower rate until 15 V/cm. To this point, shock polarity does not have a large effect. At 20 V/cm a difference in total AT between the two polarities becomes apparent: total AT is slower when the anode faces the LV, due to negative virtual electrode polarization of the LV. From 20 to 30 V/cm, total AT continues decreasing for both curves, but the changes are very small.

6.4.4. Analysis of Right Ventricle and Left Ventricle Regions

Because the RV and LV respond differently depending on shock polarity, we analyzed total AT for selected regions corresponding to each chamber. Figure 6.7 shows the total AT for RV and LV regions of interest as a function of shock strength and polarity. AT maps for the whole heart are shown as insets for the 3, 10, and 20 V/cm shocks. The RV and LV regions of interest are indicated on these maps with white rectangles.

Total AT generally decreases with increasing shock strength in both regions of interest. At the weak 3 V/cm strength activation is slow, the polarity of the shock does not have a large effect on the AT maps, and RV activation (squares, Figure 6.7) is slower than LV activation (triangles). At 10 V/cm activation is much faster, and the polarity of the shock affects the AT maps. When the anode faces the LV, activation of the LV is delayed by hyperpolarization, and activation of the RV is faster. When the cathode faces the LV, the LV activates quickly, and delayed activation is noted in the septal region. At strong shocks ($\geq$ 20 V/cm) activation of the regions of interest is very fast, except for the LV when it faces the anode (blue triangles). In that configuration, strong

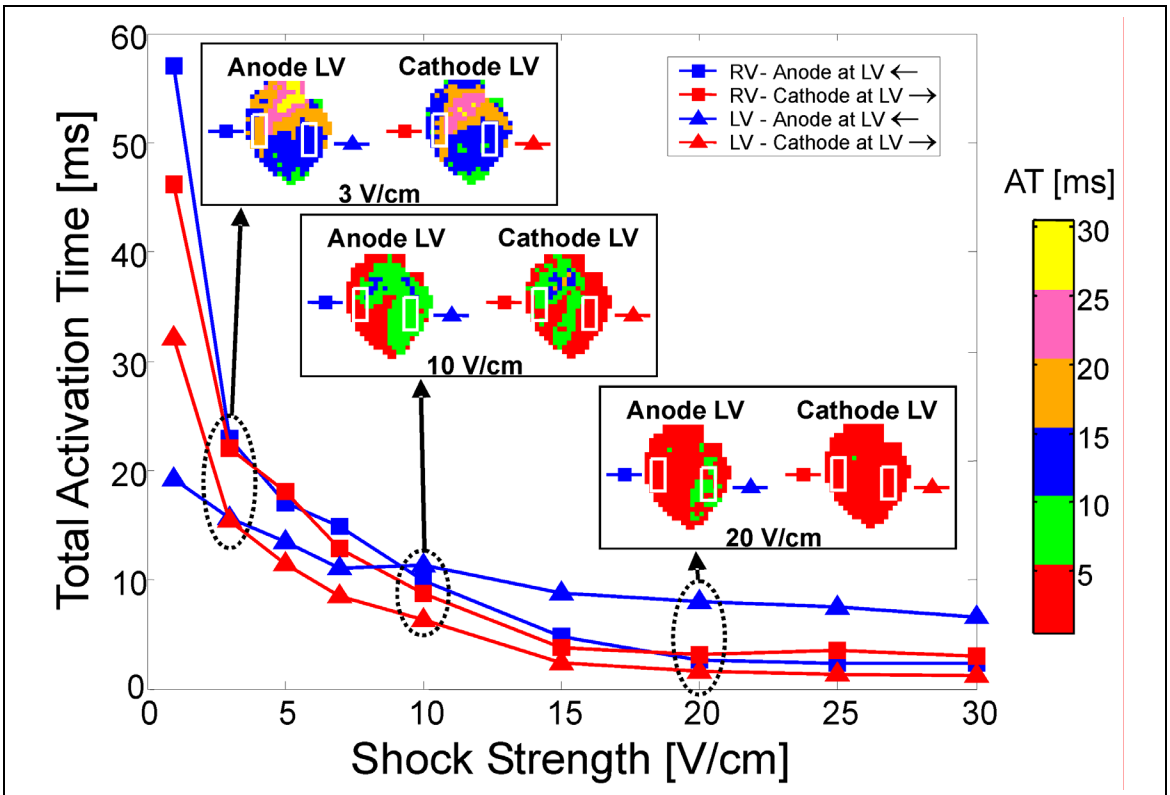

Figure 6.7. Total activation time of RV and LV regions of interest as a function of shock strength and polarity. The shock duration was 2 ms. Whole heart AT maps for 3, 10, and 20 V/cm are shown in the insets. The RV and LV regions of interest are indicated by the white rectangles on the maps. Data were collected with the Redshirt camera (26x26 pixels at 5051 fps).

hyperpolarization of the LV delays activation of the region, as is seen in the inset of activation time maps for 20 V/cm. When the cathode is at the LV, the whole heart is activated in less than 5 ms for shocks of 20 V/cm or stronger. At strong shock strengths, activation is much faster than would be expected from propagation.

6.5. Results: Role of Shock Duration

We examined the role of shock duration using strong shocks of 50 V/cm. Shock durations of 0.1 to 8 ms were tested. Atrial pixels and pixels at the base of the heart between the atria were digitally removed from the data prior to analysis and presentation.

6.5.1. Response to Short Duration Shocks

Figure 6.8 shows the response to 50 V/cm stimulation of 0.2 ms duration. Hyperpolarization of the side of the heart facing the anode is observed at shock onset for both shock polarities. Depolarization of the chamber facing the cathode is observed in the second frame of the shock (0.2-ms frame). RV hyperpolarization soon ends after S2 termination, with the whole heart activated by the 0.8-ms frame of Figure 6.8B. LV hyperpolarization lasts slightly longer, with the whole heart excited 1.4 ms after shock onset (Figure 6.8A). For both polarities, the chamber facing the cathode first activates more strongly (yellow color), further confirming the left/right differences in activation.

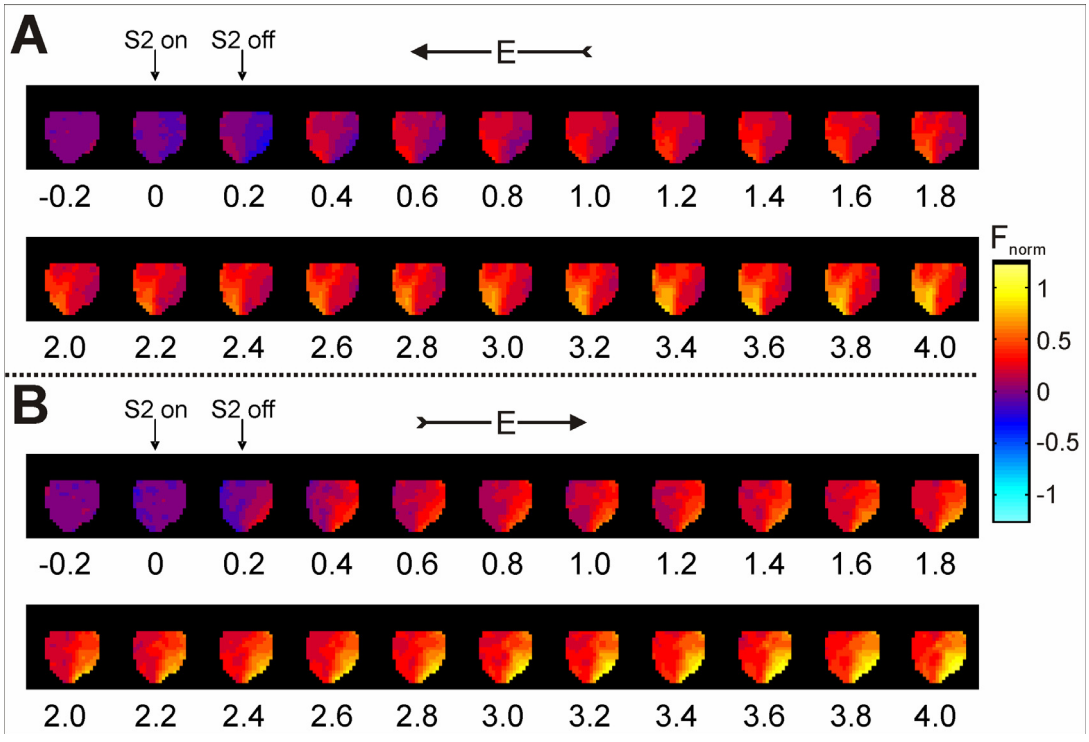

Figure 6.8. Response to strong field stimulation of short duration. This figure shows the spatiotemporal response of one heart to 50 V/cm field stimulation of 0.2 ms duration. In (A) the electric field is applied from right to left and in (B) the field is applied from left to right. The numbers below frame indicate the time [ms] since shock onset. Images were acquired with the Redshirt CCD camera (26×26 pixels at 5051 frames/sec).

6.5.2. Response to Long Duration Shocks

Figure 6.9 shows the first 4 ms of the whole heart response to 50 V/cm stimulation of 8 ms duration. Strong hyperpolarization of the LV is observed 0.2 ms into the shock (Figure 6.9A), and strong RV hyperpolarization occurs at the 0.4-ms mark (Figure 6.9B). The last region of RV hyperpolarization is noted near the apex 1.8 ms into the shock in Figure 6.9B, indicating that activation has overrun the shock. LV hyperpolarization is longer, with the last region occurring near the apex 2.6 ms after the onset of the shock (Figure 6.9A).

The V_m response to 8-ms stimulation is much stronger and faster than the response to 0.2-ms stimulation shown in Figure 6.8. In Figure 6.9 the left/right

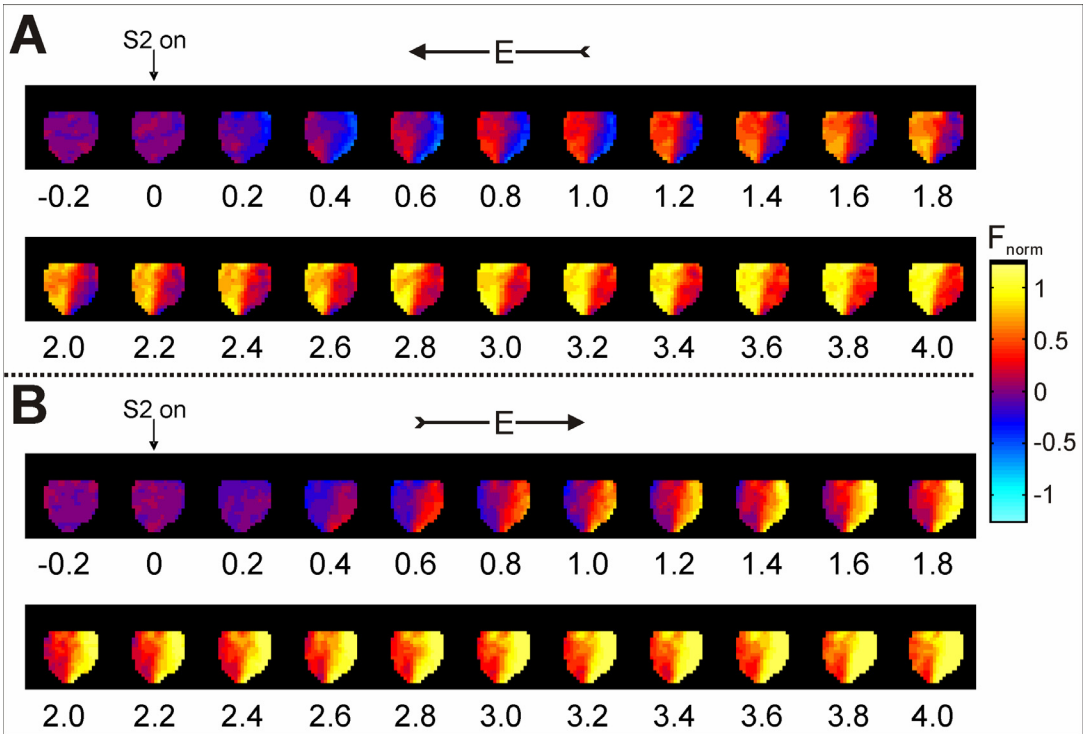

Figure 6.9. Response to strong field stimulation of long duration. This figure shows the spatiotemporal response of one heart to 50 V/cm field stimulation of 8 ms duration. In (A) the electric field is applied from right to left and in (B) the field is applied from left to right. The numbers below frame indicate the time [ms] since shock onset. The upper limit of the color scale is saturated. Images were acquired with the Redshirt CCD camera (26×26 pixels at 5051 frames/sec).

hyperpolarization/depolarization (blue/red colors) dichotomy between the chambers dependent on the field direction is much more pronounced. Peak activation (yellow color) of the entire half of the facing the cathode is very obvious in the 4.0-ms frames of Figure 6.9, whereas in Figure 6.8 only a fraction of the heart was maximally activated 4 ms after shock onset.

6.5.3. Analysis of Shock Duration

Whole heart activation dynamics as a function of shock duration is shown in Figure 6.10. In Figure 6.10A F_{avg} for each shock duration and polarity is plotted. Note that the peak F_{avg} for each curve is greater than 1. This means that the very strong 50 V/cm shock caused a much stronger and faster response than the S1 pacing stimulus by which the fluorescence data was normalized. In this graph we see that the shortest shocks (0.1 ms) exhibit delayed upstroke velocities in comparison with the other curves. Hyperpolarization with shock onset is also visible in some curves.

Figure 6.10B is a magnified view to show better the response after shock onset. Hyperpolarization after shock onset is noted in every curve except the 0.1 and 0.2 ms curves when the field is applied from left to right (cathode at LV). For these cases, RV hyperpolarization is of small magnitude and very transient (as noted Figure 6.8B), and therefore does not reveal itself in the F_{avg} computation for the whole heart. For all other shock durations and polarities, the shock-induced negative virtual electrode polarization is substantial enough to manifest in the whole heart activation dynamics. Activation for the 0.1-ms shocks is slowest, followed by the 0.2-ms duration. For the longest shock durations (3, 5 and 8 ms), strong LV hyperpolarization dominates in the F_{avg} traces when

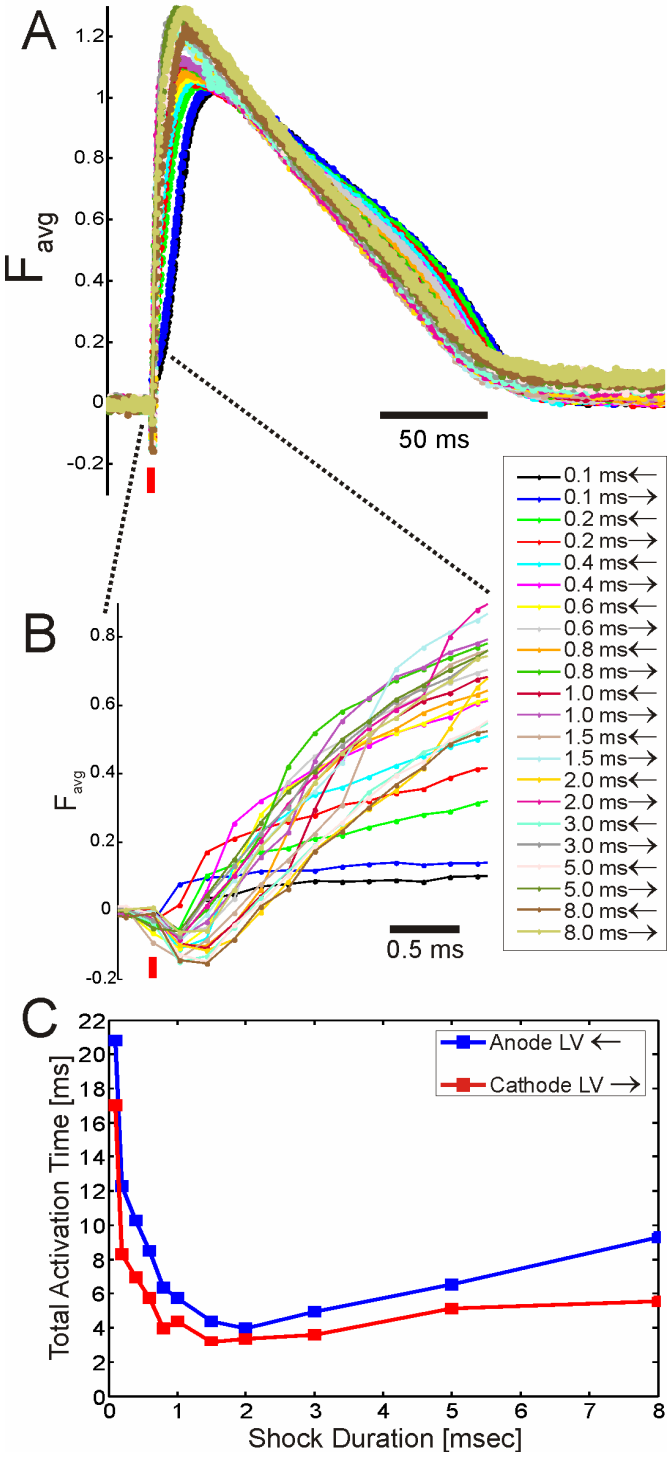

Figure 6.10. F_{avg} and total activation time as a function of shock duration and polarity. The shock strength was 50 V/cm. (A) F_{avg} for each shock duration and polarity. Red vertical line indicates shock onset. (B) Magnified view of *A* to show activation dynamics after shock onset. (C) Total activation time. Direction of the shock is indicated by the arrows: when the anode faces the LV, the direction is "←", and when the cathode faces the LV the direction is "→". Data acquired with the Redshirt camera (26×26 pixels at 5051 frames/sec).

the field is applied from left to right, resulting in a large decrease of F_{avg} after shock onset and delayed activation.

Total AT for each shock duration is graphed in Figure 6.10C according to shock polarity. Because of the strong 50 V/cm field, total AT decreases rapidly with increasing shock duration until 2.0 ms. For shock durations greater than 2.0 ms, total AT increases with increasing shock duration because of stronger hyperpolarization. Differences in total AT between the two polarities occur for all shock durations. The stronger LV hyperpolarization delays activation more than RV hyperpolarization; thus total AT is longer when the anode faces the LV.

6.5.4. Analysis of Right Ventricle and Left Ventricle Regions

As the two ventricular chambers activate differently depending on the field direction, we analyzed regions of interest corresponding to the RV and the LV. The results are shown in Figure 6.11. For shocks of 0.1 to 0.8 ms duration, total AT decreased rapidly with increasing shock duration in each region of interest. For shocks longer than 1.0 ms, there is little change in total AT for the RV when it faces the cathode (blue squares) and for the LV when it faces the cathode (red triangles). Activation of these regions is very rapid (< 2 ms), with the LV activating slightly faster than the RV. However, when the regions of interest face the anode, activation of the regions is slowed by hyperpolarization. When the RV faces the anode, total AT of the RV region (red squares) increases with increasing shock duration for shocks longer than 1.0 ms. When the LV faces the anode, LV total AT (blue triangles) plateaus for the 1.5 to 3.0-ms shocks, and then increases for the 5 and 8-ms durations.

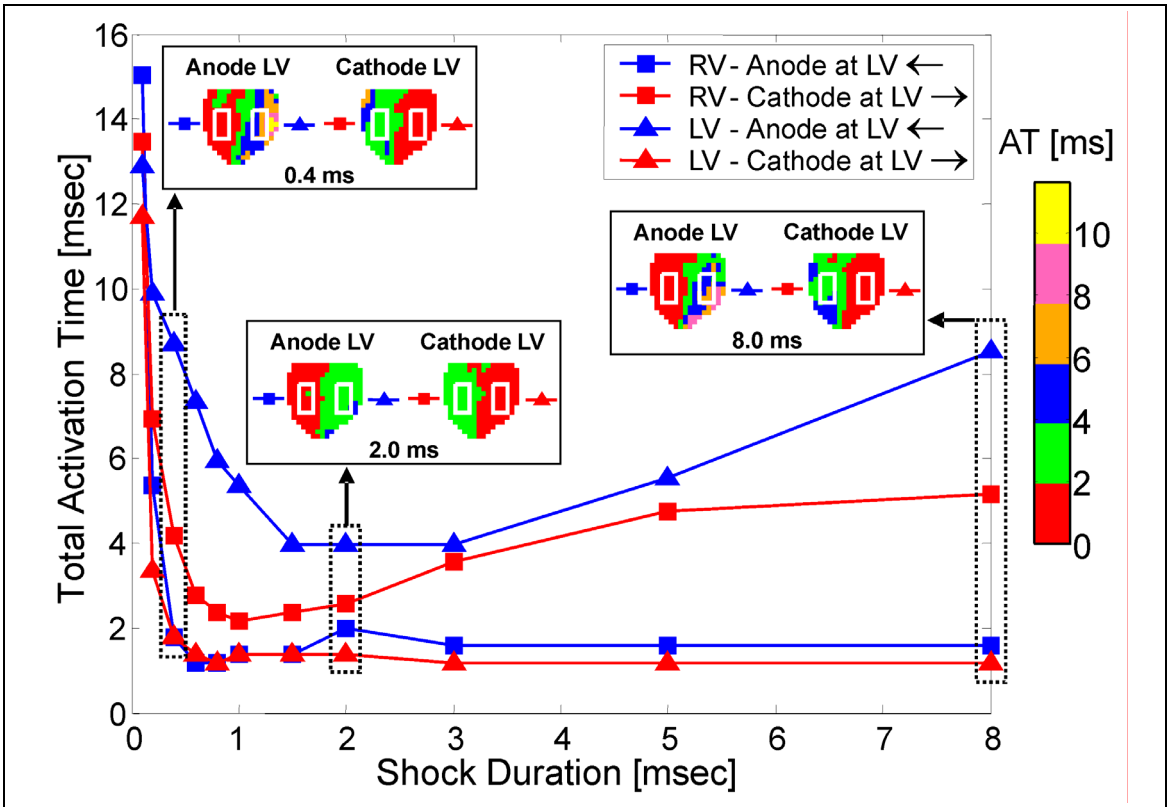

Figure 6.11. Total activation time of RV and LV regions of interest as a function of shock duration and polarity. The shock strength was 50 V/cm. Whole heart AT maps for 0.4, 2, and 8 ms are shown in the insets. The RV and LV regions of interest are depicted by the white rectangles on the maps. Images were collected with the Redshirt camera (26x26 pixels at 5051 fps).

To characterize further the differences in LV and RV activation depending on field polarity, F_{avg} was computed for the regions of interest indicated in Figure 6.11. These F_{avg} traces, shown in Figure 6.12, depict activation during and immediately after the shocks and clearly illustrate dramatically different activation dynamics of the RV and LV as a function of the field direction. In this figure, the traces were aligned according to shock termination in order to see better the effects of the different shock durations.

In Figure 6.12A the electric field was applied from left to right such that the cathode faced the RV and the anode faced the LV. F_{avg} traces for the RV region reveal slow activation for the 0.1 and 0.2-ms durations, but for all longer durations activation is very rapid beginning at the onset of the shock. Dominant negative virtual electrode

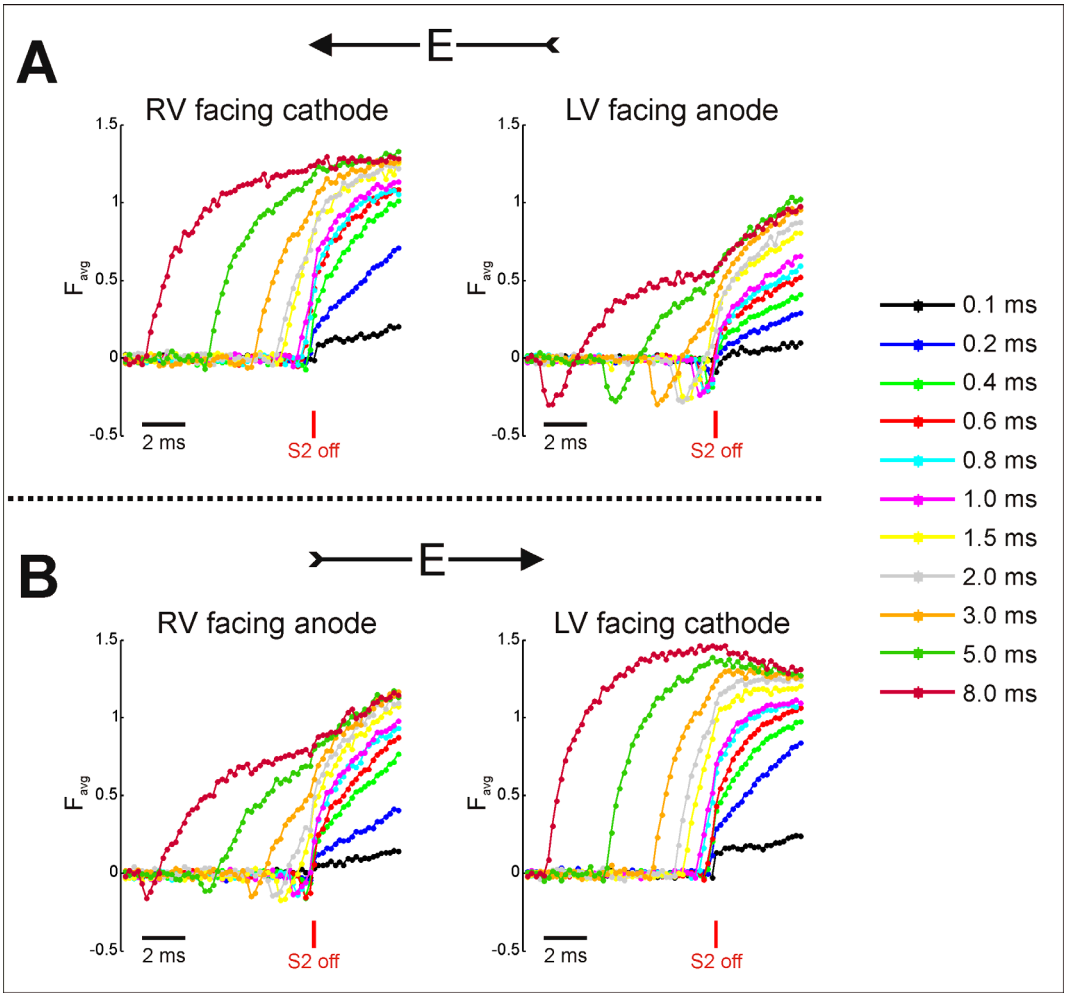

Figure 6.12. F_{avg} for RV and LV regions of interest as a function of shock duration and polarity. The shock strength was 50 V/cm. Vertical red lines indicate the termination of the shock. The time scale was chosen to show activation dynamics during and immediately after the shocks. Left column: F_{avg} for the RV region. Right column: F_{avg} for LV region. In (A) the electric field was applied from right to left (anode at LV). In (B) the electric field was applied from left to right (cathode at LV). Data were acquired with the Redshirt camera (26x26 pixels at 5051 fps).

polarization is obvious in the LV F_{avg} traces, especially at the longest durations. Activation of the LV is much slower in comparison with the RV. The LV F_{avg} traces for the 5 and 8-ms durations exhibit four phases of behavior. The first phase is negative polarization with shock onset which is followed by a phase of fast depolarization. The third phase is slower depolarization to ≈0.5, with activation completed by a phase of increased upstroke velocity after shock termination. Negative polarization in the F_{avg}

traces lasted for approximately 1.6 ms for durations of 1.5 ms and greater; the increase in durations above 1.5 ms did not lengthen the time of negative $F_{avg.}$

In Figure 6.12B the electric field was applied from right to left such that the anode faced the RV and the cathode faced the LV. Negative polarization is observed in all of the RV traces; however, the magnitude of the hyperpolarization is smaller and activation is faster than was observed for the LV in Figure 6.12A. The RV F_{avg} traces for the 5 and 8-ms durations exhibit less prominent four-phase behavior that was described for the LV in Figure 6.12A. For the RV, the negative polarization is shorter (≈1 ms) for shock durations of 1.5 ms and greater. F_{avg} traces for the LV region reveal slow activation for the 0.1 and 0.2 ms durations, but activation is extremely rapid for all longer shock durations. The maximum F_{avg}. for the LV increases with increasing duration, and activation is stronger and faster than for the RV when it faced the cathode (Figure 6.12A). For the 0.1-ms duration, F_{avg} increases rapidly for one frame (0.2 ms) at shock onset, and then much slower activation follows when the chamber faces the cathode (RV in Figure 6.12A and LV in Figure 6.12B, black traces). The brief period of positive polarization in response to an extremely short shock may reflect membrane charging.

6.6. Discussion

We find that the chamber that faces the cathode activates first and more strongly; the chamber facing the anode exhibits slower activation. Negative virtual electrode polarization delays activation. The LV hyperpolarizes at lower shock strengths than the RV. The magnitude and duration of LV hyperpolarization is larger than that observed for the RV.

Many of the experimental results presented are in good agreement with numerical predictions of an anatomically accurate 3D bidomain model of the rabbit ventricles which includes the bidomain anisotropy required for realistic modeling of shock response (M.M. Maleckar, personal communication, 2005). Maleckar and Trayanova [17] reported an increase in negative shock-induced V_m predominantly in the septum and LV free wall with increasing field strength, causing paradoxical increase in AT for stronger shocks. These results qualitatively agree with our experimental results in which field stimulation of strong strength and long duration (50 V/cm; 3, 5, and 8 ms) increased total AT due to negative virtual electrode polarization (Figure 6.10C and Figure 6.11). These results also agree with others who found shock-induced delayed activation from hyperpolarization in LV wedge preparations [14,18] and cell strands [18].

One discrepancy of note between experiment and theory is the experimental absence of obvious RV hyperpolarization at shock strengths less than 20 V/cm. Numerical simulations predict negative virtual electrode polarization of the RV should occur. The discrepancy may be due to modeling error, *i.e.* inaccurate membrane model, or may be due to experimental limitations. The bath may be masking virtual electrode polarization [10,11]. Additionally, when the chamber faces the anode, bidomain theory predicts negative polarization of the epicardial surface and positive polarization of the endocardial surface [4-6]. Transmural fiber rotation for both the LV and RV is counterclockwise from the epicardial to endocardial surface with a rotation angle of approximately 120˚ [19,20]. As the RV is much thinner than the LV, RV transmural fiber rotation is faster. In addition, optical recordings from the epicardial surface are actually weighted averages of fluorescence from a tissue depth that is estimated to be 300-500 μm

[21,22] or as much as 1-2 mm [23-26]. The combination of fiber rotation and fluorescence averaging over depth could blur epicardial and transmural virtual electrode polarization patterns, resulting in smaller recordings of shock-induced hyperpolarization for the thinner RV than actually occur. In the LV, this is less of a problem because transmural rotation is slower through the thicker wall. We do observe some hyperpolarization at the RV edge near the right atrium and the RV near the apex for 20-30 V/cm shocks (Figure 6.3B, Figure 6.4B, and Figure 6.5). The fact that these locations correspond to thicker regions supports the above hypothesis.

For very strong and very long field stimulation, F_{avg} traces in hyperpolarized regions (LV in Figure 6.12A and RV in Figure 6.12B) revealed four phases of behavior: initial hyperpolarization at shock onset, rapid depolarization, slow depolarization, and fast depolarization after shock termination. This morphology is similar to the triphasic morphology observed in transmural field stimulation of porcine LV preparations [14]. Our latter three phases correspond to their three phases: the authors report a lack of hyperpolarization during diastolic field stimulation. However, careful examination of one of the curves in their article (Figure 4C, top trace) reveals transient hyperpolarization of small magnitude at shock onset [16] in response to diastolic stimulation of 38 V/cm for 10 ms. This disagrees with our results; we observed prominent negative virtual electrode polarization for shocks with these approximate parameters.

Nevertheless, in their study Sharifov and Fast [14] hypothesized that the complex upstrokes resulted from electrotonic interaction and spatial averaging of virtual electrode polarization at microscopic heterogeneities. Activation is very rapid at virtual cathode while, at virtual anodes, negative polarization can occur for the duration of the shock.

Spatial averaging by the imaging modality of adjacent virtual cathodes and anodes would measure multi-phasic upstrokes. They also noted that the phase of slow depolarization during the shock was paralleled by the occurrence of elevation of diastolic V_m after the shock. Indeed, close examination of the F_{avg} traces in Figure 6.10A reveals elevation of the resting potential after the shock, most notably for the 8-ms duration. Elevation of resting V_m is believed to be a signature of membrane electroporation [24,27]. Therefore multi-phasic upstrokes with the morphology described above may be another indicator of electroporation.

6.7. Conclusions

In conclusion, the goals of this study were to characterize the effects of diastolic field stimulation of the isolated whole heart as a function of shock strength, duration, and polarity. Temporal activation analyses indicate that increasing shock strength and duration do not necessarily result in faster activation, and that negative virtual electrode polarization must be considered when applying field stimulation to diastolic tissue.

6.8. Acknowledgements

This work was supported by the National Institutes of Health (R01-HL58241-05), the American Heart Association (0215128B), and the Academic Venture Capital Fund of Vanderbilt University.

6.9. References

[1] Plonsey, R. and Barr, R. C., "Effect of microscopic and macroscopic discontinuities on the response of cardiac tissue to defibrillating (stimulating) currents." *Med Biol Eng Comput*, vol. 24, no. 2, pp. 130-136, 1986.

[2] Gillis, A. M., Fast, V. G., Rohr, S., and Kleber, A. G., "Spatial changes in transmembrane potential during extracellular electrical shocks in cultured

monolayers of neonatal rat ventricular myocytes." *Circ Res*, vol. 79, no. 4, pp. 676-690, 1996.

[3] Zhou, X., Knisley, S. B., Smith, W. M., Rollins, D., Pollard, A. E., and Ideker, R. E., "Spatial changes in the transmembrane potential during extracellular electric stimulation." *Circ Res*, vol. 83, no. 10, pp. 1003-1014, 1998.

[4] Efimov, I. R., Aguel, F., Cheng, Y., Wollenzier, B., and Trayanova, N., "Virtual electrode polarization in the far field: implications for external defibrillation." *Am J Physiol Heart Circ Physiol*, vol. 279, no. 3, pp. H1055-H1070, 2000.

[5] Entcheva, E., Trayanova, N. A., and Claydon, F. J., "Patterns of and mechanisms for shock-induced polarization in the heart: A bidomain analysis." *IEEE Trans Biomed Eng*, vol. 46, no. 3, pp. 260-270, 1999.

[6] Trayanova, N. A., Roth, B. J., and Malden, L. J., "The response of a spherical heart to a uniform electric field: a bidomain analysis of cardiac stimulation." *IEEE Trans Biomed Eng*, vol. 40, no. 9, pp. 899-908, 1993.

[7] Fishler, M. G., "Syncytial heterogeneity as a mechanism underlying cardiac far-field stimulation during defibrillation-level shocks." *J Cardiovasc Electrophysiol*, vol. 9, no. 4, pp. 384-394, 1998.

[8] Krassowska, W. and Kumar, M. S., "The role of spatial interactions in creating the dispersion of transmembrane potential by premature electric shocks." *Ann Biomed Eng*, vol. 25, no. 6, pp. 949-963, 1997.

[9] Hooks, D. A., Tomlinson, K. A., Marsden, J. E., LeGrice, I. J., Smaill, B. H., Pullan, A. J., and Hunter, P. J., "Cardiac microstructure: implications for electrical propagation and defibrillation in the heart." *Circ Res*, vol. 91, no. 4, pp. 331-338, 2002.

[10] Latimer, D. C. and Roth, B. J., "Effect of a bath on the epicardial transmembrane potential during internal defibrillation shocks." *IEEE Trans Biomed Eng*, vol. 46, no. 5, pp. 612-614, 1999.

[11] Entcheva, E., Eason, J., Efimov, I. R., Cheng, Y., Malkin, R., and Claydon, F., "Virtual electrode effects in transvenous defibrillation-modulation by structure and interface: Evidence from bidomain simulations and optical mapping." *J Cardiovasc Electrophysiol*, vol. 9, no. 9, pp. 949-961, 1998.

[12] Fast, V. G., Sharifov, O. F., Cheek, E. R., Newton, J. C., and Ideker, R. E., "Intramural virtual electrodes during defibrillation shocks in left ventricular wall assessed by optical mapping of membrane potential." *Circulation*, vol. 106, no. 8, pp. 1007-1014, 2002.

[13] Knisley, S. B., Trayanova, N., and Aguel, F., "Roles of electric field and fiber structure in cardiac electric stimulation." *Biophys J*, vol. 77, no. 9, pp. 1404-1417, 1999.

[14] Sharifov, O. F. and Fast, V. G., "Optical mapping of transmural activation induced by electrical shocks in isolated left ventricular wall wedge preparations." *J Cardiovasc Electrophysiol*, vol. 14, no. 11, pp. 1215-1222, 2003.

[15] Roth, B. J., Patel, S. G., and Murdick, R. A., "The effect of the cut surface during electrical stimulation of a cardiac wedge preparation." *IEEE Trans Biomed Eng*, *in press*, 2005.

[16] Efimov, I. R. and Nikolski, V. P., "Diastolic shocking experience: Do virtual electrodes exist only during systole?" *J Cardiovasc Electrophysiol*, vol. 14, no. 11, pp. 1223-1224, 2003.

[17] Maleckar, M. M. and Trayanova, N. A., "Negative VEP affects activation during diastolic stimulation in the rabbit ventricles." *Heart Rhythm*, vol. 1, no. 1, pp. S225, 2004.

[18] Cheek, E. R., Sharifov, O. F., and Fast, V. G., "Role of microscopic tissue structure in shock-induced activation assessed by optical mapping in myocyte cultures." *J Cardiovasc Electrophysiol*, vol. 16, no. 9, pp. 991-1000, 2005.

[19] Streeter, D. D., Spotnitz, H. M., Patel, D. P., Ross, J., Jr., and Sonnenblick, E. H., "Fiber orientation in the canine left ventricle during diastole and systole." *Circ Res*, vol. 24, no. 3, pp. 339-347, 1969.

[20] Streeter, D. D., "Gross morphology and fiber geometry of the heart." in Berne, R. M., Sperelakis, N., and Geiger, S. R. (eds.) *Handbook of Physiology* Bethesda, MD: American Physiological Society, 1979, pp. 61-112.

[21] Knisley, S. B., "Transmembrane voltage changes during unipolar stimulation of rabbit ventricle." *Circ Res*, vol. 77, no. 6, pp. 1229-1239, 1995.

[22] Girouard, S. D., Laurita, K. R., and Rosenbaum, D. S., "Unique properties of cardiac action potentials recorded with voltage-sensitive dyes." *J Cardiovasc Electrophysiol*, vol. 7, no. 11, pp. 1024-1038, 1996.

[23] Efimov, I. R., Sidorov, V., Cheng, Y., and Wollenzier, B., "Evidence of three-dimensional scroll waves with ribbon-shaped filament as a mechanism of ventricular tachycardia in the isolated rabbit heart." *J Cardiovasc Electrophysiol*, vol. 10, no. 11, pp. 1452-1462, 1999.

[24] Al-Khadra, A., Nikolski, V., and Efimov, I. R., "The role of electroporation in defibrillation." *Circ Res*, vol. 87, no. 9, pp. 797-804, 2000.

[25] Baxter, W. T., Mironov, S. F., Zaitsev, A. V., Jalife, J., and Pertsov, A. M., "Visualizing excitation waves inside cardiac muscle using transillumination." *Biophys J*, vol. 80, no. 1, pp. 516-530, 2001.

[26] Ding, L., Splinter, R., and Knisley, S. B., "Quantifying spatial localization of optical mapping using Monte Carlo simulations." *IEEE Trans Biomed Eng*, vol. 48, no. 10, pp. 1098-1107, 2001.

[27] Neunlist, M. and Tung, L., "Dose-dependent reduction of cardiac transmembrane potential by high-intensity electrical shocks." *Am J Physiol*, vol. 273, no. 6 Pt 2, pp. H2817-H2825, 1997.

CHAPTER VII

VIRTUAL ELECTRODE EFFECTS AROUND AN ARTIFICIAL HETEROGENEITY DURING FIELD STIMULATION OF CARDIAC TISSUE

Marcella C. Woods[1], Veniamin Y. Sidorov[1,2,3],

Mark R. Holcomb[2], Deborah Langrill Beaudoin[5],

Bradley J. Roth[6], John P. Wikswo[1,2,3,4]

[1]Department of Biomedical Engineering

[2]Department of Physics and Astronomy

[3]Vanderbilt Institute for Integrative Biosystems Research and Education

[4]Department of Molecular Physiology and Biophysics

Vanderbilt University, Nashville, Tennessee

[5]Department of Ophthalmology and Visual Sciences

University of Michigan, Ann Arbor, Michigan

[6]Department of Physics

Oakland University, Rochester, Michigan

Portions of this manuscript have been published in:

MC Woods, VY Sidorov, MR Holcomb, D Langrill Beaudoin, BJ Roth, JP Wikswo. *Heart Rhythm*, in press, 2006.

7.1. Abstract

The response of cardiac tissue to strong electric fields is determined by 3-D cable properties, bidomain anisotropy, nonlinearities, and, most importantly, heterogeneities. Langrill Beaudoin and Roth [1,2] numerically studied the effect of a plunge electrode and found alternating regions of hyperpolarization and depolarization around the electrode in response to field shock. We sought to verify experimentally their results by using field stimulation and optical imaging of di-4-ANEPPS stained rabbit hearts with a pulled glass micropipette serving as the heterogeneity. There is good agreement between the experimental and numerical results. Because adjacent regions of opposite polarization are potential sources of wave front generation, our results suggest that plunge electrodes or similar-sized heterogeneities may play a role in far-field stimulation.

7.2. Introduction

The effects of defibrillation-strength electric fields on the heart have been the subject of numerous experimental studies. In the context of the bidomain theory of cardiac tissue, heterogeneities cause regions of positive and negative polarization when exposed to an externally applied electric field. Researchers often use insulated plunge electrodes to record the extracellular potential within the ventricular walls [3,4]. While these plunge electrodes had been thought to have little impact upon the electrical activity of the heart, these electrodes are essentially artificially added myocardial heterogeneities within the cardiac bidomain. Recent bidomain calculations by Langrill Beaudoin and Roth [1,2] predict alternating areas of positive and negative polarization around an insulated heterogeneity. The purpose of this study was to verify experimentally the results of their numerical simulations. The predicted adjacent areas of opposite polarity

are potential sources of wave front generation, a hypothesized mechanism for far-field stimulation, could contribute to arrhythmogenesis, and could lead to errors in mapping shock distributions.

7.3. Methods

All experiments conformed to the National Institutes of Health guidelines for the ethical use of animals in research and were pre-approved by the Vanderbilt Institutional Animal Care and Use Committee.

7.3.1. Experimental Set Up

Here we present the effects of a heterogeneity during field stimulation of cardiac tissue. A pulled glass micropipette (1.5-mm diameter) was pushed through the anterior left ventricle of a Langendorff-perfused rabbit heart in a warmed bath of Tyrode's solution with titanium plates at each end for field stimulation. The heart was mounted on a custom-built glass goniometer to allow rotation of the fiber direction (FD) in the area of the heterogeneity with respect to the field direction. The heart was secured to the goniometer by two sutures: one near the apex and one through the posterior heart, carefully avoiding major vessels. The experimental set up is shown schematically in Figure 7.1.

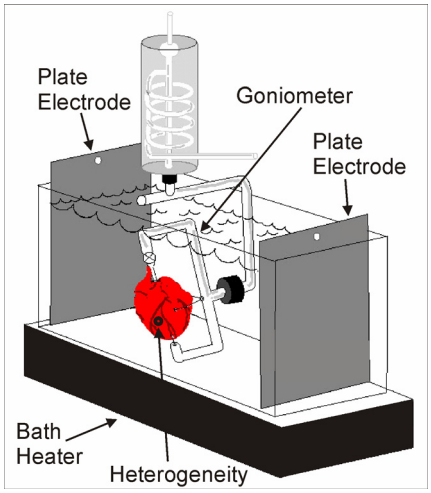

Figure 7.1. Experimental set up of isolated heart mounted on a goniometer. This figure shows the isolated rabbit heart mounted on a goniometer to allow rotation of the heart with respect to the electric field. The heart is in a warmed bath of Tyrode's solution. Titanium plate electrodes are positioned at the ends of the bath for delivery of field shocks. A pulled glass micropipette through the anterior left ventricle serves as the heterogeneity.

7.3.2. Optical Imaging

The heart was stained with the voltage-sensitive dye, di-4-ANEPPS, and a CCD camera (Redshirt Imaging, Decatur, GA; 80×80 pixels, 1000 frames/sec) was positioned to image the 8×8 mm^2 area around the heterogeneity. The tissue was illuminated by a diode-pumped, solid-state 532 nm laser (Verdi, Coherent, Santa Clara, CA). The emitted light was passed through a cutoff filter (no. 25 Red, 607 nm, Tiffen, Japan). To reduce motion artifacts in the acquired data, the excitation-contraction uncoupler diacetyl monoxime (DAM, Sigma-Aldrich, St. Louis, MO) was added to the Tyrode's solution at a concentration of 15-20 mmol/L.

7.3.3. Stimulation Protocol

Apical pacing stimuli (S1; 4 ms duration, 1.5× threshold) were delivered every 300 ms via an insulated bipolar electrode. Field shocks (S2), supplied by a computer-controlled custom voltage source (Ventritex,Sunnyvale, CA), of 3 ms duration and 30 V/cm strength were applied either to systolic tissue at an S1-S2 coupling interval of 85 ms or diastolic tissue at an S1-S2 coupling interval of 300 ms. Shocks of both polarities were examined with FD parallel and perpendicular to the field. Each shock configuration was tested twice; data from both acquisitions were summed and then spatially filtered (5×5 Gaussian) and normalized according to the pacing S1 response, assuming a resting transmembrane potential (V_m) of -85 mV and an action potential amplitude of 112 mV [5].

7.3.4. Numerical Simulations

For comparison with the experimental data, the bidomain model was used to predict the effects of a 1.6-mm diameter heterogeneity in a 2-D sheet of cardiac tissue to

5 V/cm stimulation. The simulations used a linear membrane model; thus the numerical results are the same for systolic and diastolic field shocks. Therefore the theoretical data is not replicated in the figures showing the experimental diastolic field stimulation data.

7.4. Results and Discussion

7.4.1. V_m response to systolic field stimulation

The experimental images of systolic field stimulation show the shock-induced ΔV_m during the second-ms of the 3 ms stimuli. The images were obtained by subtracting the frame acquired just before the shock. Figure 7.2 shows the response to both polarities with FD parallel to the field. Alternating regions of positive and negative virtual electrode polarization (VEP) occur around the heterogeneity. When the polarity is reversed, the

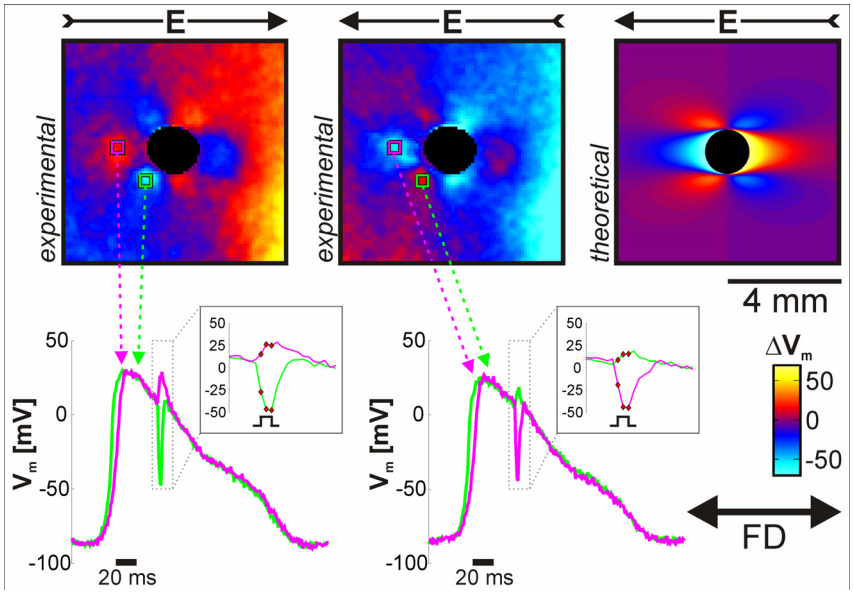

Figure 7.2. Virtual electrode polarization around an artificial heterogeneity during systolic field stimulation with fiber direction parallel to the electric field. Field shocks of 30 V/cm strength were applied for 3 ms during the plateau phase (S1-S2 coupling interval of 85 ms). Images of the shock-induced change in transmembrane potential (ΔV_m) are shown for both shock polarities; the frames correspond to the second-ms of the shock. Temporal traces for the areas indicated by the magenta and green squares are depicted below the images. Insets of the traces reveal the shock response in more detail. Red diamonds indicate the interval of S2 application.

VEP pattern reverses. There is excellent qualitative agreement between the experimental and theoretical images. Time traces for the regions indicated by the magenta and green squares reveal the timing of the field shocks with respect to the pacing response. The insets show in more detail the temporal shock response; the red diamonds indicate the interval during which the S2 shock was delivered. Fast negative VEP with shock onset is observed, along with positive VEP of smaller magnitude. Stimulation in the plateau phase is known to produce larger negative changes in V_m than positive ones [6-8]. The L-type calcium current has been hypothesized to underlie this nonlinearity in systolic V_m response [9]. The temporal traces also reveal the reversal of ΔV_m with polarity. When the field is applied from left to right with parallel FD, the largest $\pm\Delta V_m$ in the virtual electrodes around the heterogeneity are -64 mV and +29 mV. For the opposite polarity, they are -68 mV and +18 mV.

Figure 7.3 shows ΔV_m for systolic shocks when FD is perpendicular to the field. The 90° change in FD reverses the pattern of VEP and generally decreases the magnitude of ΔV_m. The maximum $\pm\Delta V_m$ are -51 mV and +20 mV with the cathode to the right, and -28 mV and +30 mV for the opposite polarity. Again the experimental polarization pattern correlates well with the theoretical prediction.

7.4.2. V_m response to diastolic field stimulation

The experimental images of diastolic field stimulation show the shock-induced ΔV_m during the first-ms of the 3 ms stimuli. Figure 7.4 shows the response to diastolic field stimulation when the FD is parallel with the electric field. The pattern of VEP around the heterogeneity resembles that of the parallel FD data for systolic field stimulation in Figure 7.2, but with positive VEP more prominent. Again, with field

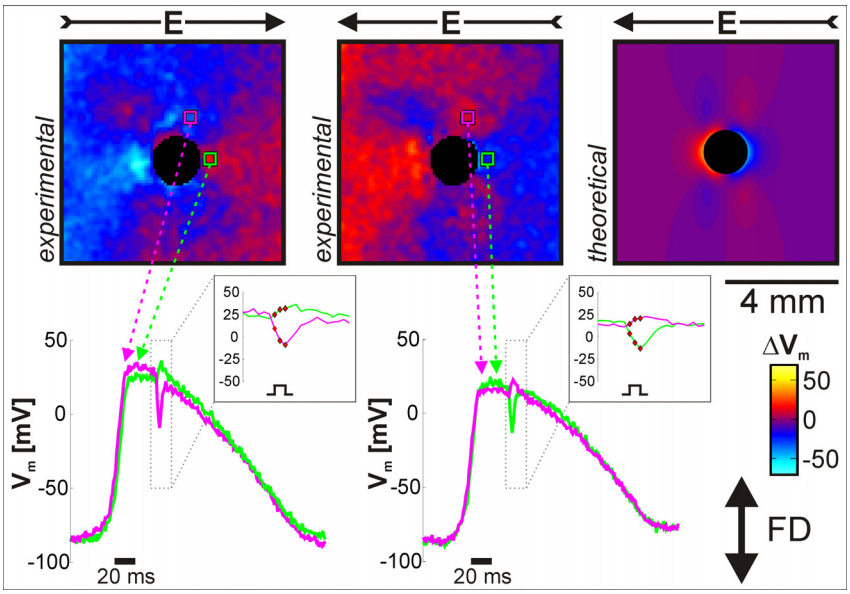

Figure 7.3. Virtual electrode polarization around an artificial heterogeneity during systolic field stimulation with fiber direction perpendicular to the electric field. Field shocks of 30 V/cm strength were applied for 3 ms during the plateau phase (S1-S2 coupling interval of 85 ms). Images of the shock-induced change in transmembrane potential (ΔV_m) are shown for both shock polarities; the frames correspond to the second-ms of the shock. Temporal traces for the areas indicated by the magenta and green squares are depicted below the images. Insets of the traces reveal the shock response in more detail. Red diamonds indicate the interval of S2 application.

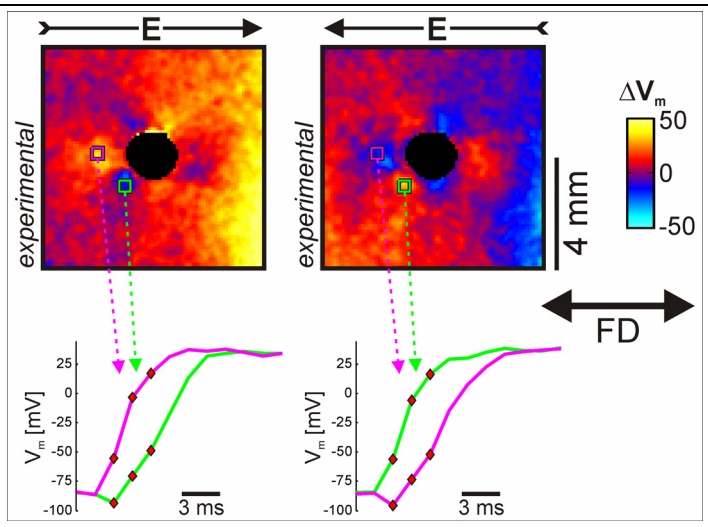

Figure 7.4. Virtual electrode polarization around an artificial heterogeneity during diastolic field stimulation with fiber direction parallel to the electric field. Field shocks of 30 V/cm strength were applied for 3 ms to resting tissue (S1-S2 coupling interval of 300 ms). Images of the shock-induced change in transmembrane potential (ΔV_m) are shown for both shock polarities; the frames correspond to the first-ms of the shock. Temporal traces for the areas indicated by the magenta and green squares are depicted below the images. Red diamonds indicate the interval of S2 application.

direction reversal, the spatial pattern of polarization reverses as well for diastolic stimulation. The temporal traces show the activation dynamics in the green and magenta regions after the shock; the red diamonds indicate S2 shock timing. The traces reveal fast depolarization with onset of the shock in the positive VEP regions. In the negative VEP regions, hyperpolarization of smaller magnitude occurs at the shock onset, but lasts only 1 ms. Depolarization of the negative VEP regions occurs during the second and third-ms of the field shock. For diastolic stimulation, activation of the positive VEP areas is faster than that in the negative regions VEP. Hyperpolarization in the negative VEP regions delays activation.

Figure 7.5 shows the diastolic shock-induced Vm response with the FD perpendicular to the electric field. The 90° rotation of the FD causes the spatial pattern of VEP to almost disappear. However, when comparing the shock-induced ΔV_m images, one

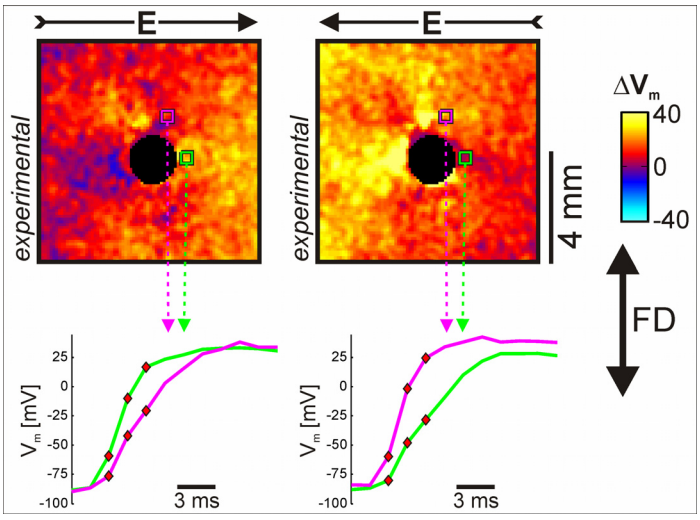

Figure 7.5. Virtual electrode polarization around an artificial heterogeneity during diastolic field stimulation with fiber direction perpendicular to the electric field. Field shocks of 30 V/cm strength were applied for 3 ms to resting tissue (S1-S2 coupling interval of 300 ms). Images of the shock-induced change in transmembrane potential (ΔV_m) are shown for both shock polarities; the frames correspond to the first-ms of the shock. Temporal traces for the areas indicated by the magenta and green squares are depicted below the images. Red diamonds indicate the interval of S2 application.

can see reversal of the pattern of the areas of strongest change (yellow color) when the electric field is reversed. The temporal traces, indeed, reveal different activation dynamics for different regions around the heterogeneity. Though no hyperpolarization is detected in the traces, delayed activation is observed. When the field direction reverses, the activation in the region is faster. Thus, while the spatial pattern of VEP is not readily visible, there are areas of faster and slower activation dynamics around the heterogeneity when FD is perpendicular to the field.

7.4.3. V_m response to systolic field stimulation around a very small heterogeneity

In another experiment we observed VEP around very small artificial myocardial heterogeneities, comparable to the size of anatomical heterogeneities in the heart. Figure 7.6 shows ΔV_m around a cactus needle (≈0.28-mm diameter) when the FD is parallel to the electric field. Small regions of VEP occur in the area immediately around the cactus needle. The spatial scale and magnitude of ΔV_m are smaller with the cactus needle in comparison to the larger, 1.5-mm diameter micropipette. This is in agreement with numerical predictions [2]. When the electric field is applied from left to right, both moderate negative polarization and positive polarization of very small magnitude are visible in the temporal traces. With the reversed polarity, the pattern of VEP also reverses and negative polarization is observed in the temporal trace. However, positive polarization does not occur in the other trace. Rather, this region of tissue seems relatively unaffected by the shock. The small size of the heterogeneity may not be sufficient to produce positive polarization in systolic tissue when the majority of the left ventricle is hyperpolarized from the shock. However, even if positive polarization does

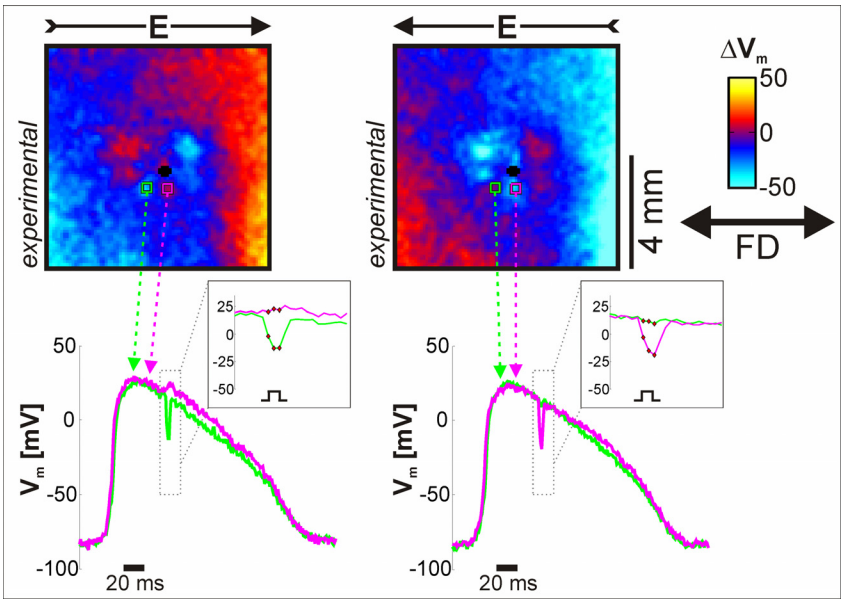

Figure 7.6. Virtual electrode polarization around a cactus needle during systolic field stimulation with fiber direction parallel to the electric field. Field shocks of 30 V/cm strength were applied for 3 ms to systolic tissue (S1-S2 coupling interval of 85 ms). Images of the shock-induced change in transmembrane potential (ΔV_m) are shown for both shock polarities. Temporal traces for the areas indicated by the magenta and green squares are depicted below the images. Insets of the traces reveal the shock response in more detail. Red diamonds indicate the interval of S2 application.

not occur with this electric field polarity, there still exists a gradient of V_m between the adjacent areas to allow charge diffusion and potentially generate a wave front.

7.5. Conclusions

These results are experimental confirmation of previous bidomain calculations.[1,2] The data reveal the importance of the relationship between the electric field, heterogeneity, and FD. Our findings suggest that insulated heterogeneities, such as plunge electrodes, could cause unintended experimental artifacts and results. The cactus needle data imply that VEP around even relatively small heterogeneities may play a role in far-field stimulation and arrhythmogenesis.

7.6. Acknowledgements

This work was supported by the National Institutes of Health (R01-HL58241-05; R01-HL57207), the American Heart Association (0215128B), and the Academic Venture Capital Fund of Vanderbilt University. We thank Thomas Howe for fabricating the goniometer, and David Mashburn for his work on the high voltage stimulator.

7.7. References

[1] Langrill Beaudoin, D. and Roth, B. J., "Effect of plunge electrodes in active cardiac tissue with curving fibers." *Heart Rhythm*, vol. 1, no. 4, pp. 476-481, 2004.

[2] Langrill, D. M. and Roth, B. J., "The effect of plunge electrodes during electrical stimulation of cardiac tissue." *IEEE Trans Biomed Eng*, vol. 48, no. 10, pp. 1207-1211, 2001.

[3] Frazier, D. W., Wolf, P. D., Wharton, J. M., Tang, A. S., Smith, W. M., and Ideker, R. E., "Stimulus-induced critical point. Mechanism for electrical initiation of reentry in normal canine myocardium." *J Clin Invest*, vol. 83, no. 3, pp. 1039-1052, 1989.

[4] Frazier, D. W., Krassowska, W., Chen, P.-S., Wolf, P. D., Danieley, N. D., Smith, W. M., and Ideker, R. E., "Transmural activations and stimulus potentials in three-dimensional anisotropic canine myocardium." *Circ Res*, vol. 63, no. 1, pp. 135-146, 1988.

[5] Sidorov, V. Y., Woods, M. C., and Wikswo, J. P., "Effects of elevated extracellular potassium on the stimulation mechanism of diastolic cardiac tissue." *Biophys J*, vol. 84, no. 5, pp. 3470-3479, 2003.

[6] Zhou, X., Smith, W. M., Rollins, D. L., and Ideker, R. E., "Transmembrane potential changes caused by shocks in guinea pig papillary muscle." *Am J Physiol Heart Circ Physiol*, vol. 271, no. 6 Pt 2, pp. H2536-H2546, 1996.

[7] Fast, V. G., Rohr, S., and Ideker, R. E., "Nonlinear changes of transmembrane potential caused by defibrillation shocks in strands of cultured myocytes." *Am J Physiol Heart Circ Physiol*, vol. 278, no. 3, pp. H688-H697, 2000.

[8] Cheng, D. K., Tung, L., and Sobie, E. A., "Nonuniform responses of transmembrane potential during electric field stimulation of single cardiac cells." *Am J Physiol Heart Circ Physiol*, vol. 277, no. 1, pp. H351-H362, 1999.

[9] Cheek, E. R., Ideker, R. E., and Fast, V. G., "Nonlinear changes of transmembrane potential during defibrillation shocks: Role of Ca^{2+} current." *Circ Res*, vol. 87, no. 6, pp. 453-459, 2000.

CHAPTER VIII

SUMMARY AND FUTURE WORK

The objectives of this research were to investigate experimentally the response of the heart in the context of the bidomain theory of cardiac tissue. Different experimental conditions and stimulation protocols were examined.

The review of cardiac dynamics in Chapter 2 illustrated the importance of studying electrical stimulation of the cardiac tissue. Ventricular fibrillation and the unknown mechanisms of defibrillation were discussed. The bidomain model was introduced as a numerical model which has accurately predicted many electrical properties of cardiac tissue and many of the effects of electrical stimulation of the heart. Experimental unipolar stimulation, producing the characteristic "dog bone" virtual electrode polarization pattern, was shown to agree with the unequal-anisotropy ratio bidomain model. Field stimulation and the proposed role of heterogeneities and virtual electrode polarization in bidomain theory were additionally described. Lastly, cardiac optical mapping was presented as a non-invasive way to measure the membrane response to electrical stimulation.

Chapter 3 details the results of anodal stimulation of diastolic cardiac tissue during elevated extracellular potassium conditions. Under normal conditions, activation from diastolic anodal stimulation is mediated by the make excitation mechanism. The excitation originates at the onset of the stimulus in the virtual cathodes that flank the virtual anode "dog bone". However, when the extracellular potassium concentration is

increased, as occurs during ischemia, the resting transmembrane potential is elevated. Elevation of resting transmembrane potential increases sodium channel inactivation, causing the threshold to increase and slowing action potential upstrokes. For threshold anodal stimulation in high potassium, we found that the virtual cathodes were not depolarized above threshold during the 10-ms stimulus because of the slowed upstroke. Because the resting transmembrane potential is elevated, hyperpolarization in the small virtual anode opens voltage-dependent sodium channel inactivation gates, producing increased excitability in the virtual anode. At the termination of the stimulus, charge that accumulated in the virtual cathodes (but could not overcome threshold) is sufficient to stimulate the virtual anode. Excitation, therefore, initiates in the virtual anode region at the termination of the stimulus, indicating anodal-break stimulation. Subsequent numerical predictions of the bidomain model qualitatively agreed with our experimental findings [1]. These results suggest that anode break, not anode make, may be the excitation mechanism for threshold unipolar anodal stimulation during hyperkalemia and ischemia.

In Chapter 4 we presented the results of unipolar cathodal stimulation in the wake of a planar conditioning wave propagating along the fiber direction. When the unipolar stimulus was applied near the refractory tail of the planar wave, slow-wave dynamics were observed. Two damped waves of small amplitude propagate slowly in opposite directions from the “dog bone” shaped polarization centered around the unipolar electrode. The damped wave that propagates into more refractory tissue (toward the planar conditioning wave) decays and dies approximately 28 ms after stimulus termination. The other damped wave, whose initial dynamics are similar to the first,

eventually evolves a full amplitude steadily propagating wave roughly 40 ms after stimulus termination. The transition of damped waves to full amplitude propagating waves suggests that slow propagation in electrically altered post-shock tissue may be one mechanism of re-excitation after unsuccessful defibrillation.

The role of virtual electrode polarization from unipolar stimulation in excitability through the cardiac cycle was presented in Chapter 5. The experimental strength-interval curves are in good agreement with the numerical predictions of the bidomain model. The transition of the stimulation mechanism from break to make always coincided with the final descending phase of both anodal and cathodal curves. This transition is attributed to the bidomain properties (virtual electrode polarization patterns) of cardiac tissue. Stimulation patterns near refractoriness show always an excitation mechanism mediated by damped wave propagation after S2 termination, similar to that described in Chapter 4.

In Chapter 6 field stimulation (2-ms duration) of the diastolic rabbit heart as a function of shock strength was presented. At low field strengths, activation was slow and appeared to propagate to the epicardium from sites of transmural initial activation. Hyperpolarization was not observed for weak shocks. Increasing the shock strength generally decreased activation time. Small-magnitude hyperpolarization and depolarization of the left ventricle and right ventricle depolarization occur with onset of moderate shocks. For shocks above 15 V/cm, virtual electrode polarization was strong and prominent except for right ventricle hyperpolarization, which was of small magnitude and localized to the right ventricular edge and apex. Left ventricular areas of negative virtual electrode polarization exhibited delayed activation.

We also presented the effects of shock duration (50-V/cm strength) in Chapter 6. Short shocks resulted in slow activation. However, in contrast to weak shocks, both positive and negative virtual electrode polarization of the left ventricle and right ventricle were observed. Activation time decreased with increasing shock strength until 2-ms. For 2-ms shocks, activation of the heart was very rapid, with the whole heart activated within 4 ms of shock onset. This is much faster than would be expected from propagation. For shocks longer than 2-ms, we observed paradoxical increase in activation time with increasing shock duration. Analyses of regions of interest corresponding to the right and left ventricles revealed delayed activation of the chamber facing the anode due to negative virtual electrode polarization. Activation delay caused by hyperpolarization of the left ventricle was more prominent than that of right ventricle hyperpolarization. The results of this study elucidate the effects of diastolic field stimulation of the isolated heart. Temporal activation analyses indicate that increasing shock strength and duration do not necessarily result in faster activation, and that negative virtual electrode polarization must be considered when applying field stimulation during diastole.

Chapter 7 detailed the virtual electrode effects around an artificial heterogeneity during field stimulation. Experimental data show alternating regions of positive and negative virtual electrode polarization around an insulated heterogeneity during field stimulation of both systolic and diastolic tissue. When the field polarity was reversed, the spatial pattern of polarization also reversed. The virtual electrode effects were more prominent when the fiber direction was parallel to the field, and minimized when the fibers were perpendicular to the field. A 90° rotation of the fiber direction reversed the spatial pattern of polarization. The experimental results are in good agreement with

bidomain predictions. The adjacent areas of positive and negative virtual electrode polarization around the heterogeneity are potential sites of wave front generation, and may be a mechanism for far-field stimulation. These results also suggest that heterogeneities introduced during experimental measurements, such as plunge electrodes, may cause unintended artifacts and results.

8.1. Overall Conclusions

A common theme of the results described in the above chapters is virtual electrode polarization in response to electrical stimulation of cardiac tissue. The bidomain model of cardiac tissue predicts virtual electrode polarization when unequal anisotropies of the intracellular and extracellular spaces are incorporated. Bidomain theory has revolutionized the field of cardiac stimulation, successfully characterizing many of the experimentally observed effects of electrical stimulation. The results of this research generally agree with predictions of the unequal-anisotropy ratio bidomain model, further validating the bidomain theory of cardiac tissue. An increased understanding of how cardiac tissue responds to electrical stimulation in various conditions will guide improvements in treatment and prevention of cardiac rhythm disorders.

8.2. Future Work

In some cases there are natural extensions of the individual research projects that lead to possible future experimental investigations.

Examining the effects of elevated extracellular potassium during field stimulation of the whole heart is a clinically relevant experiment. The extracellular potassium concentration of a fibrillating heart requiring defibrillation therapy may be elevated. Electroporation of the cardiac membrane occurs during high strength electrical shocks.

As the response of the diastolic heart to field stimulation has now been characterized, the spatial location and role of electroporation may be investigated. Researchers have begun to use fluorescent probes to detect electroporated regions in intact tissue [2,3]; however, this methodology has not been extended to field stimulation at the spatial scale of the whole heart. This research group has extensive preliminary data examining the spatial extent of electroporation during unipolar stimulation [4,5]. After the experimental technique is perfected, the protocol could be extended to examining electroporation during field stimulation of the whole heart.

One limitation of cardiac optical mapping is that only the activation is only viewed from the epicardial surface. Bidomain theory predicts endocardial polarization of the opposite polarity than epicardial polarization during field stimulation of the whole heart [6,7]. Earlier experiments from this group attempted to view endocardial activity transmurally by placing a fiber inside the left ventricle for endocardial illumination. Results did not agree with bidomain predictions: rapid activation of the endocardium was observed at shock onset, with no corresponding negative virtual electrode polarization [8]. However, our imaging resolution and stimulation control have greatly improved since that time. Revisiting these experiments with the improved technology may be warranted.

Finally, virtual electrode effects around an artificial heterogeneity were observed during field stimulation. This research may be extended by examining the effects of shock strength, duration, and timing and heterogeneity size. Imaging on a larger scale would reveal if wave front generation occurs at these heterogeneities. We observed virtual electrode polarization around a heterogeneity as small as a cactus needle. This size is on the order of small-scale anatomic heterogeneities inherent in the myocardium. Our

research group has developed a flat-field imaging system with very high spatial resolution that is ideal for studying the virtual electrode phenomenon on such a small scale.

8.3. Research Considerations

Before embarking on these research projects, the protection of research subjects and the societal impact of this research were considered.

8.3.1. Protection of Research Subjects

No human subjects were used in this research. Because the research project was directed towards developing an understanding of cardiac electrophysiology and its representation with the bidomain model, animal experimentation is necessary. The results from this research should lead to more accurate numerical simulations of the response of the heart to electrical stimulation and, therefore, reduce the use of experimental animals in the future.

Our group is very concerned about the proper and ethical use of animals in scientific research, and we go to great lengths to ensure that rabbits used in our work undergo a minimum of distress and discomfort. All lab personnel completed the Animal Research Training Program sponsored by the Institutional Animal Care and Use Committee, as required by Vanderbilt University. All experiments were conducted in accordance with National Institutes of Health regulations for the ethical use of animals in research and were pre-approved by the Vanderbilt Institutional Animal Care and Use Committee. New Zealand white rabbits were first preanesthetized with intramuscular ketamine followed by intravenous sodium pentobarbital for anesthesia. The hearts were then quickly excised and mounted on a Langendorff apparatus. After removal of the

heart, the rabbit carcass was returned to the Vanderbilt Division of Animal Care (DAC) for proper disposal. These methods are consistent with the recommendations of the Panel on Euthanasia of the American Veterinary Medical Association.

The personnel who staff the DAC performed the everyday care and maintenance of the experimental animals. Routine care of animals was provided by a group of animal technicians whose work is guided by supervisors and the DAC assistant to the director. Thus, except during the actual experimental procedures, the rabbits were housed and cared for by the DAC. The Vanderbilt University laboratory animal program is fully accredited by the AAALAC, and all research protocols involving vertebrate animals are reviewed by the Vanderbilt University veterinarian as required by Vanderbilt University policy.

8.3.2. Societal Implications

Coronary heart disease remains the single largest cause of mortality in the United States. An estimated 335,000 Americans die each year from sudden cardiac death, and the majority of these cases are believed to be from ventricular fibrillation [9]. An increased understanding of how the heart responds to electrical stimulation in different conditions is crucial to the development of better pharmacological and device therapies. The result will be an overall improvement in quality of life and increase in life expectancy.

8.4. References

[1] Roth, B. J. and Patel, S. G., "Effects of elevated extracellular potassium ion concentration on anodal excitation of cardiac tissue." *J Cardiovasc Electrophysiol*, vol. 14, no. 12, pp. 1351-1355, 2003.

[2] Sambelashvili, A. T., Nikolski, V. P., and Efimov, I. R., "Virtual electrode theory explains pacing threshold increase caused by cardiac tissue damage." *Am J Physiol Heart Circ Physiol*, vol. 286, no. 6, pp. H2183-H2194, 2004.

[3] Nikolski, V. P., Sambelashvili, A. T., Krinsky, V. I., and Efimov, I. R., "Effects of electroporation on optically recorded transmembrane potential responses to high-intensity electrical shocks." *Am J Physiol Heart Circ Physiol*, vol. 286, no. 1, pp. H412-H418, 2004.

[4] O'Grady, M. L., Woods, M. C., Wikswo, J. P., and Gilligan, J. M., "Electroporation of cardiac tissue from unipolar stimulation." *PACE*, vol. 26, no. 4 Part II, pp. 1023, 2003.

[5] Woods, M. C., O'Grady, M. L., Wikswo, J. P., and Gilligan, J. M., "The spatial extent of electroporation from point stimulation of cardiac tissue." *Proceedings of the 2003 Annual Fall Meeting of the Biomedical Engineering Society*, pp. 107, 2003.

[6] Entcheva, E., Trayanova, N. A., and Claydon, F. J., "Patterns of and mechanisms for shock-induced polarization in the heart: A bidomain analysis." *IEEE Trans Biomed Eng*, vol. 46, no. 3, pp. 260-270, 1999.

[7] Efimov, I. R., Aguel, F., Cheng, Y., Wollenzier, B., and Trayanova, N., "Virtual electrode polarization in the far field: implications for external defibrillation." *Am J Physiol Heart Circ Physiol*, vol. 279, no. 3, pp. H1055-H1070, 2000.

[8] Wikswo, J. P., Jr. and Lin, S.-F., "The drug-independent roles of cardiac geometry and tissue anisotropy in defibrillation and reentry." *Cardiostim 98, 11th International Congress*, vol. 53, no. 3, pp. 112, 1998. Nice, France.

[9] American Heart Association, "Heart disease and stroke statistics - 2005 update." Dallas, TX. American Heart Association, 2005.